

**Stochastic Model of Breakdown Nucleation Under  
Intense Electric Fields**

Thesis submitted for the degree of  
**“Doctor of Philosophy”**

**By**

**Eliyahu Zvi Engelberg**

Submitted to the Senate of the Hebrew University of Jerusalem  
September 2020



This work was carried out under the supervision of:

Prof. Yinon Ashkenazy



# Acknowledgments

I wish to thank my supervisor, Yinon Ashkenazy, for giving me the opportunity to pursue my PhD, and for his guidance and support.

I wish to thank Idit Mor Kline, assistant to chairperson of physics studies in the Hebrew University. Signing up for PhD studies was a financially challenging step, which was made possible for me by her efficiency and support at the initial stages and throughout.



# Abstract

Breakdown of metals subject to intense electric fields is a long-standing problem in high-voltage applications, limiting the obtainable amplitudes of electric and electromagnetic fields. One specific application is in the prospect study for the compact linear collider (CLIC) in CERN and other high-gradient accelerators, where understanding and controlling breakdown are pivotal topics. Surface features have been postulated to be essential in the development of breakdown. However, the mechanism by which such surface features come into being is not well understood.

In this thesis, we construct a *mobile dislocation density fluctuation* (MDDF) model, in which breakdown in a metal, subject to a strong electric field, is driven by dislocations in the crystal structure. In this model, the mobile dislocation density normally fluctuates around a stable point, with a finite probability to undergo a critical transition due to the effects of the external field. Once such a transition occurs, the mobile dislocation density will increase deterministically, leading to the formation of surface features and, subsequently, to breakdown. The probability of this transition is expected to increase with applied field, up to a critical field at which breakdown is immediate. By describing a mechanism by which surface features are created, which is consistent with experimental observations, the MDDF model completes the physical description of breakdown nucleation.

Model parametrization is achieved via microscopic analysis of oxygen-free high thermal conductivity (OFHC) Cu cathode samples from the CERN CLIC project, allowing the creation and depletion rates of mobile dislocations to be estimated as a function of the initial physical condition of the material and the applied electric field. We find analytical expressions for the mean

breakdown time and quasistationary probability distribution of the mobile dislocation density, and verify these results by using a Gillespie algorithm. A least-squares algorithm is used to fit the results with available experimental data of the dependence of the breakdown rate on the applied strength of the electric field and on temperature. The fitted predictions of the model are in good agreement with the experimental data.

The effects of the variation of some of the assumptions of the physical model are considered, and a number of additional experiments to validate the model are proposed, which include examining the effects of the temperature and pulse length, as well as of a time-dependent electric field, on the breakdown rate. In addition, based on the MDDF model, we predicted the existence of prebreakdown fluctuations of the mobile dislocation density, which are manifested as spikes in the dark current measured between electrodes. A setup was built in CERN to test this prediction, in which these spikes were, indeed, discovered and characterized. Their rate of occurrence and distribution in time agree with the predictions of the MDDF model, both in functional form and in absolute numerical values. The prediction and description of this new phenomenon serves to further validate the model, and provides an option of early detection of imminent breakdown.

# Statement of Contribution

This thesis includes three chapters presented as research articles. I was the primary contributor, and my supervisor is listed as a coauthor, in all three articles.

Michael Assaf is listed as a coauthor of Chapter 2. Dr. Assaf supervised my work on the analytical solution of the stochastic model.

Ayelet Badichi Yashar, Michael Assaf, and Inna Popov are listed as coauthors of Chapter 3. Dr. Popov and Ms. Badichi Yashar conducted the microscopic observations which are used in the chapter. Dr. Assaf supervised the analytical work on the WKB approximation and on the field ramping.

Jan Paszkiewicz, Ruth Peacock, Sagy Lachman, and Walter Wuensch are listed as coauthors of Chapter 4. Mr. Paszkiewicz and Ms. Peacock conducted the experiment described in this chapter at CERN, under the supervision of Dr. Wuensch. Mr. Lachman created and coded the spike identification algorithm, and contributed to the code which performed the maximum likelihood calculations.



# Contents

<b>Abstract</b>	<b>v</b>
<b>Statement of Contribution</b>	<b>vii</b>
<b>1 Introduction</b>	<b>3</b>
1.1 Vacuum Arcs . . . . .	3
1.2 The CLIC Study . . . . .	4
1.3 Dislocations . . . . .	6
1.4 Plastic Deformation and Breakdown . . . . .	10
1.5 Birth-Death Markov Processes . . . . .	12
1.6 Simulation of Birth-Death Markov Processes . . . . .	18
1.7 Frank-Read Sources . . . . .	20
1.8 Dark Current . . . . .	22
1.9 Overview of the Following Chapters . . . . .	24
<b>2 Stochastic Model of Breakdown Nucleation Under Intense Electric Fields</b>	<b>27</b>
<b>3 Theory of Electric Field Breakdown Nucleation Due to Mobile Dislocations</b>	<b>37</b>
<b>4 Dark Current Spikes as an Indicator of Mobile Dislocation Dynamics Under Intense DC Electric Fields</b>	<b>55</b>
<b>5 Discussion</b>	<b>65</b>
5.1 Comparison to Goals in the Research Proposal . . . . .	65
5.2 Applicability and Future Research . . . . .	66



# CHAPTER 1

## Introduction

---

### 1.1 Vacuum Arcs

A *cathodic arc*, or electric arc, is a discharge of electricity between electrodes in a gas or vapor. Lightning is a natural example of the cathodic arc [1]. Human-made cathodic arcs were observed in experiments beginning in the eighteenth century, in which both the arcs themselves and *cathode spots*, i.e., markings left by the arcs on the surface of the electrodes, were studied. At this point, too, it was recognized that cathodic arcing can be used for *coating*, which is the deposition of a thin layer of one material on another. Improved vacuum technology led, in the middle of the nineteenth century, to the experimental observation of *vacuum arcs*, in which the medium effecting the electrical discharge is plasma originating from the electrodes themselves, rather than a preexisting gas between the electrodes [2].

Beginning at the end of the nineteenth century, the use of cathode arcing was considered for the purpose of lighting [2]. After the Second World War, the industrial use of vacuum arcing in circuit breakers, and for coating, gradually became widespread. The ongoing development of these applications continues to be of importance in modern industry [1, 2].

Conversely, in applications which require the maintenance of high voltages between electrodes, vacuum arcing is a long-standing problem, limiting the obtainable amplitudes of electric and electromagnetic fields. In these

applications, vacuum arcing is also known as *vacuum breakdown*, or, simply, *breakdown*. The problem of breakdown has assumed importance due to the initiation of next-generation linear collider projects, which employ strong radio frequency (rf) electromagnetic fields. These projects include the Next Linear Collider collaboration at SLAC in the United States, the Global Linear Collider collaboration at KEK in Japan, and the Compact Linear Collider (CLIC) study at CERN in Switzerland, in each of which breakdown has become a limiting factor. A better understanding of breakdown is important for each of these groups, in order to achieve higher electric field gradients at the reliability that they need [3]. Such an understanding would be valuable for other fields in which breakdown is relevant, too, as either a desired effect or one to be prevented.

## 1.2 The CLIC Study

The research described in this thesis was done in collaboration with the CLIC study mentioned above [4]. Therefore, a brief description of the CLIC study follows.

CLIC is an international collaboration working on a next-generation linear particle accelerator (linac) concept, to collide electrons and positrons at energies of up to 3 TeV. At the initial stage, in which the length of the linac will be 11.4 km (see Fig. 1.1), the collision energy will reach 380 GeV. The linac will be made up of a series of oxygen-free high conductivity (OFHC) Cu *accelerating structures*, each of which is approximately 25 cm long, see Fig. 1.2. As the main beam of particles to be collided passes through each accelerating structure, a pulsed radio frequency (rf) electric field of up to 100 MV/m is applied within the structure, thus accelerating the beam. This

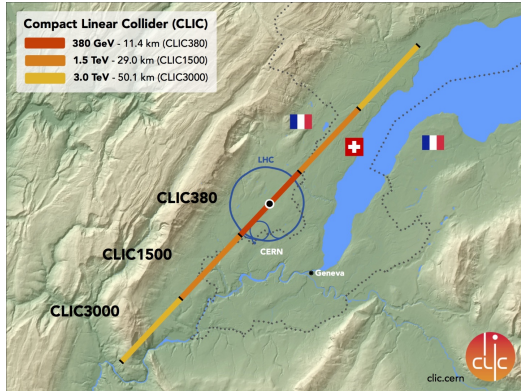


**Figure 1.1:** Map of the proposed stages of CLIC, to be built underground.

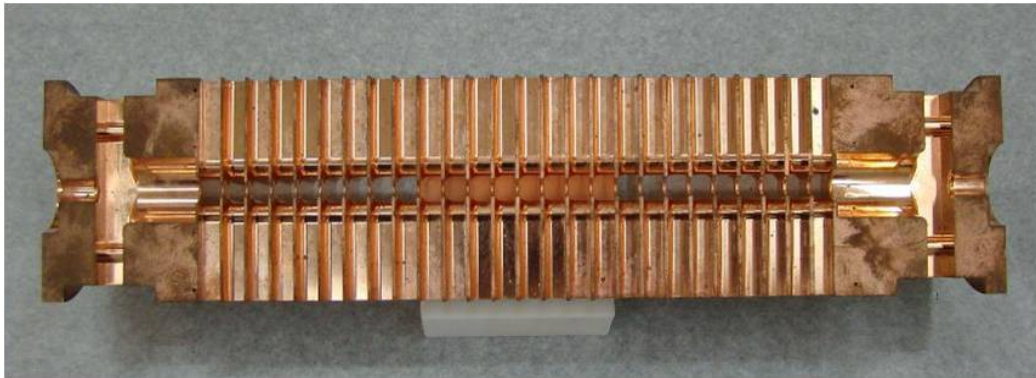


**Figure 1.2:** A CLIC accelerating structure.

electric field is also called an *acceleration gradient*. The length of each pulse is about 200 ns, and the pulses are applied at a repetition rate of 50 Hz.

As described previously, the CLIC study has encountered vacuum breakdown, between the electrodes of the accelerating structures, as the main factor limiting the obtainable accelerating gradients. If breakdown occurs during operation of the accelerator, the accelerated particle beams will not collide [5]. therefore, the goal at CLIC is to reduce the breakdown rates to  $3 \times 10^{-7}$  breakdowns per pulse per meter (bpp/m) of accelerator length [6].

To investigate breakdowns in an environment which is simpler, and more specifically targeted to their study, direct current (dc) setups were con-



**Figure 1.3:** An electrode of the LES.

structed in CERN and elsewhere. One of these is the Large Electrodes System (LES) in CERN, see Fig. 1 in Chapter 4 and Fig. 1.3 here. While some characteristics of the rf and dc setups obviously differ, many insights gained from dc measurements were shown to be valid in rf systems, too [5, 7, 8].

### 1.3 Dislocations

The steps leading to vacuum breakdown are understood to consist of surface modification by the electromagnetic fields, leading to electron emission and evaporation of the electrode material in the vacuum, and, subsequently, to arcing, as described in detail in Chapter 3. The process leading to the initial surface modification, however, is not well understood. When various electrode materials were experimented with, a correlation was found between measured breakdown rates and the crystal structure of the tested materials, i.e., if the material was a face-centered cubic (fcc), body-centered cubic (bcc), or hexagonal close-packed (hcp) structure material. In addition, breakdown rates varied among differently machined electrodes, even when they were made of the same material. This suggested that the mobility of dislocations

is somehow involved in breakdown nucleation [9]. Since this idea, albeit in a modified form, is developed in this thesis, a brief description of crystal structures and dislocations follows.

Atoms in a crystal are organized in periodic structures, defined by translation vectors  $\vec{a}_1$ ,  $\vec{a}_2$ , and  $\vec{a}_3$ , which are not necessarily orthogonal. The crystal looks the same when viewed from the point  $\vec{r}$  or from the point  $\vec{r}' = \vec{r} + u_1\vec{a}_1 + u_2\vec{a}_2 + u_3\vec{a}_3$ , for any integer  $u_1$ ,  $u_2$ , and  $u_3$ . The set of points  $\vec{r}'$  is called a *lattice*. A basis, consisting of one or more atoms, is attached to each point of the lattice [10].

The atoms of metals are commonly arranged as body-centered cubic (bcc), face-centered cubic (fcc), or hexagonal close packed (hcp) lattices. As its name suggests, the translation vectors of the bcc lattice are of equal length and orthogonal.  $a = |\vec{a}_1| = |\vec{a}_2| = |\vec{a}_3|$  is called the *lattice constant*. The basis, contained in each cell of the bcc lattice, consists of two atoms, at points  $(0, 0, 0)$  and  $(\frac{a}{2}, \frac{a}{2}, \frac{a}{2})$  of each cell, see Fig. 1.4(a). The translation vectors of the fcc lattice are identical to those of the bcc lattice. Its basis, however, is made up of four atoms, at the positions  $(0, 0, 0)$ ,  $(\frac{a}{2}, \frac{a}{2}, 0)$ ,  $(0, \frac{a}{2}, \frac{a}{2})$ , and  $(\frac{a}{2}, 0, \frac{a}{2})$ , as shown in Fig. 1.4(b) [10].

In the hcp lattice,  $|\vec{a}_1| = |\vec{a}_2|$ , and there is an angle of  $120^\circ$  between them.  $\vec{a}_3$  is perpendicular to both other vectors, and its length is around  $\sqrt{8/3}$  times theirs, see Fig. 1.4(c) [10].

A few types of defects can be found in the crystal structure of metals. *Dislocations* are one such type, in which one part of a crystal is displaced, or *slips*, relative to another part. The dislocation is the boundary between slipped and unslipped regions in the crystal. If the dislocation line is perpendicular to the direction of the slip, the dislocation is an edge dislocation, see Fig. 1.5(a). If it is parallel to it, it is a screw dislocation, see Fig. 1.5(b) [10].

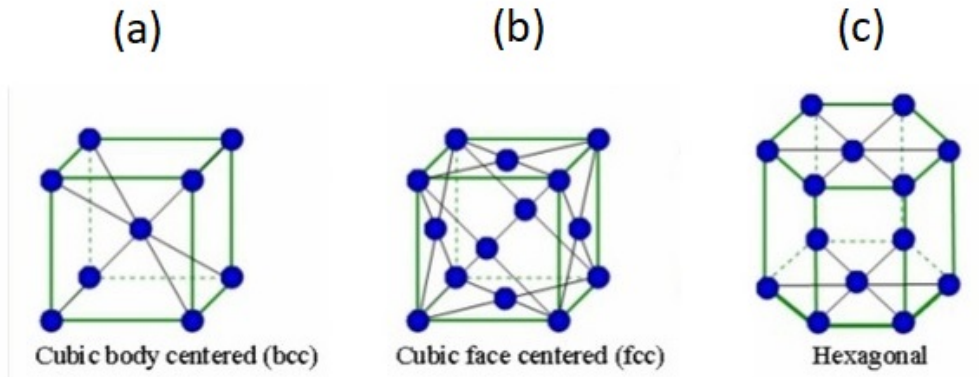


**Figure 1.4:** (a) bcc, (b) fcc, and (c) hcp lattices.

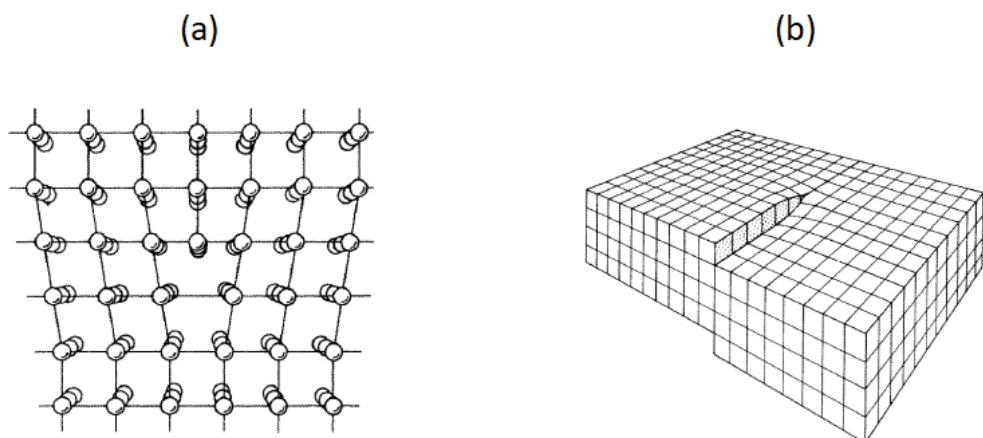


**Figure 1.5:** (a) Edge and (b) screw dislocations.

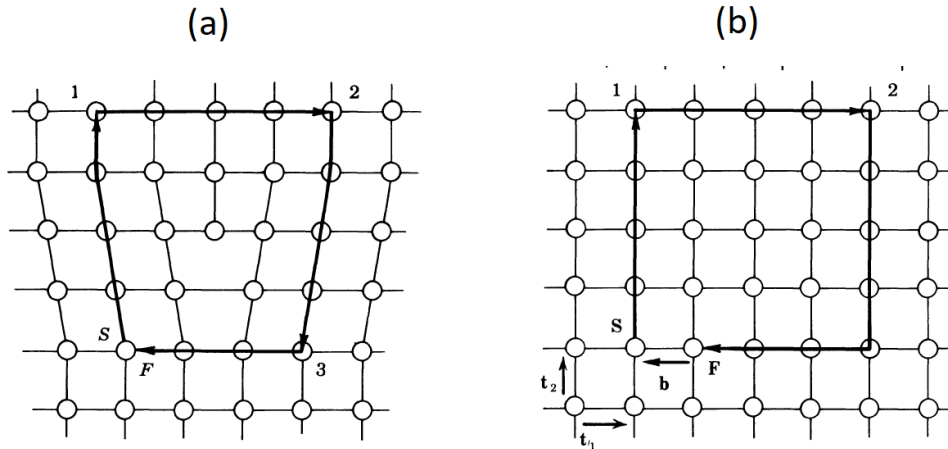


**Figure 1.6:** The Burgers circuit in (a) the crystal with the dislocation and (b) a perfect crystal. The Burgers vector closes the circuit in (b).

The direction of slip can be characterized by the *Burgers vector*  $\vec{b}$ . To find the Burgers vector, one draws a closed clockwise circuit around the dislocation line in the crystal, as in Fig. 1.6(a). Then one draws a clockwise circuit with the same links from atom to atom in a perfect crystal, as in Fig. 1.6(b). The vector required to close the circuit in the perfect crystal is the Burgers vector  $\vec{b}$ . If  $\hat{\xi}$  is the direction of the dislocation line, then  $\vec{b} \cdot \hat{\xi} = 0$  for an edge dislocation, and  $\vec{b} \cdot \hat{\xi} = \pm b$  for a screw dislocation (the plus or minus depending on an arbitrary choice of the sense of the dislocation line). In general, a dislocation can have a mixed character, with edge and screw components, and its Burgers vector can be resolved into a screw component  $\vec{b}_s = (\vec{b} \cdot \hat{\xi})\hat{\xi}$  and an edge component  $\vec{b}_e = \hat{\xi} \times (\vec{b} \times \hat{\xi})$  [11].

An external stress exerts a force on a dislocation which can cause it to move. The vector components of the force, per unit length of dislocation, are

$$F_k = -\epsilon_{ijk}\xi_i\sigma_{jl}b_l, \quad (1.1)$$

where  $\epsilon_{ijk}$  is the permutation operator, and  $\sigma$  is the external stress tensor. However, dislocations do not move freely through the crystal which contains them. Rather, they become *pinned*, or *sessile*, when they intersect with other dislocations. Pinned dislocations can lead to the creation of new dislocations, or can continue their motion, as a result of thermally activated processes. An example of the first type of process is the *Frank-Read mechanism* (further discussed in Sec. 1.7), and an example of the second type is *cross slip*. Either type leads to the creation of *mobile dislocations*, which can then be annihilated either when they are rendered sessile, or when they reach the surface of the metal and cause its deformation [11].

## 1.4 Plastic Deformation and Breakdown

Slip in crystals occurs in the direction of closest atomic packing. Hence, the Burgers vector of a dislocation is normally in the direction of the closest packing of atoms in a crystal. The dislocations themselves, and their motion, must also be along the planes of closest atomic packing, which are, therefore, called *slip planes* or *glide planes*. As a result, the crystal structure of a metal is significant in characterizing its dislocations, their motion, and their interactions. For example, in an fcc crystal such as Cu, dislocations will have Burgers vectors in the  $\langle 110 \rangle$  directions, and will be situated and glide along the  $\{111\}$  planes, see Fig. 1.7 [11]. (In fcc crystals *partial dislocations*, whose Burgers vectors are not in the  $\langle 110 \rangle$  directions, are energetically favored and therefore common. However, partial dislocations, too, are situated and move along the  $\{111\}$  planes, and, furthermore, the *sum* of two partial dislocations of different types is always in a  $\langle 110 \rangle$  direction.)

When a dislocation reaches the surface of a metal, it leads to its defor-

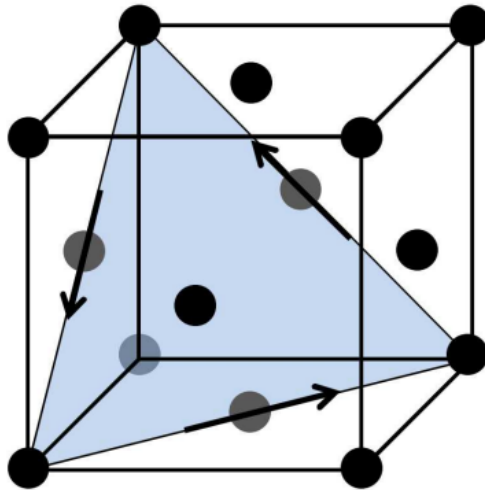


**Figure 1.7:** The fcc unit cell, showing the atoms of the cell, one of its slip planes (shaded region), and three of its slip directions (arrows).

mation, because one part of the surface is shifted by  $\vec{b}$  relative to the other, see Fig. 1.8. As explained in Sec. 1.3, stress creates mobile dislocations and can then pull them to the surface. Each such dislocation further deforms the surface of the metal. This deformation, which cannot be reversed, is called *plastic deformation*.

Because dislocations can lead to surface deformation, and because a correlation was observed between breakdown rates and the crystal structure of different materials, it was suggested that dislocation dynamics are involved in breakdown nucleation. In addition, the machining of electrodes, which is known to effect dislocation densities and their interaction, was observed to have an effect on breakdown rates. However, despite the apparent relation between dislocations and breakdown, computerized models did not manage to reproduce the formation of surface features on electrodes subjected to intense electric fields, unless they assumed the implausible existence of major defects inside the electrode material [9]. Microscopic observations of such

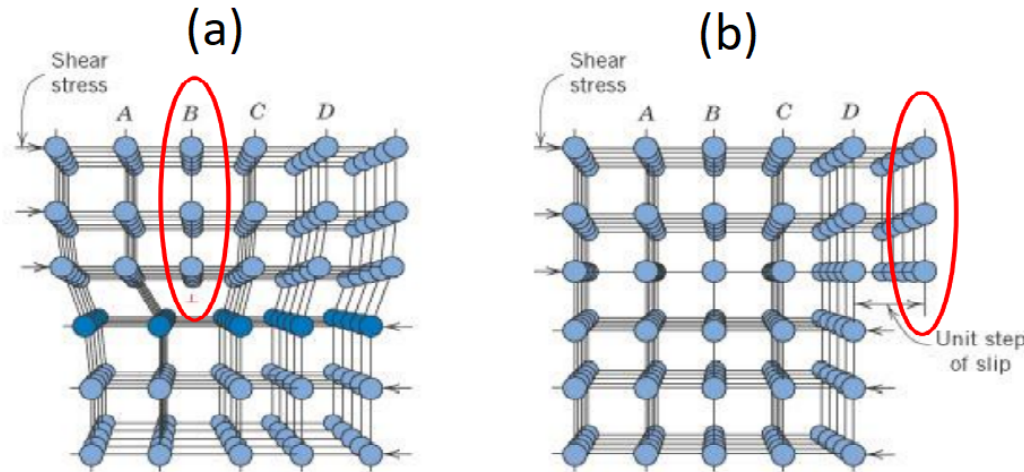


**Figure 1.8:** (a) A dislocation inside a crystal, pulled to the surface by stress, (b) causes plastic deformation.

electrodes, and the measurement of breakdown rates over long periods of time, also preclude both the preexistence of surface features, and the possibility that these features develop over time (see Chapters 2-4 for a detailed explanation.)

To overcome this difficulty, It was suggested that the stochastic nature of dislocation dynamics, described in Chapter 2, must be taken into account. This approach underlies the *mobile dislocation density fluctuation* (MDDF) model, which is developed in this dissertation. In this model, the creation and depletion of mobile dislocations are treated as a birth-death Markov process. Some mathematical and computational methods pertaining to such processes are, therefore, described in the following sections.

## 1.5 Birth-Death Markov Processes

The MDDF model describes the fluctuations of the mobile dislocation density in a slip plane as a series of discrete changes in the number of mobile

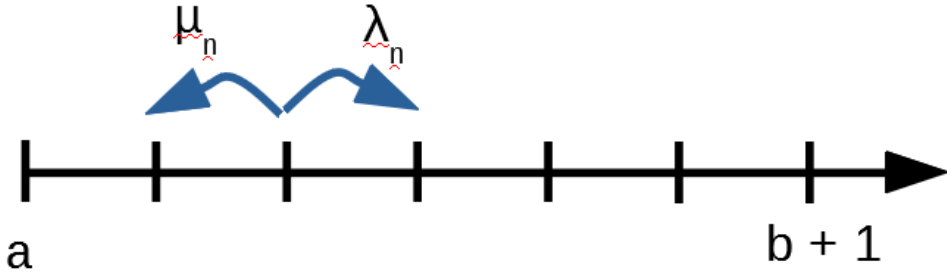


**Figure 1.9:** A one-step birth-death Markov system, with a reflecting boundary  $a$  and an absorbing boundary  $b + 1$ .

dislocations. The probability that a dislocation will be created or depleted is dependent only on the present number of mobile dislocations in the slip plane. Processes of this type are called *birth-death Markov processes*. The system undergoing the Markov process can be at any state  $n$ , with  $n$  represented by an integer number (which, in the MDDF model, is equal to the number of mobile dislocations). At any given time, the system has a certain probability  $P_n(t)$  of being at a state  $n$  [12].

In the MDDF model, only one dislocation can be created or depleted at a time, so from any state  $n$  transitions are allowed only to the states  $n - 1$  and  $n + 1$ . Such a system undergoes a *one-step birth-death Markov process*, see Fig. 1.9. It can be described using the *master equation*

$$\frac{dP_n(t)}{dt} = \lambda_{n-1}P_{n-1}(t) + \mu_{n+1}P_{n+1}(t) - (\lambda_n + \mu_n)P_n(t), \quad (1.2)$$

where  $\lambda_n$  is the rate of transition from state  $n$  to state  $n + 1$ , and  $\mu_n$  is the rate of transition from  $n$  to state  $n - 1$  [12].

We further consider such a system where  $n$  can have values only between  $a$  and  $b + 1$ . The system has a reflecting boundary at  $a$  and an absorbing

boundary at  $b + 1$ , meaning that the system can transition from  $a$  only to  $a + 1$ , and if the system reaches the state  $b + 1$ , it stays there. In other words,

$$\mu_a = \mu_{b+1} = \lambda_{b+1} = 0. \quad (1.3)$$

In such a system, we can ask what the *mean first passage time* is, i.e., how long it will take, on average, to transition from any state  $n$  to the absorbing state  $b + 1$ . The mean time  $T_n$  can be found recursively, by considering the fact that the system can transition out of  $n$  to either  $n - 1$  or  $n + 1$ . Therefore, the mean time from  $n$  to  $b + 1$  is equal to the mean time out of  $n$ , plus the mean time from  $n - 1$  to  $b + 1$  times the probability that the transition was to  $n - 1$ , plus the mean time from  $n + 1$  to  $b + 1$  times the probability that the transition was to  $n + 1$ , see Fig. 1.10. i.e.,

$$T_n = \frac{\lambda_n}{\lambda_n + \mu_n} T_{n+1} + \frac{\mu_n}{\lambda_n + \mu_n} T_{n-1} + \frac{1}{\lambda_n + \mu_n}. \quad (1.4)$$

The solution of this equation, together with the boundary conditions of Eq. (1.3), is

$$T_n = \sum_{y=n}^b \phi_y \sum_{z=a}^y (\lambda_z \phi_z)^{-1}, \quad (1.5)$$

with  $\phi_n = \prod_{z=a+1}^n \mu_z / \lambda_z$  [12]. In Chapters 2 and 3 the transition probabilities and boundaries of the Markov process in the case of the MDDF model are calculated, and are then used to find the mean first passage time as described.

Although Eq. (1.5) gives an exact solution for the mean first passage time, its usage can be cumbersome, because it involves two sums. To find an alternative expression, we consider the case in which there is no absorbing state  $b + 1$ , and the probability of being at any state  $n$  is time independent.

In such a case  $dP_n/dt = 0$ , so, by Eq. (1.2),

$$\lambda_{n-1} P_{n-1} + \mu_{n+1} P_{n+1} - (\lambda_n + \mu_n) P_n = 0. \quad (1.6)$$

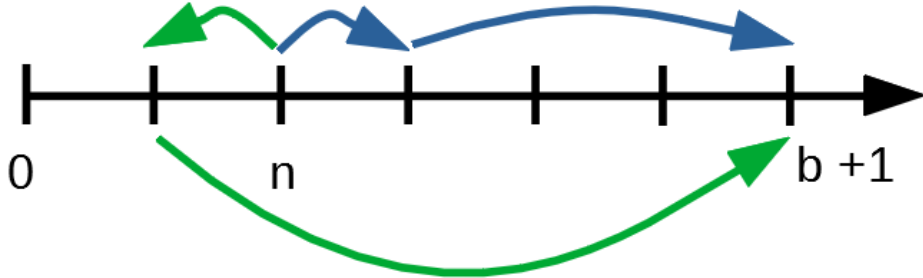


**Figure 1.10:** The possible paths from state  $n$  to the absorbing state  $b + 1$ .

Together with the boundary condition  $\mu_a = 0$  (because  $a$  is a reflecting boundary), this can be shown to lead to the *detailed balance* condition

$$P_n = \frac{\lambda_{n-1}}{\mu_n} P_{n-1}. \quad (1.7)$$

i.e., at any time, the probability of transitioning from  $n - 1$  to  $n$  (which consists of the probability of being at state  $n - 1$  multiplied by the rate of transition to  $n$  in such a case) is equal to the probability of transitioning in the reverse direction. This leads to the *stationary solution* [12]

$$P_n = P_a \prod_{z=a+1}^n \frac{\lambda_{z-1}}{\mu_z}. \quad (1.8)$$

The value of  $P_a$  itself can be found by normalizing the probability distribution, i.e.,  $\sum_n P_n = 1$ , or using case-specific approximations, as will be done in Chapters 2 and 3.

We now consider again the case in which there is an absorbing state  $b + 1$ . Clearly, in this case the probability distribution must also be time dependent, because  $P_{n \leq b}(t \rightarrow \infty) = 0$  and  $P_{b+1}(t \rightarrow \infty) = 1$ , which is not the case before the system reaches the absorbing state. However, if the system fluctuates around a *stable point*  $n_*$ , with a low probability of transitioning

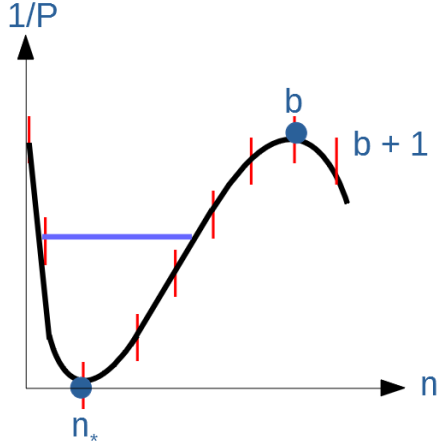


**Figure 1.11:** A metastable Markov system, which normally fluctuates around the stable point  $n_*$ , with a low probability of reaching the absorbing state  $b + 1$ . The y axis is the inverse of the probability of being found at  $n$ , so that transitions are more likely from higher to lower points on the graph.

to the absorbing state (see Fig. 1.11), it is possible to employ a *metastable approximation*. It is assumed that the probability distribution of the system is given by the *metastable ansatz*

$$P_{n \leq b}(t) = \pi_n e^{-t/\tau} \quad (1.9)$$

for states which are not the absorbing state, and

$$P_{b+1}(t) = 1 - e^{-t/\tau} \quad (1.10)$$

for the absorbing state.  $\pi_n$  itself is time independent, and is called the *quasistationary probability distribution* (QSD) [13].

Plugging Eq. (1.9) into the master equation (1.2) yields

$$-\frac{1}{\tau}\pi_n = \lambda_{n-1}\pi_{n-1} + \mu_{n+1}\pi_{n+1} - (\lambda_n + \mu_n)\pi_n. \quad (1.11)$$

If  $1/\tau$  is very small compared to the transition rates, this becomes

$$\lambda_{n-1}\pi_{n-1} + \mu_{n+1}\pi_{n+1} - (\lambda_n + \mu_n)\pi_n = 0, \quad (1.12)$$

which is identical to Eq. (1.6). The assumption concerning  $1/\tau$  is valid if the relaxation time of the system from any state to  $n_*$  is much smaller than  $\tau$ , and it can be verified *a posteriori*. Eq. (1.12) leads, just as Eq. (1.6) did, to

$$\pi_n = \pi_a \prod_{z=a+1}^n \frac{\lambda_{z-1}}{\mu_z}, \quad (1.13)$$

so the quasistationary probability distribution can be calculated for any  $n$  [13].

To find the value of  $\tau$ , we write the master equation (1.2) for the state  $b + 1$ , remembering that transitions out of the state are impossible:

$$\frac{dP_{b+1}(t)}{dt} = \lambda_b P_b(t). \quad (1.14)$$

Substituting Eqs. (1.9) and (1.10) into this, we have

$$\frac{1}{\tau} e^{-t/\tau} = \lambda_b \pi_b e^{-t/\tau}, \quad (1.15)$$

or

$$\tau = (\pi_b \lambda_b)^{-1}. \quad (1.16)$$

The system is at the absorbing state at time  $t$  if, and only if, it transitioned into it at a time  $t' < t$ . Eq. (1.10) is, therefore, the *cumulative probability function* (CDF) of the distribution of the first passage time. Its form is that of the CDF of the *exponential distribution* [14]. Hence, the mean first passage time is the mean of the exponential distribution, which is  $\tau$ . Eq. (1.16) provides, therefore, an approximate of calculating the mean first passage time (using the metastable approximation), which is simpler than Eq. (1.5).

## 1.6 Simulation of Birth-Death Markov Processes

Birth-death Markov processes can be simulated using a *kinetic Monte Carlo* (KMC) method, in which the time evolution of a stochastic physical process is examined by the use of randomness. In *rejection KMC*, one possible transition from a given state is chosen, and then a decision is made if to accept or reject the transition, based on the rate of that specific transition. In contrast, in *rejection-free KMC*, or the *Gillespie algorithm*, the total rate of transition is first calculated, and then the specific transition to be carried out is chosen. The latter algorithm is computationally more efficient when there is a small number of transitions to choose from, as is the case in one-step birth-death Markov processes, where at most two transitions out of each state are possible, see Fig. 1.9 [14].

The Gillespie algorithm can be summarized as follows [14]:

1. Get a uniformly distributed random number  $0 \leq r < 1$ .
2. Calculate the time interval  $\Delta t$  until stepping, see below.
3. Increment the system time  $t \rightarrow t + \Delta t$ .
4. Get a uniformly distributed random number  $0 \leq r' < 1$ .
5. If  $r' < \mu_n / (\mu_n + \lambda_n)$ , decrement  $n$  by one. Otherwise, increment  $n$  by one.
6. Return to the beginning of the algorithm, or exit.

To calculate the time interval  $\Delta t$  in step #2, we consider the total transition rate out of the state  $n$ , which is  $\lambda = \mu_n + \lambda_n$ . In a short enough time

$\delta t$ , we can neglect the probability that two transitions will occur, i.e., there either will be a transition with a probability of  $\lambda\delta t$ , or not, with a probability of  $1 - \lambda\delta t$ . We now assume that the transition out of  $n$  is a *Poisson process*, meaning that the transition rate does not depend on the time elapsed since the last transition. In such a case, the probability that there were no transitions within a time interval  $t + \delta t$  (where  $t$  is finite and  $\delta t$  infinitesimal) is equal to the product of the probability that there were no transitions in either of the individual intervals, i.e.,

$$P(0; t + \delta t) = P(0; t)(1 - \lambda\delta t). \quad (1.17)$$

Rearranging terms leads to the differential equation

$$\frac{P(0; t + \delta t) - P(0; t)}{\delta t} = -\lambda P(0; t) \Rightarrow P(0; t) = C e^{-\lambda t}. \quad (1.18)$$

We must have  $P(0; t = 0) = 1$ , and therefore  $C = 1$ , i.e. [14],

$$P(0; t) = e^{-\lambda t}. \quad (1.19)$$

If the time  $\Delta t$  elapsed from the previous transition to the present one is in the interval  $(t, t + \delta t)$ , this means that no transition occurred in time  $t$ , but one *did* occur in time  $t + \delta t$ . The probability of this happening is

$$P(t < \Delta t < t + \delta t) = P(0; t) - P(0; t + \delta t) = \frac{dP}{dt} \delta t. \quad (1.20)$$

The *cumulative distribution function* (CDF) of this probability distribution is, therefore,

$$P(\Delta t < t) = \int_0^{\Delta t} \frac{dP}{dt} dt = P(0; t = 0) - P(0; t = \Delta t) = 1 - e^{-\lambda \Delta t}. \quad (1.21)$$

This is the CDF of an exponential distribution, meaning that the distribution of times between events, in a Poisson process, follows the exponential distribution [14].

To obtain a random value of  $\Delta t$  which follows the exponential distribution, we apply the inverse of the CDF to the uniformly distributed value of  $r$ , i.e.,  $1 - \exp(-\lambda\Delta t) = r$ . Alternatively, since the distribution of  $1 - r$  is identical to that of  $r$ , we can omit the subtraction from 1, leading to the equation

$$e^{-\lambda\Delta t} = r \Rightarrow \Delta t = -\frac{\ln r}{\lambda}. \quad (1.22)$$

Recalling that  $\lambda = \mu_n + \lambda_n$ , the calculation in step #2 of the Gillespie algorithm is [14]

$$\Delta t = -\frac{\ln r}{\mu_n + \lambda_n}. \quad (1.23)$$

## 1.7 Frank-Read Sources

As stated in Sec. 1.3, there are a number of mechanisms by which mobile dislocations can be generated, either by the production of new dislocations which are initially mobile, or by freeing sessile dislocations to move. These mechanisms are *thermally activated*, i.e., an initial energy barrier must be overcome, on the atomic level, in order for the mechanisms to have effect. Work done by external stress can reduce this energy barrier. Therefore, the probability of overcoming the energy barrier, at every attempt by the system to do so, is  $\exp[-(E_a - \Omega\sigma)/(k_B T)]$ , where  $\sigma$  is the external stress applied, and  $T$  is the temperature.  $E_a$  and  $\Omega$  are the *activation energy* and *activation volume*, respectively. Each mechanism which produces mobile dislocations is expected to have its own typical activation energy and volume. In addition, each mechanism will have its own *attempt frequency*  $\nu$ , so that the rate at which mobile dislocations are produced by one source are  $\nu \exp[-(E_a - \Omega\sigma)/(k_B T)]$  [11].

At this stage of the development of the MDDF model, we do not attempt

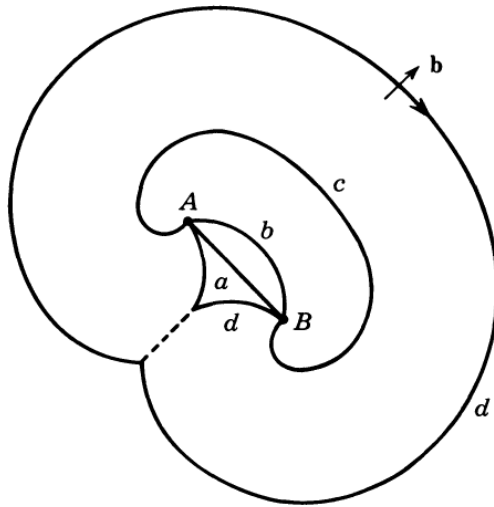


**Figure 1.12:** (a) A dislocation segment pinned at points A and B, under stress, (b) and (c) bows out in its slip plane, and (d) acts as a Frank-Read source, generating a new dislocation.

to determine the relative contributions of different mechanisms to the overall rate of production of mobile dislocations. Rather, as an example of the applicability of the model, we assume that mobile dislocations are produced by one of the common mechanisms, viz *Frank-Read sources* of minimal length, and use its characteristics to calculate  $E_a$ ,  $\Omega$ , and  $\nu$ . Therefore, a brief description of Frank-Read sources follows. Further research, using atomistic simulations, can determine if this mechanism or another one is the main source of nucleation of mobile dislocations.

A Frank-Read source is activated when two points of a dislocation, located on one slip plane, are pinned, see Fig. 1.12. An applied external stress can cause the dislocation line between the edges to bow out. When the dislocation line becomes a full circle, its opposing edges annihilate, the pinned dislocation is restored to its original form, and a new mobile dislocation is formed on the slip plane around it [15].

A curved dislocation experiences a surplus energy compared to a straight dislocation. Due to this energy, which is called its *line tension*, the curved dislocation is subject to a force which tends to straighten it. The magnitude of this force per unit length of dislocation is  $F = Gb^2/R$ , where  $G$  is the shear modulus of the metal in question (48 GPa in Cu), and  $R$  is the radius of curvature of the dislocation. When a Frank-Read source of length  $L$  (when straight) is curved to the shape of a circle, the radius of the circle must be equal to  $L/2$ . On the other hand, from Eq. (1.1), the maximum force per unit length which a stress in any direction can exert on a dislocation is  $\sigma b$ . To activate a Frank-Read source, the force of the external stress must be at least equal to the force due to the line tension, i.e. [15],

$$\sigma_{\text{th}}b = Gb^2/R \Rightarrow \sigma_{\text{th}} = 2Gb/L. \quad (1.24)$$

This expression is used, in Chapters 3 and 4, to estimate the attempt frequency  $\nu$  of the creation of dislocations by a Frank-Read source.

## 1.8 Dark Current

Although high-gradient applications depend on maintaining an open-circuit voltage between electrodes, a small current called the *dark current* nonetheless flows among them. This is due to the fact that electrons within the metal of the cathode tunnel to the surface, and are pulled by the electric field to the anode. The release of electrons from the metal by the field is called *field emission*. Since the dark current is examined in Chapter 4 as a prebreakdown signal, it is briefly discussed in this section.

If an electrode with a flat surface fills the volume  $z < 0$ , and an electric field  $E$  is applied, the effective potential energy  $V(z)$  is  $-W_a$  for  $z < 0$  (within the metal), and  $-eEz - e^2/4z$  for  $z > 0$  (outside the metal), see Fig. 1.13.

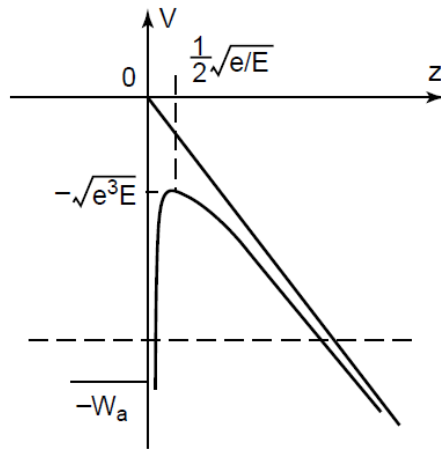


**Figure 1.13:** The potential barrier at the surface of a cathode. The metal fills the region where  $z < 0$ .

Here,  $-W_a$  is the potential energy of the electron inside the metal, and  $-e$  is the charge of the electron. The term  $-e^2/4z$  arises because, when the electron is close to the metal, it induces an image charge which pulls it back in the direction of the metal [16].

The field emission current depends on the flux of electrons arriving at the potential barrier, multiplied by the transmission coefficient of the barrier, i.e., the probability that an electron arriving at the barrier will tunnel through it. This is given by the Fowler-Nordheim (FN) equation

$$j_F = \frac{1.54 \times 10^{-6} \times 10^{4.52/\sqrt{\phi}} E^2}{\phi} \exp\left(-\frac{6.53 \times 10^9 \phi^{1.5}}{E}\right) \frac{\text{A}}{\text{m}^2}, \quad (1.25)$$

where  $\phi$  is the work function of the metal in units of eV [16].

Real-world surfaces are not perfectly flat. The deformations of a surface lead to an enhancement of the microscopic electric field in their vicinity. As a result, surfaces tend to have sites, called *emitters*, which have higher field emission than the rest of the surface. For simple deformation geometries, the local electric field is multiplied by a factor  $\beta$ , so that the modified FN

equation (1.25) becomes [16]

$$j_F = \frac{1.54 \times 10^{-6} \times 10^{4.52/\sqrt{\phi}} (\beta E)^2}{\phi} \exp\left(-\frac{6.53 \times 10^9 \phi^{1.5}}{\beta E}\right) \frac{\text{A}}{\text{m}^2}. \quad (1.26)$$

The value of  $\beta$  in a high-voltage setup can, theoretically, be found by measuring dark current as a function of the applied electric field, plotting Eq. (1.26), and extracting  $\beta$  from the plot. Typical values of  $\beta$  thus measured range between 40 and 100. Surface features leading to such field enhancement factors, however, have not been observed. In this sense dark current, similarly to vacuum breakdown (see Sec. 1.1), is a phenomenon which is not fully understood [16].

To avoid confusion later in this work, we note that  $\beta$  in Chapters 2-4 describes a field enhancement at the location of nucleation of dislocations, close to, but not on, the surface of a metal. Therefore, while  $\beta$  of the modified FN equation (1.26) and  $\beta$  of the MDDF model are likely related, they are not necessarily identical.

## 1.9 Overview of the Following Chapters

The rest of this dissertation is organized as follows:

In Chapter 2 the MDDF model is presented, drawing on the theoretical concepts introduced in Secs. 1.3-1.7. It is shown how the MDDF model provides, for the first time, a theory which agrees with experimentally observed breakdown rates. In Chapter 3, microscopic observations of electrodes are incorporated into the model. In addition, the model is employed to predict the expected breakdown rates in a number of proposed experiments. This includes an analysis of the effect of the duration of a pulsed electromagnetic field on breakdown rates, which is important in the next-generation linear accelerators.

As mentioned in Sec. 1.8, the description of the prebreakdown state as a metastable state, in which birth-death fluctuations occur around a stable point, led us to predict the existence of spikes in the dark current among electrodes subjected to strong fields. One such phenomenon was discovered in a dedicated setup at CERN, and its behavior was found to be as predicted by the MDDF model. This is described in Chapter 4. Finally, in Chapter 5, we discuss the results of my work, and compare them to my originally proposed research goals.



## CHAPTER 2

# Stochastic Model of Breakdown Nucleation Under Intense Electric Fields

---

E.Z. Engelberg, Y. Ashkenazy, and M. Assaf

Published: Physical Review Letters **120** (2018), 124801

## Stochastic Model of Breakdown Nucleation under Intense Electric Fields

Eliyahu Zvi Engelberg, Yinon Ashkenazy, and Michael Assaf  
*Racah Institute of Physics and the Center for Nanoscience and Nanotechnology,  
 Hebrew University of Jerusalem, Jerusalem 9190401, Israel*



(Received 31 August 2017; published 20 March 2018)

A plastic response due to dislocation activity under intense electric fields is proposed as a source of breakdown. A model is formulated based on stochastic multiplication and arrest under the stress generated by the field. A critical transition in the dislocation population is suggested as the cause of protrusion formation leading to subsequent arcing. The model is studied using Monte Carlo simulations and theoretical analysis, yielding a simplified dependence of the breakdown rates on the electric field. These agree with experimental observations of field and temperature breakdown dependencies.

DOI: [10.1103/PhysRevLett.120.124801](https://doi.org/10.1103/PhysRevLett.120.124801)

Various modern applications rely on maintaining high electric fields in a vacuum between metallic electrodes [1–4]. In such systems, arcing of current through the vacuum, which leads to a field breakdown (BD), is a major failure mechanism. Even when plasma formation is required [5], arcing nucleation and the mechanism leading up to it play a critical role in system design. Therefore, arcing nucleation and vacuum BD are subjects of interest in application and theory.

In most cases, plasma, created by particles emitted from the cathode, leads to arcing [2,6,7]. While the properties of arcing in relation to the interelectrode environment, as well as the development of the cathode and anode surface states, have been previously studied and remain an active and important area of research, the processes in the cathode leading up to BD nucleation are not yet understood [2,4]. It has been postulated that plastic damage to the cathode surface plays a critical role in the nucleation process. Based on this assumption, it was suggested that a BD can be related to the mobility of defects within the solid [8], and thus the mean time to BD  $\tau$  would show an exponential dependence on the stress  $\sigma$ . Assuming that the leading contribution to  $\sigma$  is due to Maxwell stress  $\sigma = \epsilon_0 E^2 / 2$ , where  $E$  is the applied field, led to a  $\ln \tau \sim E^2$  relation. This showed a good fit to a compilation of experimental data on the BD rate ( $BDR \sim 1/\tau$ ) versus  $E$  in metals at room temperature [10].

Understanding the observed limit is of general interest and is important for the design of high gradient applications, specifically in the proposed new CLIC project in CERN [1,4,11]. This led to a concentrated effort to identify the mechanism by which BDs are driven [12,13]. The basic assumption was that an applied field may cause a yield at the surface, which would lead to the formation of a localized protrusion. This protrusion would then enhance the electric current on the surface, leading to heating and thus to plasma formation and arc nucleation. However,

molecular dynamics and finite element simulations showed these processes occurring only at  $E \gtrsim 1$  GV/m [12,13], significantly more than the observed BD fields, in the range of 100–200 MV/m [4,11].

It is well established that plasticity in metals close to the yield is controlled by stochastic dislocation reactions [14]. Individual crystals, too, deform via a sequence of discrete slip events, as was demonstrated in the compression of micropillars [15]. The probability distribution of these events was measured [16] and reproduced by discrete dislocation dynamics simulations [17], as well as mean-field models [18]. Such systems demonstrate universal critical behavior characteristics of a self-organized critical state controlled by a minimally stable cluster, where in this case the cluster is a pinned dislocation arrangement [19,20]. A model reproducing this type of critical behavior utilizes terms describing the kinetics of the mobile dislocation density  $\rho$ , with nucleation at stress concentration sites on free surfaces,  $\dot{\rho}_+$ , as well as their depletion,  $\dot{\rho}_-$  [21]. While not fully descriptive of the complex dislocation system, this model successfully describes the nature and size dependence of the observed stress-strain curves [22,23].

In a similar fashion, it has been shown, using a stochastic model, that the correlated motion of dislocations can lead to micron-sized surface protrusions, when persistent slip bands, caused by cyclic stress, break through the surface [24,25]. This was observed using SEM in fatigued samples exposed to high-cyclic stresses [26,27]. Samples exposed to strong electric fields, however, do not show such prominent features [4].

Here we explore the possibility that the mechanism leading to arc nucleation is a critical transition in the mobile dislocation population density close to the surface. We propose that, in a cathode subjected to an external electric field, the dislocation density typically fluctuates around a stable level, which depends on  $E$ . However, at any point in time, there is a finite probability that the density will reach a

critical point, beyond which it will increase deterministically. Arc nucleation will then follow from the surface response to the sudden localized increase in the surface dislocation density, through a mechanism which we do not attempt to address at this stage.

To explore this option, we employ a zero-dimensional mean-field model to describe the kinetics of the creation and depletion of mobile dislocations in a single slip plane, neglecting interactions between slip planes and the spatial variation of the mobile dislocation density within one plane. In this model, mobile dislocations nucleate at existing sources, and their depletion is due to collisions with obstacles. We formulate the problem in terms of a birth-death master equation [28] for the mobile dislocation population. This formalism is used to calculate an explicit analytical expression for the BDR in one slip plane as a function of  $E$ , which agrees well with kinetic Monte Carlo (KMC) simulations. The resulting model is unique in that, for the first time, it treats a BD in metals as a critical transition, due to the stochastic evolution of dislocations under an external field. In contrast with linear evolution models [10,12,13], our model predicts an eventual BD without requiring observable pre-BD surface features, whose absence in the microscopy of post-BD samples has posed a long-standing problem [4].

We calibrate the model for oxygen-free high-conductivity Cu, due to the availability of experimental data, as it is used in the CERN CLIC Collaboration, developing the next-generation linear collider accelerators. The physical parameters that are unknown are found by fitting the results generated by the model to experimental observations, including the temperature and  $E$  dependence of the BDR. Following this calibration, the model yields a quantitative agreement with the observed experimental BDRs, without making additional assumptions about the physical characteristics of the system, such as postulating the existence of specific surface or subsurface features.

*Deterministic description.*—A simplified kinetic model is based on the average creation and depletion rates  $\dot{\rho}_+$  and  $\dot{\rho}_-$ , respectively [21]. For these, we assume that the kinetics are described within slip planes limited by dislocation cells on the order of  $10 \mu\text{m}$ . Dislocations nucleate at sources, whose density depends on the number of mobile dislocations, at a rate depending on  $E$ . They are depleted by interactions with other mobile dislocations and existing defects. Thus, the deterministic dynamics of the mobile dislocation density are given by

$$\dot{\rho} = \dot{\rho}_+ - \dot{\rho}_-, \quad \dot{\rho}_+ = B_1(\rho + c)\sigma^2 e^{\alpha\sigma}; \quad \dot{\rho}_- = b_2\sigma\rho(\rho + c), \quad (1)$$

with  $\sigma = A_1 + a_2\rho$ . The constants  $A_1$ ,  $a_2$ ,  $B_1$ ,  $b_2$ ,  $c$ , and  $\alpha$  depend on the system parameters and are independent of  $E$ , except for  $A_1 \sim E^2$ . The derivation of these functional forms and the relation of the effective constants to the appropriate physical parameters is described in the

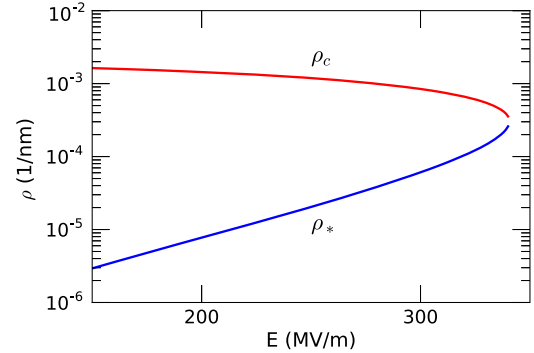


FIG. 1. Fixed points of the dynamical equations for  $\rho$ , attracting ( $\rho_*$ ) and repelling ( $\rho_c$ ), as functions of  $E$ , demonstrating the existence of a bifurcation point.

Supplemental Material; see also Fig. S1 [29]. Henceforth, all analytical and numerical results are presented for fitted parameters (see below).

Below a critical field  $E_c$  (see below), the equation  $\dot{\rho} = 0$  yields two solutions:  $\rho_*$  and  $\rho_c$ , where  $\rho_* < \rho_c$ . For  $\rho_* < \rho < \rho_c$ , we have  $\dot{\rho}_- > \dot{\rho}_+$ , and the dislocation density deterministically decreases back to  $\rho_*$ . Therefore,  $\rho_*$  is an attracting fixed point of Eq. (1), while  $\rho_c$  is a repelling point. That is, if  $\rho$  is larger than  $\rho_c$ , it will increase indefinitely, leading to a subsequent BD.

Sufficiently below  $E_c$ , where  $\rho_* \ll A_1/a_2 \ll \rho_c$ , we can find analytical expressions for  $\rho_*$  and  $\rho_c$ , which yield  $\rho_* = (B_1 A_1 / b_2) e^{\alpha A_1}$  and  $\rho_c = (\alpha a_2)^{-1} \ln[b_2 / (B_1 a_2)]$ .

The values of  $\dot{\rho}_+$  and  $\dot{\rho}_-$  approach each other as  $E$  increases, as shown in Fig. 1. At  $E = E_c$ ,  $\rho_* = \rho_c$ , and thus for  $E \geq E_c$  the system progresses deterministically to a BD. Notably, for  $E < E_c$ , reaching  $\rho_c$  is a fluctuation-driven stochastic event, leading to an  $E$ -dependent BDR.

*Stochastic model.*—To incorporate fluctuations, we model the evolution of the mobile dislocation density  $\rho$  as a birth-death Markov process [28]. The rates  $\dot{\rho}_+$  and  $\dot{\rho}_-$  represent the probability per unit time that  $\rho$  will increase or decrease, respectively, by  $\Delta\rho = 0.1 \mu\text{m}^{-1}$ , corresponding to one dislocation per cell. For one single slip plane, we define  $n = \rho/\Delta\rho$  as the instantaneous number of mobile dislocations per cell. By defining  $A_2 = a_2 n_c \Delta\rho$ ,  $B_2 = b_2 n_c \Delta\rho$ , and  $C = c/(n_c \Delta\rho)$ , where  $n_c = \rho_c/\Delta\rho$ , we find that the microscopic birth and death rates as a function of  $n$  are, respectively,

$$\lambda_n = B_1(n + n_c C)\sigma^2 e^{\alpha\sigma}; \quad \mu_n = (B_2 n / n_c)(n + n_c C)\sigma, \quad (2)$$

with  $\sigma(n) = A_1 + A_2 n / n_c$  [40]. The stochastic dynamics are governed by the master equation

$$\frac{\partial P_n(t)}{\partial t} = \lambda_{n-1} P_{n-1}(t) + \mu_{n+1} P_{n+1}(t) - (\lambda_n + \mu_n)P_n(t), \quad (3)$$

describing the evolution of the probability  $P_n(t)$  of finding  $n$  mobile dislocations per cell at time  $t$  [28].

In order to find the BDR, we write a recursive equation for  $T_n$ , the mean time it takes to reach BD starting from  $n$  mobile dislocations [28,42]:

$$T_n = \frac{\lambda_n}{\lambda_n + \mu_n} T_{n+1} + \frac{\mu_n}{\lambda_n + \mu_n} T_{n-1} + \frac{1}{\lambda_n + \mu_n}, \quad (4)$$

where  $(\lambda_n + \mu_n)^{-1}$  is the average time it takes to jump from  $n$  to  $n \pm 1$ . We solve this equation with an absorbing boundary at  $n_c$  and a reflecting wall at  $n = 0$ , such that  $T_{n_c} = 0$  and  $T'_n(n=0) = 0$ . Starting from the vicinity of  $n = 0$ ,  $\tau$  is given by [43]

$$\tau = T_n = \sum_{i=n}^{n_c} \phi_i \left( \sum_{j=0}^i \frac{1}{\lambda_j \phi_j} \right), \quad (5)$$

with  $\phi_n = \prod_{m=1}^n \mu_m / \lambda_m$  [28].

In the rest of the Letter, we focus on the regime where the critical number of mobile dislocations, needed for a BD, satisfies  $n_c \gg 1$ . In this regime, the expression for  $\tau$  can be simplified. Assuming *a priori* that  $\tau$  is exponentially large in  $n_c$ , we can employ the metastability ansatz  $P_n(t) \simeq \pi_n e^{-t/\tau}$  [44], where  $\pi_n$  is the *quasistationary distribution* (QSD) [41,45–47]. Substituting this into Eq. (3) and neglecting the exponentially small term proportional to  $1/\tau$ , we have  $\lambda_{n-1}\pi_{n-1} + \mu_{n+1}\pi_{n+1} - (\lambda_n + \mu_n)\pi_n = 0$ , whose solution, for  $n \leq n_c$  [48], satisfies [28]

$$\pi_n = \pi_0 \prod_{m=1}^n \frac{\lambda_{m-1}}{\mu_m}. \quad (6)$$

This solution is shown in Fig. 2(a), where  $\pi_0$  is found via normalization [28]. Using Eq. (3) for  $n = n_c + 1$  and the metastability ansatz, we thus have  $\tau \simeq (\lambda_{n_c} \pi_{n_c})^{-1}$  [41, 45–47]. Using Eqs. (2) and (6), expanding in  $n_c \gg 1$ , and applying the Stirling approximation up to subleading order,  $\tau$  gives way to a WKB-like solution [41]

$$\tau = \mathcal{A} e^{n_c \Delta S}, \quad (7)$$

where

$$\begin{aligned} \Delta S &= \ln \frac{B_2}{A_1 B_1} - \alpha A_1 \left( 1 + \frac{1}{2\eta} \right) - (\eta + 1) \ln \left( 1 + \frac{1}{\eta} \right), \\ \mathcal{A} &= \sqrt{\frac{2\pi e^{-\alpha A_1 [1+(1/2\eta)]}}{n_c A_1^2 B_1 C}} \left( 1 + \frac{1}{\eta} \right)^{-1/2}, \end{aligned} \quad (8)$$

and  $\eta = A_1/A_2$ . Here  $n_c \Delta S$  can be viewed as a barrier to a BD [49]. Note that, in the experimentally relevant electric-field range, we observe that

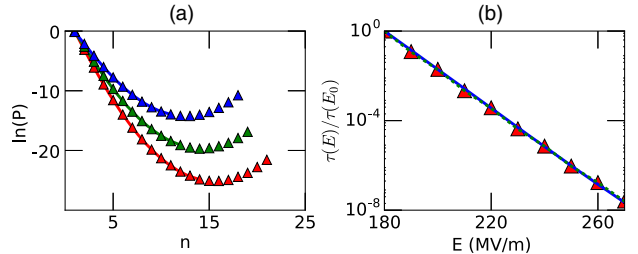


FIG. 2. Analytical versus simulated values: (a) probability of being in state  $n$ , at  $t \ll \tau$ , as calculated from the analytical expression [Eq. (6)] and numerical simulation. The lines, from bottom to top, are for  $E = 200$ , 230, and 260 MV/m. The simulation points include measurements of the probability for  $n > n_c$ , above the QSD validity regime. (b)  $\tau$  normalized by  $\tau(E_0 = 180$  MV/m) as a function of  $E$ , calculated using the metastable approximation [Eq. (7), solid line], the exact formula [Eq. (5), dashed line], and the simulation (triangles).

$$\tau \sim \exp[\gamma(1 - E/E_0)] \quad (9)$$

with  $E_0$  a reference field and  $\gamma$  a dimensionless constant independent of  $E$ , as demonstrated in Fig. 2(b) [50].

The analytical results were compared to a KMC simulation, tracking the time evolution of  $n$ . In this simulation,  $n \rightarrow n \pm 1$  changes randomly using the transition rates in Eq. (2), with the time elapsed between changes determined using an exponential distribution with mean  $(\lambda_n + \mu_n)^{-1}$ . The numerically estimated QSD and  $\tau$  agree with the analytical solution; see Figs. 2 and S2 [29].

*Parameter range.*—The model includes six constants which depend on the material properties and on specific mechanisms that control the reactions of dislocations to the applied field [29]. These constants depend on four unknown parameters: (i)  $\beta$ , relating the stress at the nucleation sites to  $E$ ; (ii)  $\kappa$ , representing temperature-independent factors affecting nucleation, such as the nucleation attempt frequency and activation entropy; (iii) the activation energy  $E_a$ ; and (iv) the activation volume  $\Omega$  for releasing new mobile dislocations.

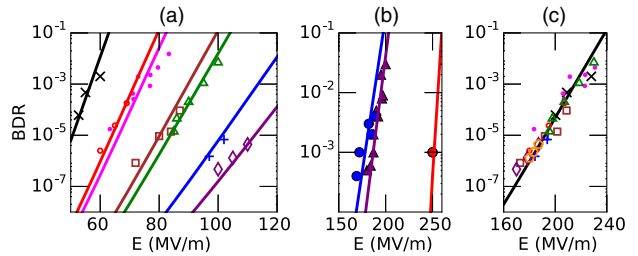


FIG. 3. Experimental BDRs with fitted theoretical lines using Eq. (7): (a) BDR versus  $E$  for various Cu accelerating structures [11]. (b) BDR variation with  $E$  at room temperature (two lines on the left) and at 45 K (line on the right) [51]. (c) BDR versus  $E$  for various Cu accelerating structures [11,52], with  $E$  rescaled so that all measurements are fitted with  $\beta = 4.8$ .

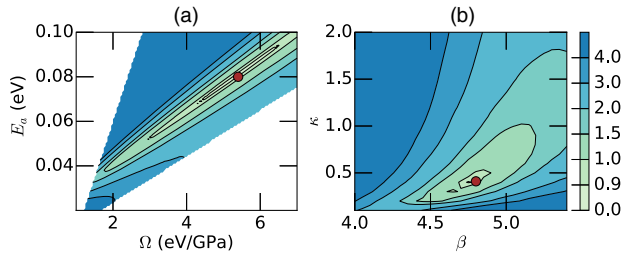


FIG. 4. Fit of free model parameters: (a) LSQ parameter as a function of  $\Omega$  and  $E_a$ , with  $\beta = 4.8$  and  $\kappa = 0.41$ . (b) LSQ parameter as a function of  $\beta$  and  $\kappa$ , with  $\Omega = 5.4$  eV/GPa and  $E_a = 0.08$  eV.

The values of these parameters can be found and validated by a comparison to experimental measurements of the BDR as a function of  $E$  for different structures [11], shown in Fig. 3(a), and for one structure at both room temperature and 45 K [51], shown in Fig. 3(b). The results include measurements from various geometries, leading to a significant variation in the local field at the BD site [11]. As this translates to a variation in  $\beta$  only, results were scaled using  $\beta$  to those of a reference set [52], so that all sets produce identical BDRs at  $E = 180$  MV/m. This led to a single normalized data set shown in Fig. 3(c). As normalization was done for each structure at 300 K, results at 45 K are presented for the rescaled  $E = 250$  MV/m rather than the measured 300 MV/m.

The parameter evaluation was done in two steps: First, a fitting was performed for the reference set [52] and the data from the temperature-varied structure [51], using a least square (LSQ) fit demanding (i) consistency with the experimental values of  $\tau(T = 300$  K,  $E = 180$  MV/m),  $\tau(T = 45$  K,  $E = 300$  MV/m), and  $\gamma(T = 300$  K) of Eq. (9), (ii) consistency with theoretical estimates of  $E_a \gtrsim 0.1$ , and (iii) validity of the approximation  $n_c \gg 1$  at the corresponding temperatures and fields as in (i) [53]. Next, the rest of the data sets [11] were used to validate the quality of the fit. Two cross sections of the resulting LSQ fit in the parameter space ( $\Omega$ ,  $E_a$ ,  $\beta$ ,  $\kappa$ ) are plotted in Fig. 4. We find that the LSQ parameter has a minimum at  $\beta = 4.8 \pm 0.1$ ,  $\kappa = 0.41 \pm 0.02$ ,  $\Omega = 5.4 \pm 0.2$  eV/GPa, and  $E_a = 0.08 \pm 0.002$  eV, marked on the graphs in Fig. 4.

Our results for  $E_a$  are consistent with mobile dislocation nucleation from preexisting sources [54], significantly lower than the activation energy for nucleation in pristine crystalline structures [55–57]. Furthermore, the activation volume  $\Omega = 55b^3$ , with  $b$  the Burgers vector, is within the experimental range  $10b^3 < \Omega < 124b^3$  [54,56].

*Discussion.*—The model can be consistently fitted to all available experimental data sets, with a single free parameter  $\beta$  adjusted to account for the geometrical difference between experimental structures. Thus, the model allows us to make predictions for BDRs over a wide range of physical

parameters beyond those of the current measurements, as demonstrated in Fig. 3.

According to the proposed model, BD nucleation is preceded by a critical increase in the number of mobile dislocations. This can create an early-warning signal for imminent BD through the monitoring of characteristic fluctuations [58], which includes indirect measurements such as thermionic current emissions or direct measurements of acoustic signals from increased fluctuations in the mobile dislocation populations [59]. Furthermore, it is expected that the standard deviation of the QSD, representing the typical fluctuations of the pre-BD mobile dislocation population, will increase significantly as the BD is approached [29].

Conversely, our model does not depend upon the appearance of an observable surface protrusion before a BD. This is in line with the fact that no observable sub-BD features have been observed in metallic electrodes exposed to a strong electric field [4]. BD sites are characterized by a large crater created by the arc [2], obliterating any remains of possible pre-BD features. Such features, however, should have been found further away from the BD site if they existed.

An understanding of the mechanism which leads to BD nucleation can facilitate the development of a better design of electrodes, focusing on limiting the nucleation and mobility of dislocations, in order to lower the BDR. It is well established that, in order to stabilize a significant field, an electrode has to undergo *conditioning* via a series of field exposures and BDs at lower fields [60]. Conditioning includes both an initial extrinsic process (resulting from the removal of contaminants) and a long-term intrinsic process resulting from modifications of the electrode. In line with our model, this comes about as a result of surface hardening [9]. In addition, by controlling the dislocation mobility, our model offers a direction for improving the electrode performance.

In conclusion, we presented a model describing BD nucleation as a stochastic process driven by the creation and depletion of dislocations within the electrode. BD nucleation in this case is a result of a critical transition in the mobile dislocation population density. The model was formulated using a set of parameters describing known material properties and unknown parameters describing interactions specific to the response of the dislocation population to the applied field. Measurements in various fields and temperatures were used to fit the parameters and validate the model. This model is unique, as it does not require pre-BD features, and offers a simple intrinsic mechanism for a BD at fields lower than the deterministic limit. Establishing such a model may provide opportunities for improving the design of future electrodes, aiming to limit the dislocation mobility, as well as offer ways to identify pre-BD early-warning signals through the evolution of the dislocation population.

We acknowledge K. Nordlund, F. Djurabekova, and W. Wuensch for helpful discussions and providing data for Fig. 3. We acknowledge funding from the PAZI foundation.

- 
- [1] P. Burrows, P. Lebrun, L. Linssen, D. Schulte, E. Sicking, S. Stapnes, and M. Thomson, CERN Technical Report No. CERN-2016-004, 2016.
- [2] *Handbook of Vacuum Arc Science and Technology: Fundamentals and Applications*, edited by R. L. Boxman, D. M. Sanders, and P. J. Martin (Noyes, Park Ridge, NJ, 1996).
- [3] P. G. Slade, *The Vacuum Interrupter: Theory, Design, and Application* (CRC, Boca Raton, FL, 2008).
- [4] *High Gradient Accelerating Structure*, edited by W. Gai (World Scientific, Singapore, 2014).
- [5] G. Teel, A. Shashurin, X. Fang, and M. Keidar, *J. Appl. Phys.* **121**, 023303 (2017).
- [6] A. Anders, *Cathodic Arcs: From Fractal Spots to Energetic Condensation*, Springer Series on Atomic, Optical, and Plasma Physics Vol. 50 (Springer, New York, 2008).
- [7] A. Anders, *Surf. Coat. Technol.* **257**, 308 (2014).
- [8] Contaminants and oxide layers can also lead to extrinsic BD nucleation. However, this Letter discusses the rate of intrinsic BDs, which are observed after conditioning processes have removed sources for extrinsic BDs [9].
- [9] W. Wuensch, CERN Technical Report No. CERN-OPEN-2014-028, 2013.
- [10] K. Nordlund and F. Djurabekova, *Phys. Rev. ST Accel. Beams* **15**, 071002 (2012).
- [11] A. Grudiev, S. Calatroni, and W. Wuensch, *Phys. Rev. ST Accel. Beams* **12**, 102001 (2009).
- [12] V. Zadin, A. Pohjonen, A. Aabloo, K. Nordlund, and F. Djurabekova, *Phys. Rev. ST Accel. Beams* **17**, 103501 (2014).
- [13] S. Vigonski, M. Veske, A. Aabloo, F. Djurabekova, and V. Zadin, *Applied Mathematics and Computation* **267**, 476 (2015).
- [14] M. A. Meyers, D. J. Benson, O. Vöhringer, B. K. Kad, Q. Xue, and H.-H. Fu, *Mater. Sci. Eng. A* **322**, 194 (2002).
- [15] M. D. Uchic, P. A. Shade, and D. M. Dimiduk, *Annu. Rev. Mater. Res.* **39**, 361 (2009).
- [16] D. M. Dimiduk, C. Woodward, R. LeSar, and M. D. Uchic, *Science* **312**, 1188 (2006).
- [17] F. F. Csikor, C. Motz, D. Weygand, M. Zaiser, and S. Zapperi, *Science* **318**, 251 (2007).
- [18] N. Friedman, A. T. Jennings, G. Tsekenis, J. Y. Kim, M. Tao, J. T. Uhl, J. R. Greer, and K. A. Dahmen, *Phys. Rev. Lett.* **109**, 095507 (2012).
- [19] S. Papanikolaou, F. Bohn, R. L. Sommer, G. Durin, S. Zapperi, and J. P. Sethna, *Nat. Phys.* **7**, 316 (2011).
- [20] P. Bak, C. Tang, and K. Wiesenfeld, *Phys. Rev. Lett.* **59**, 381 (1987).
- [21] W. D. Nix and S.-W. Lee, *Philos. Mag.* **91**, 1084 (2011).
- [22] I. Ryu, W. D. Nix, and W. Cai, *Acta Mater.* **61**, 3233 (2013).
- [23] I. Ryu, W. Cai, W. D. Nix, and H. Gao, *Acta Mater.* **95**, 176 (2015).
- [24] J. Man, K. Obrtlik, and J. Polák, *Philos. Mag.* **89**, 1295 (2009).
- [25] V. Levitin and S. Loskutov, *Strained Metallic Surfaces* (Wiley-VCH, Weinheim, 2009).
- [26] M. Goto, S. Han, T. Yakushiji, S. Kim, and C. Lim, *International Journal of Fatigue* **30**, 1333 (2008).
- [27] L. Laurent, S. Tantawi, V. Dolgashev, C. Nantista, Y. Higashi, M. Aicheler, S. Heikkinen, and W. Wuensch, *Phys. Rev. ST Accel. Beams* **14**, 041001 (2011).
- [28] C. W. Gardiner, *Handbook of Stochastic Methods* (Springer, Berlin, 2004).
- [29] See Supplemental Material at <http://link.aps.org/supplemental/10.1103/PhysRevLett.120.124801>, which includes Refs. [30–39], for details of the physical model and additional results from the analysis and simulation.
- [30] J. Weertman and J. R. Weertman, *Elementary Dislocation Theory* (MacMillan, New York, 1964).
- [31] W. F. Greenman, T. Vreeland, Jr., and D. S. Wood, *J. Appl. Phys.* **38**, 3595 (1967).
- [32] E. Nadgorny, *Prog. Mater. Sci.* **31**, 1 (1988).
- [33] J. P. Hirth and J. Lothe, *Theory of Dislocations* (Krieger, Malabar, FL, 1982).
- [34] D. Mordehai, Y. Ashkenazy, I. Kelson, and G. Makov, *Phys. Rev. B* **67**, 024112 (2003).
- [35] P. Chatterton, *Proc. Phys. Soc. London* **88**, 231 (1966).
- [36] X. Wang, M. Wang, P. He, Y. Xu, and Z. Li, *J. Appl. Phys.* **96**, 6752 (2004).
- [37] A. Descoedres, Y. Levinson, S. Calatroni, M. Taborelli, and W. Wuensch, *Phys. Rev. ST Accel. Beams* **12**, 092001 (2009).
- [38] G. I. Taylor, *Proc. R. Soc. A* **145**, 362 (1934).
- [39] J. Sevillano, P. van Houtte, and E. Aernoudt, *Prog. Mater. Sci.* **25**, 135 (1980).
- [40] The parameters have been expressed in this form so that we can later conveniently apply a WKB-like perturbation theory with respect to  $n_c \gg 1$  [41].
- [41] M. Dykman, E. Mori, J. Ross, and P. Hunt, *J. Chem. Phys.* **100**, 5735 (1994).
- [42] M. Assaf and B. Meerson, *J. Phys. A* **50**, 263001 (2017).
- [43] Note that, since  $n_* = O(1)$  is an attracting fixed point of Eq. (1), starting from any  $n = O(1)$  in Eq. (5) leads to the same quantitative result.
- [44] Here, once the system has already settled into a long-lived metastable state centered about  $n_*$ , the metastable distribution slowly decays at a rate of  $1/\tau$ , representing the BD probability.
- [45] M. Assaf and B. Meerson, *Phys. Rev. Lett.* **97**, 200602 (2006).
- [46] C. Escudero and A. Kamenev, *Phys. Rev. E* **79**, 041149 (2009).
- [47] M. Assaf and B. Meerson, *Phys. Rev. E* **81**, 021116 (2010).
- [48] Here we assume  $\pi_{n>n_c} \simeq 0$  at  $t \ll \tau$ .
- [49] When  $E \simeq E_c$ , the term  $A_1 \sim E^2$  dominates the exponent. However, in the experimental regime of interest, where the BD is fluctuation driven, all terms in Eq. (8) are of a similar magnitude.
- [50] While the term  $E^2$  provides a reasonable fit to experimentally available data at room temperature [10], a linear dependence provides a better approximation over a wide range of electric fields and temperatures [29].
- [51] A. Cahill, V. Dolgashev, J. Rosenzweig, S. Tantawi, and S. Weathersby, in *Proceedings of the Eighth International*

- Particle Accelerator Conference (IPAC'17), Copenhagen, 2017* (JACoW, Geneva, 2017), pp. 4395–4398.
- [52] W. Wuensch (private communication).
- [53]  $E_a \simeq 0.1$  is the lowest estimate to date of the activation energy of mobile dislocation nucleation [54].
- [54] T. Zhu, J. Li, A. Samanta, A. Leach, and K. Gall, *Phys. Rev. Lett.* **100**, 025502 (2008).
- [55] J. Bonneville, B. Escaig, and J. Martin, *Acta Metall.* **36**, 1989 (1988).
- [56] O. Couteau, T. Kruml, and J. L. Martin, *Acta Mater.* **59**, 4207 (2011).
- [57] S. Ryu, K. Kang, and W. Cai, *Proc. Natl. Acad. Sci. U.S.A.* **108**, 5174 (2011).
- [58] M. Scheffer, J. Bascompte, W. Brock, V. Brovkin, S. Carpenter, V. Dakos, H. Held, E. van Nes, M. Rietkerk, and G. Sugihara, *Nature (London)* **461**, 53 (2009).
- [59] J. Weiss, T. Richeton, F. Louchet, F. Chmelik, P. Dobron, D. Entemeyer, M. Lebyodkin, T. Lebedkina, C. Fressengeas, and R. J. McDonald, *Phys. Rev. B* **76**, 224110 (2007).
- [60] A. Degiovanni, W. Wuensch, and J. Giner Navarro, *Phys. Rev. Accel. Beams* **19**, 032001 (2016).

# Stochastic model of breakdown nucleation under intense electric fields - Supplemental Material

Eliyahu Zvi Engelberg, Yinon Ashkenazy, and Michael Assaf  
*Racah Institute of Physics and the Center for Nanoscience and Nanotechnology,  
 Hebrew University of Jerusalem, Jerusalem 9190401, Israel*  
 (Dated: March 22, 2018)

## CREATION AND DEPLETION RATES

In this section we describe the considerations leading to the formulation of the kinetic equations, leading up to Eq. (1) in the main text.

The rate at which new mobile dislocations are created in a slip plane is determined by the density of sources, which is proportional to the density of in-plane pre-existing defects  $c$  and the mobile dislocation density  $\rho$ . Both of these quantities represent in-plane densities, and therefore are measured in units of  $1/\text{nm}$ . Based on the amount of defects we see in experimental samples, we assign  $c$  a value of  $1 \mu\text{m}^{-1}$ .

In addition, the rate is proportional to the rate of creation of dislocations by each defect. Since the creation of dislocations is thermally activated, the rate should be inversely proportional to a temperature-dependent factor  $\exp[(E_a - \Omega\sigma)/(k_B T)]$ , divided by the creation time of each dislocation. Here  $E_a$  and  $\Omega$  are the activation energy and volume, respectively, of a dislocation nucleation source, whose values we estimate in the main text, while  $\sigma$  is the surface stress of the metal.

To find the attempt frequency of the nucleation, we consider, for convenience, a Frank-Read type source. The creation time of a dislocation in such a source is  $t = L/v$ , with  $L$  the length of the source, and  $v$  the velocity of the dislocation. The threshold stress needed to activate a source of length  $L$  or longer is  $\sigma_{th} = 2Gb/L$ , where  $G = 48 \text{ GPa}$  is the shear modulus, and  $b = 0.25 \text{ nm}$  is the Burgers vector [1]. If the amount of sources decreases rapidly as a function of length, then  $L \approx 2Gb/\sigma$ . For stresses ranging from 0.2 [2, 3] up to 400 MPa [4, 5], the dislocation velocity in Cu is approximately a linear function of  $\sigma$ ,  $v = 50C_t\sigma/G$ , where  $C_t = 2.31 \times 10^3 \text{ m/s}$  is the propagation velocity of sound in Cu [4]. Therefore  $t = G^2b/(25C_t\sigma^2)$ , giving us a total creation rate

$$\dot{\rho}^+ = \frac{25\kappa C_t}{G^2 b} (\rho + c) \sigma^2 e^{-\frac{E_a - \Omega\sigma}{k_B T}}, \quad (1)$$

where  $\kappa$  is a kinetic factor, combining the fraction of mobile dislocations that have been pinned and therefore contribute nucleation sources, and the activation entropy of the sources [6]. We estimate the value of  $\kappa$  in the main text.

Mobile dislocations can be depleted by interactions with other mobile dislocations as well as with pre-existing defects, and ejection to the surface. Assuming that the

last mechanism is considerably slower than the first two, we can write the depletion rate as  $\dot{\rho}^- = \xi\rho v(c + \rho)$ . Here  $\xi$  is a dimensionless proportionality factor, representing trap efficiency. For simplicity, we assign it a value of 1. Substituting once again for  $v$  we have

$$\dot{\rho}^- = \frac{50\xi C_t}{G} \sigma \rho (c + \rho). \quad (2)$$

The stress in metal subjected to an external electric field is composed of the Maxwell stress due to the external field  $E$  applied, and of the average internal stress created by the dislocations themselves. The Maxwell stress is  $\epsilon_0(\beta E)^2/2$ , with the dimensionless parameter  $\beta$  representing the ratio of the effective electric field at the mobile dislocation nucleation site to  $E$ .  $\beta$  is expected to depend both on surface geometry and the electric field distribution. Specifically,  $\beta$  is expected to vary with  $\rho$ , since it depends on the aspect ratio of protrusions created on the surface [7–9]. However, it can be shown by numerical analysis that in the regime of interest, as determined by the values of the rest of the parameters, the aspect ratio remains nearly constant until breakdown. Therefore, we consider it to be a constant over time, whose value we estimate in the main text, for every given cathode geometry.

The second term of the stress is proportional to  $Gb/d$ , where  $d$  is the average distance between dislocations [10, 11]. In the experimental setups examined in the main text, a pulsed electric field is applied, and the breakdown rate (BDR) is constant over time. Since there is no memory effect, we assume a constant sessile dislocation population whose contribution to the total stress from all slip planes saturates. As a result, we take into consideration only the stress caused by the mobile dislocations, whose density varies over time. In multi-slip plane systems  $d$  is proportional to  $\rho^{-1/2}$ , with  $\rho$  measured in units of  $\text{nm}^{-2}$  [10, 11]. However, when considering only one slip plane as in our model, we expect the relation to be  $d \sim \rho^{-1}$ , with  $\rho$  in units of  $\text{nm}^{-1}$ , as described above (and also see below). We therefore find that, altogether, the stress is  $\sigma = \epsilon_0(\beta E)^2/2 + ZGb\rho$ , where the dimensionless parameter  $Z$ , in the second term of the stress, is a structural parameter linking the stress to the dislocation density. For simplicity, we assign it a value of 1.

Defining new constants of the form  $\alpha \equiv \Omega/(k_B T)$ ,  $A_1 \equiv \epsilon_0(\beta E)^2/2$ ,  $a_2 \equiv ZGb$ ,  $B_1 \equiv 25\kappa C_t e^{-\frac{E_a}{k_B T}}/(G^2 b)$ , and  $b_2 \equiv 50\xi C_t/G$ , we arrive at Eq. (1) in the main text.

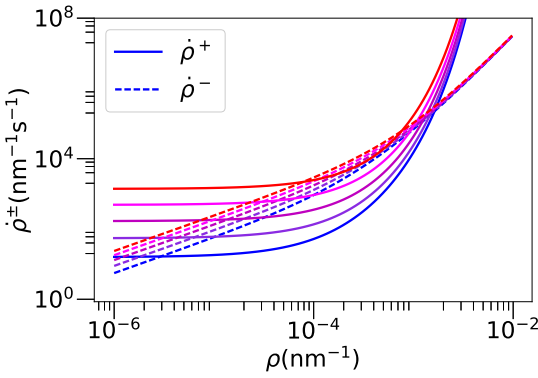


FIG. 1.  $\dot{\rho}^+$  and  $\dot{\rho}^-$  for five electric fields (bottom to top): 150, 190, 230, 270, and 310 MV/m.

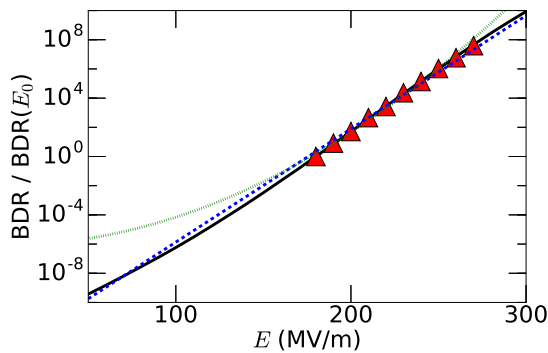


FIG. 2. BDR as a function of the electric field. The solid line is the metastable approximation [Eq. (9) in the main text], the triangles are the simulation results, and the dashed and dotted lines are linear and quadratic fits, respectively.

The values of  $\beta = 4.8 \pm 0.1$ ,  $\kappa = 0.41 \pm 0.02$ ,  $\Omega = 5.4 \pm 0.2$  eV/GPa, and  $E_a = 0.08 \pm 0.002$  eV, found by the fitting procedure in the main text, give us the following values for the constants:  $A_1 = 100 \text{ Pa}(\text{MV/m})^{-2}E^2$ ,  $a_2 = 12 \text{ GPa nm}$ ,  $B_1 = 1850 \text{ MPa}^{-2}\text{s}^{-1}$ ,  $b_2 = 2410 \text{ mGPa}^{-1}\text{s}^{-1}$ ,  $c = 1 \mu\text{m}^{-1}$ ,  $\alpha = 210 \text{ GPa}^{-1}$ . Figure 1 shows the values of  $\dot{\rho}^+$  and  $\dot{\rho}^-$  for the nominal values of the above parameters.

#### LINEAR APPROXIMATION OF THE BDR

For practical purposes it is useful to identify a simple function of the dependence of the BDR on the electric field, which can be later fitted to experimental results. Our results strongly indicate that a linear fit of the logarithm serves as a good approximation over a wide range of electric fields, see Eq. (11) in the main text and Fig. 2 (for fields between 50 and 300 MV/m). Note that the pre-

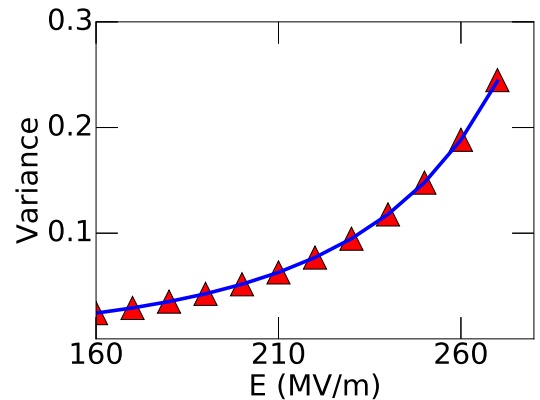


FIG. 3. Variance of the QSD as function of electric field: analytical result (lines), extracted from Eq. (7) in the main text, and simulation (triangles).

viously suggested dependence,  $\tau \sim \exp(\alpha E^2)$  [12], agrees with our model within the range of currently available data but significantly diverges from our results outside that range. However, we stress that our model includes a discernibly different temperature-dependent term, which can be distinguished by dedicated experiments.

#### VARIANCE OF THE QSD

Figure 3 shows the variance of the quasi-stationary distribution (QSD) as a function of the electric field, for the same set of parameters as in Fig. 1. Here the simulation results agree well with a numerical calculation of the variance of the theoretical QSD [Eq. (7) in the main text]. As expected, for stronger fields the variance is larger, and the probability for breakdown increases, since the system moves more rapidly towards higher values of  $n$ . This increase in variance may be experimentally detected through increased variation in related signals such as the acoustic emission signal from moving dislocations within the electrodes, as well as in the dark current produced between them under increasing field.

#### VOLUME DENSITY MODEL

The model developed in this manuscript discusses in-plane mobile dislocation density fluctuations, neglecting interactions between slip planes. The mobile dislocation density  $\rho$  is therefore a two-dimensional density, measured in units of length per area, nm\$^{-1}\$. If we were to define  $\rho$  as the volume density of mobile dislocations in units of length per volume, nm\$^{-2}\$, the average distance between dislocations would be proportional to  $\rho^{-1/2}$  [10, 11]. Then, the stress would be  $\sigma = \epsilon_0(\beta E)^2/2 + ZGb\rho^{1/2}$ . The

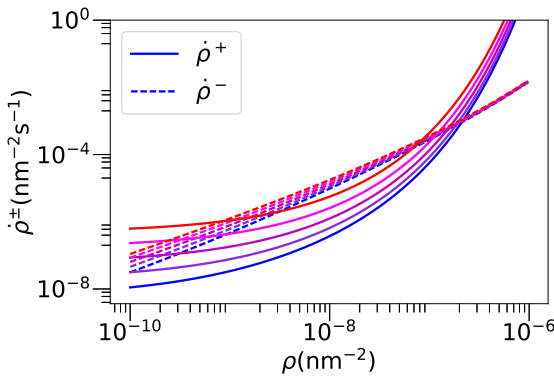


FIG. 4.  $\dot{\rho}^+$  and  $\dot{\rho}^-$  in a model describing volume mobile dislocation density fluctuations, for five electric fields (bottom to top): 150, 190, 230, 270, and 310 MV/m.

creation and depletion rates would be

$$\begin{aligned}\dot{\rho}^+ &= \frac{25\kappa C_t}{G^2 b} (\rho + c)\sigma^2 e^{-\frac{E_a - \Omega\sigma}{k_B T}} \\ \dot{\rho}^- &= \frac{50\xi C_t}{G} \sigma b \rho (c + \rho)\end{aligned}\quad (3)$$

where  $c = 1 \mu\text{m}^{-2}$  is now the volume density of the constant defects, while all other constants retain their original meaning. The factor of  $b$  in the depletion term was added in order to correctly describe the probability of two dislocations interacting, now in a volume instead of a plane, assuming that the width of a dislocation is equal

to the Burgers vector  $b$ .

As seen in Fig. 4, for adjusted values of the parameter set  $\beta$ ,  $\kappa$ ,  $\Omega$ , and  $E_a$ ,  $\dot{\rho}^+$  and  $\dot{\rho}^-$  as volume density creation and depletion rates exhibit the same qualitative behavior as in the two-dimensional density model. The same considerations as in the latter model can then be applied, once again yielding the  $\ln \tau \sim E$  dependence and BDRs as described in the main text.

- 
- [1] J. Weertman and J. R. Weertman, *Elementary Dislocation Theory* (MacMillan, New York, 1964).
  - [2] W. F. Greenman, T. Vreeland, Jr., and D. S. Wood, *J. Appl. Phys.* **38**, 3595 (1967).
  - [3] E. Nadgorny, *Prog. Mater. Sci.* **31**, 1 (1988).
  - [4] J. P. Hirth and J. Lothe, *Theory of Dislocations* (Krieger, Malabar, FL, 1982).
  - [5] D. Mordehai, Y. Ashkenazy, I. Kelson, and G. Makov, *Phys. Rev. B* **67**, 024112 (2003).
  - [6] S. Ryu, K. Kang, and W. Cai, *Proc. Natl. Acad. Sci. U.S.A.* **108**, 5174 (2011).
  - [7] P. Chatterton, *Proc. Phys. Soc.* **88**, 231 (1966).
  - [8] X. Wang, M. Wang, P. He, Y. Xu, and Z. Li, *J. Appl. Phys.* **96**, 6752 (2004).
  - [9] A. Descoedres, Y. Levinsen, S. Calatroni, M. Taborelli, and W. Wuensch, *Phys. Rev. Accel. Beams* **12**, 092001 (2009).
  - [10] G. I. Taylor, *Proc. R. Soc. A* **145**, 362 (1934).
  - [11] J. Sevillano, P. van Houtte, and E. Aernoudt, *Prog. Mater. Sci.* **25**, 135 (1980).
  - [12] K. Nordlund and F. Djurabekova, *Phys. Rev. Accel. Beams* **15**, 071002 (2012).

## CHAPTER 3

# Theory of Electric Field Breakdown Nucleation Due to Mobile Dislocations

---

E.Z. Engelberg, A. Badichi Yashar, Y. Ashkenazy, M. Assaf, and I. Popov

Published: Physical Review Accelerators and Beams **22** (2019), 083501

## Theory of electric field breakdown nucleation due to mobile dislocations

Eliyahu Zvi Engelberg, Ayelet Badichi Yashar, Yinon Ashkenazy,  
Michael Assaf, and Inna Popov

*Racah Institute of Physics and the Center for Nanoscience and Nanotechnology,  
The Hebrew University of Jerusalem, Jerusalem 9190401, Israel*



(Received 19 March 2019; published 7 August 2019)

A model is described in which electrical breakdown in high-voltage systems is caused by stochastic fluctuations of the mobile dislocation population in the cathode. In this model, the mobile dislocation density normally fluctuates, with a finite probability to undergo a critical transition due to the effects of the external field. It is suggested that once such a transition occurs, the mobile dislocation density will increase deterministically, leading to electrical breakdown. Model parametrization is achieved via microscopic analysis of oxygen-free high thermal conductivity Cu cathode samples from the CERN compact linear collider project, allowing the creation and depletion rates of mobile dislocations to be estimated as a function of the initial physical condition of the material and the applied electric field. We find analytical expressions for the mean breakdown time and quasistationary probability distribution of the mobile dislocation density, and verify these results by using a Gillespie algorithm. A least-squares algorithm is used to fit these results with available experimental data of the dependence of the breakdown rate on the applied strength of the electric field and on temperature. The effects of the variation of some of the assumptions of the physical model are considered, and a number of additional experiments to validate the model are proposed, which include examining the effects of the temperature and pulse length, as well as of a time-dependent electric field, on the breakdown rate. Finally, applications of the model are discussed, including the usage of the quasistatic probability distribution to predict breakdowns, and applying the predictions of the model to improve the conditioning process of the cathode material.

DOI: [10.1103/PhysRevAccelBeams.22.083501](https://doi.org/10.1103/PhysRevAccelBeams.22.083501)

### I. INTRODUCTION

The process of plastic deformation in metals is known to be controlled by dislocation dynamics [1,2]. Due to the stochastic nature of these dynamics, plastic deformation can occur even below the yield point of the metal. For example, aging can be observed in metals subjected to cyclic low stresses, due to collective stochastic motion of dislocations. These may lead to strain localization and formation of structures known as persistent slip bands. In particular, the formation of surface features occurs at the surface-slip band intersection [3–7].

Even at stresses close to the yield point, a complete analysis of the dislocation dynamics must take into account the stochastic nature of mobile dislocation nucleation and depletion [8]. For instance, it was shown experimentally and through simulation that the compression of micro-pillars, which can be formed as single crystals with a low

dislocation density, consists of a series of discrete slip events, in which applied stress unpins sessile dislocations and enables them to move to the surface of the crystal [9]. The probability distribution of such events was measured [10] and shown to match simulations [11], and mean field theories were developed which were able to reproduce the stress-strain behavior of the micropillars [12–15].

In a previous study [16] we proposed that stochastic fluctuations of the mobile dislocation density  $\rho$  control a critical process in metallic surfaces subjected to an extreme electric field. This critical process leads to plasma formation between electrodes in vacuum, and to subsequent arcing of current between the electrodes, serving as a major failure mechanism in numerous applications [17–20]. Specifically, arcing between electrodes, known as breakdown, limits the design of linear accelerators, and as such is a focal topic of the prospect study for a future compact linear collider (CLIC) in CERN [21]. CLIC is planned to operate at low breakdown rates (BDRs) with electric fields of 100 MV/m and stronger applied between OFHC Cu electrodes. Since a large amount of experimental results and physical samples from the CLIC project are available for analysis, this manuscript focuses on theoretical estimates for OFHC Cu, the parameters of which are directly derived using samples from the CLIC project. Results from

---

Published by the American Physical Society under the terms of the [Creative Commons Attribution 4.0 International license](#). Further distribution of this work must maintain attribution to the author(s) and the published article's title, journal citation, and DOI.

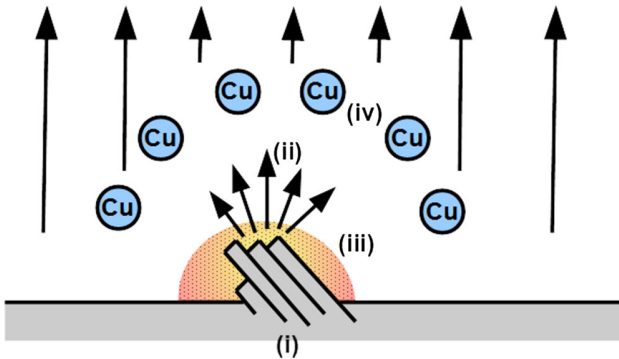


FIG. 1. Schematic description of the stages leading to arcing: (i) Extreme fields generate local stresses which, in turn, lead to dislocation activity, causing mobile dislocations to glide to the surface of the metal and modify it. (ii) The electric field and current on the surface are enhanced due to the surface modifications. (iii) The enhanced current causes heating. (iv) Due to the heating, atoms are released from the cathode and plasma is formed, allowing current to arc between the electrodes.

CLIC consist of data collected both from setups where short radio frequency (rf) electromagnetic pulses are applied [22], and from setups in which the electric field is constant (DC) [23].

The process of arc nucleation under extreme electric fields is understood to be initiated by the glide of mobile dislocations to the surface of the metal, due to local stresses generated by the fields [24]. The mobile dislocations arriving at the surface modify it, thus enhancing the electric field and the current on the surface [25]. The enhanced current then causes heating, which causes atoms to be released from the cathode and to form a plasma [26,27], allowing current to arc between the electrodes [17]. This process is described schematically in Fig. 1.

Previous attempts to explain breakdown nucleation were centered around the formation of distinct protrusions leading to electric field enhancement, evidenced by increased dark currents [28,29]. The enhanced electric field can lead to heating, due to the current and field emission effects after a significant surface protrusion appears [30]. However, the formation process of such protrusions in a metal subject to an electric field has not yet been adequately described theoretically or observed experimentally [19,25,28,29].

Our model, based on mobile dislocation density fluctuations (MDDF) [16], complements these previous models by proposing that surface features appear as a result of a critical increase in the mobile dislocation density  $\rho$ . According to this model, prior to breakdown, the mobile dislocation density is in a long-lived metastable state, fluctuating around a deterministically stable value  $\rho_*$ . When the population experiences a large enough fluctuation to carry the mobile dislocation density beyond a critical value  $\rho_c$ , a critical transition occurs, leading to a deterministic increase in the mobile dislocation density,

which can lead to a localized increase in field emission, due to plastic evolution of the surface. Therefore, the MDDF model describes the process up to the formation of surface deformations, while the subsequent processes of breakdown can be treated by the models previously mentioned [19,25,28,29]. This post-nucleation evolution is not discussed here, and may, as well, not be deterministic. Indeed, there are initial indications from microscopy and current measurements suggesting the existence of subbreakdown events, which may be a result of critical transitions which did not develop into a full-blown breakdown [31].

In this study we extend the MDDF model [16] by including insights from experimental observations pertaining to its physical characteristics and parameters, and discussing their implications for the model. In addition, we present predictions of the model which are relevant for applications in which electric field breakdown is significant.

The manuscript is organized as follows: In Sec. II we present the physical basis of the model, consisting of deterministic rate equations describing the creation and depletion of mobile dislocations in a metal subjected to an electric field. Then, in Sec. III, we describe the problem of finding the BDR in terms of a birth-death master equation [32] for the mobile dislocation population, thereby transforming the problem of calculating the BDR to that of finding the first passage time of a biased random walker. Results of the model are compared to experimental measurements of BDRs in OFHC Cu in Sec. IV, providing estimates of observables such as the activation energy and volume for mobile dislocation nucleation. In Sec. V we examine variations of the physical assumptions of the model, and demonstrate the robustness of the resulting BDR dependence on the electric field. In Sec. VI we propose specific experiments, which can serve to validate the predictions of the model. Finally, in Sec. VII, possibilities for reducing the BDR in real-life applications are discussed.

## II. MEAN-FIELD MODEL

### A. Kinetic equations

Under externally applied stress, dislocations will glide along slip planes [1]. The resulting mobile dislocation density  $\rho$  is expressed as the total length of dislocations in one slip plane, and therefore measured in units of  $\text{nm}^{-1}$ . Mobile dislocations can be blocked by various obstacles, including interactions with other dislocations. Once rendered sessile, dislocations can be released by processes such as cross slip [33]. Thus, barriers serve both as sources and sinks of mobile dislocations.

Figure 2 is a dark-field transmission electron microscopy (TEM) image of a soft OFHC Cu cathode sample from CLIC, under two-beam  $g:220$  diffraction conditions. Dislocation lines are seen to be aligned in a typical ladder-like structure [34] in one active slip plane, which

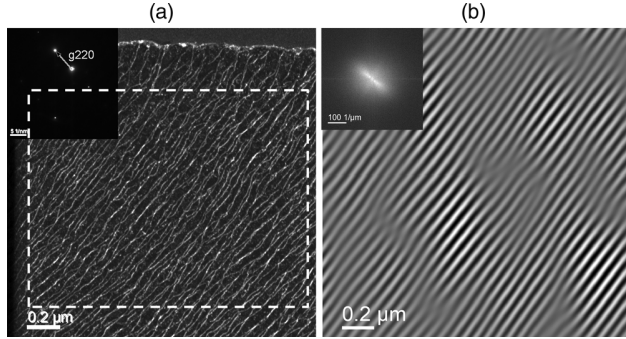


FIG. 2. (a) A dark-field TEM image of a soft OFHC Cu sample ( $\sim 100$  nm thick lamella) under two-beam  $g:220$  diffraction conditions, displaying a typical ladder-like dislocation structure, with the corresponding diffraction pattern (upper left corner). (b) Fourier filtered region enclosed by the dashed rectangle in (a), spatial frequencies farther away than  $\sim 10 \mu\text{m}^{-1}$  from the peak spatial frequency filtered out. The FFT of the region is shown in the upper left corner. The peak spatial frequency corresponds to a transverse distance of 62 nm between dislocation lines.

is parallel to the image plane, and separated from each other by a transverse distance of  $\sim 62$  nm. The density of barriers  $c$  can be estimated from the observed distance between dislocation intersections, which is seen in the figure to be of the order of  $\sim 1 \mu\text{m}$ .

To find the creation and depletion rates of mobile dislocations, we consider a zero-dimensional mean-field model, in which the average value of the mobile dislocation density in one slip plane is calculated. Thus, the effects of variation of the mobile and sessile dislocation density within the slip plane, which would lead to spatial variation of the rates of creation and depletion, are neglected. Also, the variation of the dislocation density and cross interactions among slip planes are not taken into consideration. Cross-interaction effects due to localized surface evolution are not considered either, as these are expected to evolve only following the nucleation of a breakdown event.

When an electromagnetic field is applied, the rate at which new mobile dislocations are created is, therefore, determined by the longitudinal density of barriers  $c$  within the slip plane, and is proportional to the rate of creation of mobile dislocations at each barrier. Since the creation of mobile dislocations is thermally activated, the creation rate should also be proportional to a temperature-dependent factor  $\exp[-(E_a - \Omega\sigma)/(k_B T)]$ , divided by the average creation time of each mobile dislocation. Here  $E_a$  and  $\Omega$  are the activation energy and volume, respectively, of a mobile dislocation nucleation source, whose values we estimate in Sec. IV, while  $\sigma$  is the stress within the slip plane.

The average creation time  $t$  is calculated by considering a typical Frank-Read type source [35]. In such a case  $t = L/v$ , with  $L$  the length of the source, and  $v$  the velocity of the mobile dislocation. The threshold stress needed to activate such a source is  $\sigma_{\text{th}} = 2Gb/L$ , where  $G = 48$  GPa

is the shear modulus, and  $b = 0.25$  nm is the Burgers vector [36]. If the amount of sources decreases rapidly as a function of length, then the dislocation sources can be described using a single  $L \approx 2Gb/\sigma$ . For stresses ranging from 0.2 MPa [37,38], up to 400 MPa [33,39], the dislocation velocity in Cu is approximately a linear function of  $\sigma$ ,  $v = 50C_t\sigma/G$ , where  $C_t = 2.31 \times 10^3$  m/s is the propagation velocity of sound in Cu [33]. Therefore the average creation time satisfies,  $t = G^2b/(25C_t\sigma^2)$ , giving us a total creation rate

$$\dot{\rho}^+ = \frac{25\kappa C_t c}{G^2 b} \sigma^2 \exp\left(-\frac{E_a - \Omega\sigma}{k_B T}\right), \quad (1)$$

where  $\kappa$  is a kinetic factor which depends on the activation entropy of the sources [40], evaluated in Sec. IV.

To estimate the depletion rate of mobile dislocations, we consider dislocation arrest at barriers and surfaces. Assuming that the latter mechanism is considerably slower than the former, we can approximate the depletion rate as  $\dot{\rho}^- = \xi c \rho v$ . Here  $\xi$  is a dimensionless proportionality factor, representing trap efficiency. For simplicity, we assign it a value of 1. Substituting once again for the dislocation velocity  $v$  we have

$$\dot{\rho}^- = \frac{50\xi C_t c}{G} \sigma \rho. \quad (2)$$

## B. In-plane stress

The stress in a slip plane is composed of two terms: the Maxwell stress due to the applied electromagnetic fields  $\mathbf{E}$  and  $\mathbf{B}$ , and the internal stress caused by the dislocations themselves. The Maxwell stress in each direction, i.e., the force in each Cartesian direction per unit area of the surface acting on the particles and fields inside the metal, is given as  $\sum_\beta T_{\alpha\beta} n_\beta$ , with  $T_{\alpha\beta} = \epsilon_0 [E_\alpha E_\beta + c^2 B_\alpha B_\beta - \frac{1}{2}(E^2 + c^2 B^2)\delta_{\alpha\beta}]$ , where  $E_i$  and  $B_i$  are the Cartesian components of the electric and magnetic field, and  $E$  and  $B$  are their respective magnitudes [41]. In the case of a static electric field (DC), the stress inside the slip plane, close to the surface, can be estimated to have a uniform value of  $\epsilon_0(\beta E)^2/2$  in the direction perpendicular to the surface [25]. Here, the dimensionless parameter  $\beta$  represents the ratio of the average stress inside the slip plane to the stress on the surface.  $\beta$  is expected to depend on both surface geometry and the electric field distribution. Specifically, one may expect  $\beta$  to vary with  $\rho$ , since it relates to plastic deformation of the surface [23,42,43]. However, due to the low variation range of  $\rho$  prior to breakdown, we consider  $\beta$  to be constant per cathode geometry (see Sec. IV). This is consistent with the fact that no surface evolution was microscopically observed in prebreakdown samples, as described in Sec. I.

In the case of an alternating electric field (rf), the in-plane stress includes magnetic field terms, and components of

the electric field parallel to the surface, in addition to the contribution of the perpendicular electric field. Above a frequency of 1 GHz, and at subyield stresses, the effect of the fields on the mobility of dislocations can be estimated using the average of the fields over time. The additional components of the stress are then linearly proportional to the perpendicular field, so that their contribution can be incorporated into the value of  $\beta$ .

Note that, due to the nature of the Maxwell stress tensor  $T_{\alpha\beta}$ , stress will be induced in a metal even when it is subject only to a magnetic field. In such a scenario [7], then, breakdown nucleation should be ultimately attributed to the applied magnetic field, since the effects of temperature alone, within experimental ranges, cannot account for breakdown on an initially smooth surface [30].

The second term of the stress, due to the internal stress caused by the dislocations, is proportional to  $Gb/d$ , where  $d$  is the average distance between dislocations [1,44]. In the experimental setups examined in Sec. IV a pulsed electric field is applied, and the BDR is constant over time. Since there is no memory effect, we assume a constant sessile dislocation population whose contribution to the total stress from all slip planes saturates. As a result, we take into consideration only the stress caused by the mobile dislocations, whose density varies over time. In multi-slip-plane systems  $d$  is proportional to  $\rho^{-1/2}$ , with  $\rho$  measured in units of nm<sup>-2</sup> [1,44]. However, when considering only one slip plane as in our model, we expect the relation to be  $d \sim \rho^{-1}$ , with  $\rho$  in units of nm<sup>-1</sup>, as described above (and also see Sec. V). We therefore find that overall, the stress is

$$\sigma = \epsilon_0(\beta E)^2/2 + ZGb\rho, \quad (3)$$

where the dimensionless parameter  $Z$ , in the second term of the stress, is a structural parameter linking the stress to the dislocation density. For concreteness, we assign it a value of 1.

### C. Deterministic fixed points

Defining new constants of the form  $\alpha = \Omega/(k_B T)$ ,  $A_1 = \epsilon_0(\beta E)^2/2$ ,  $a_2 = ZGb$ ,  $B_1 = 25\kappa C_t c \exp[-E_a/(k_B T)]/(G^2 b)$ , and  $b_2 = 50\xi C_t c/G$ , we arrive at

$$\dot{\rho} = \dot{\rho}_+ - \dot{\rho}_-; \quad \dot{\rho}_+ = B_1 \sigma^2 e^{\alpha\sigma}, \quad \dot{\rho}_- = b_2 \sigma \rho, \quad (4)$$

with  $\sigma = A_1 + a_2 \rho$ . As can be seen,  $A_1$  is the only parameter that depends on the strength of the electric field. The values of  $E_a = 0.08 \pm 0.002$  eV,  $\Omega = 5.6 \pm 0.2$  eV/GPa,  $\kappa = 0.32 \pm 0.02$ , and  $\beta = 4.6 \pm 0.1$ , found by the fitting procedure in Sec. IV, give us the following values for the constants:  $A_1 = 94 \text{ Pa}(\text{MV/m})^{-2} E^2$ ,  $a_2 = 12 \text{ GPa nm}$ ,  $B_1 = 0.15 \text{ Pa}^{-2} \text{ m}^{-1} \text{ s}^{-1}$ ,  $b_2 = 2.4 \text{ Pa}^{-1} \text{ s}^{-1}$ , and  $\alpha = 220 \text{ GPa}^{-1}$ . Figure 3 shows the values of  $\dot{\rho}^+$  and  $\dot{\rho}^-$  for

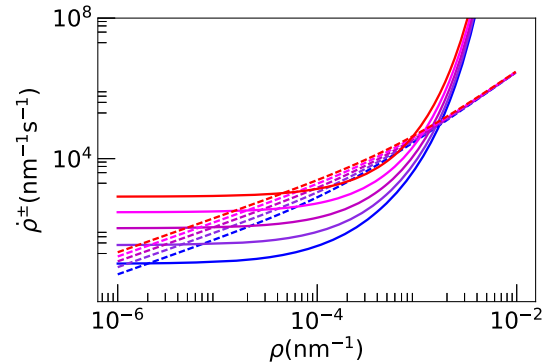


FIG. 3.  $\dot{\rho}^+$  (solid lines) and  $\dot{\rho}^-$  (dashed lines) for five electric fields (bottom to top): 150, 190, 230, 270, and 310 MV/m.

these nominal values. In the rest of this manuscript, unless stated otherwise, the results presented are for these values.

The fixed points can be found in the following way: For  $\rho \ll A_1/a_2$ , we find a stable fixed point at  $\rho_* = (B_1 A_1/b_2) e^{\alpha A_1}$ , while for  $\rho \gg A_1/a_2$ , we find an unstable fixed point at  $\rho_c = (\alpha a_2)^{-1} \ln[b_2/(B_1 a_2)]$ . That is, when  $\rho_* < \rho < \rho_c$  we have  $\dot{\rho}_- > \dot{\rho}_+$ , meaning that the mobile dislocation deterministically returns to the stable attracting point  $\rho_*$ . Whereas, when  $\rho > \rho_c$ , we have  $\dot{\rho}_+ > \dot{\rho}_-$ , meaning that the mobile dislocation density increases beyond  $\rho_c$ , leading to eventual breakdown.

Note that as the electric field increases,  $\rho_*$  and  $\rho_c$  approach each other, and the assumption that  $\rho_* \ll \rho_c$  becomes invalid. The values of  $\rho_*$  and  $\rho_c$  coincide at a bifurcation point, when the electric field is equal to the deterministic breakdown field  $E_b$ . For  $E > E_b$ , we have  $\dot{\rho}_+ > \dot{\rho}_-$  for every  $\rho$ . Therefore, when a field greater than  $E_b$  is applied, the system does not possess a stable fixed point, and it progresses directly to breakdown.

### D. Dislocation cells

Under applied stress, dislocations tend to become organized in a cellular structure, where they are free to glide within each cell, and the cells are separated by an accumulation of sessile dislocations [45]. Figure 4 shows a dark-field scanning transmission electron microscopy (STEM) image of a cross section taken from a soft OFHC Cu electrode which was fully conditioned, meaning that it was exposed to a pulsed electromagnetic field of increasing intensity and pulse length, so that its BDR reached a saturation value. The borders of the cells appear as curled white lines, where each cell is smaller than 10  $\mu\text{m}$ . The cross section was taken from a region which is at least 50  $\mu\text{m}$  away from any breakdown site, demonstrating that the formation of cells is a phenomenon caused by the stress generated by the electric field, and not by the breakdowns themselves.

Assuming the dislocation population evolves independently in each cell, the addition or removal of a single mobile



FIG. 4. A dark-field STEM image of a cross-sectional lamella from a fully conditioned (see main text) OFHC soft Cu electrode, under two-beam g:111 diffraction conditions, showing dislocation cells separated by dislocation walls. The cross section was taken from a region far (at least 50  $\mu\text{m}$  away) from any breakdown site. The dislocation walls appear as curled thin bright lines, as opposed to long straight dislocation segments inside the cells which are organized in a ladderlike structure.

dislocation will modify the mobile dislocation density by approximately  $\Delta\rho = 0.1 \mu\text{m}^{-1}$ . Since breakdown is a surface phenomenon, we propose that it is driven by the mobile dislocation population behavior in the cells adjacent to the surface.

### III. STOCHASTIC MODEL

#### A. Birth-death Markov process

Rate equation (4) demonstrates the existence of two steady-state solutions, but provides no information concerning the rate at which random fluctuations of the mobile dislocation population will carry the system past the critical point. To describe this dynamic behavior, we model the dynamics as a birth-death Markov process [32]. Here the value of  $\rho$  can increase or decrease by  $\Delta\rho$ , with a transition probability per unit time  $\dot{\rho}_+(\rho)/\Delta\rho$  or  $\dot{\rho}_-(\rho)/\Delta\rho$ , respectively. These transitions are independent of the time history of  $\rho$ , and correspond to the creation and pinning, respectively, of one mobile dislocation in one slip plane inside a cell close to the surface. This behavior can be viewed as a biased random walk along the mobile dislocation density axis.

For convenience, we define  $n = \rho/\Delta\rho$ , so that the step size of every transition is  $\pm 1$ . The possible states of the

system are thus described by an integer  $n$ , which assumes values from 0 to  $n_c = [\rho_c/\Delta\rho]$ , where the typical fluctuations are around  $n_* = [\rho_*/\Delta\rho]$ . Defining  $A_2 = a_2 n_c \Delta\rho$  and  $B_2 = b_2 n_c \Delta\rho$ , the birth and death rates of the Markov process are

$$\lambda_n = B_1 \sigma^2 e^{\alpha\sigma}, \quad \mu_n = \frac{B_2 n}{n_c} \sigma \quad (5)$$

with  $\sigma(n) = A_1 + A_2 n/n_c$ . Using these rates, the rate equation can then be written as

$$\dot{n} = \lambda_n(n) - \mu_n(n). \quad (6)$$

The corresponding master equation, describing the time evolution of the probability to be in the state  $n$ , is

$$\frac{\partial P_n(t)}{\partial t} = \lambda_{n-1} P_{n-1}(t) + \mu_{n+1} P_{n+1}(t) - (\lambda_n + \mu_n) P_n(t). \quad (7)$$

Finding the BDR is now equivalent to finding the mean time it takes for the biased random walker to reach  $n_c$ , when starting from the vicinity of  $n_* = O(1)$  [32].

#### B. Estimating the time to breakdown

Given the values of  $\lambda_n$  and  $\mu_n$  for every  $0 \leq n < n_c$ , the mean time to reach  $n_c$  from any state  $n$  can be written recursively as

$$T_n = \frac{\lambda_n}{\lambda_n + \mu_n} T_{n+1} + \frac{\mu_n}{\lambda_n + \mu_n} T_{n-1} + \frac{1}{\lambda_n + \mu_n}. \quad (8)$$

The solution to this equation, with the boundary conditions  $T_{n_c} = 0$  (absorbing state at  $n = n_c$ ) and  $T_0 = T_1 + \lambda_0^{-1}$  (reflecting boundary at  $n = 0$ ), is given, for any  $n < n_c$ , by

$$T_n = \sum_{i=n}^{n_c} \phi_i \left( \sum_{j=0}^i \frac{1}{\lambda_j \phi_j} \right), \quad (9)$$

with  $\phi_n = \prod_{m=1}^n \mu_m / \lambda_m$  [32]. Since the system resides in a long-lived metastable state prior to escape,  $T_n$  is independent of  $n$ , as long as  $n = O(n_*)$ . The lines in Fig. 5, which represent Eq. (9) and various approximations of it, see below, agree well with the values found from numerical simulations, see Appendix A.

#### C. Metastable approximation

The exact solution for  $\tau$ , presented in the previous section [see Eq. (9)], is highly cumbersome. In order to provide insight into the effect of physical constants and parameters on the BDR, it is possible to employ a *metastable* approximation (see below). Starting from some arbitrary initial condition, the system settles after a relaxation time  $t_r$

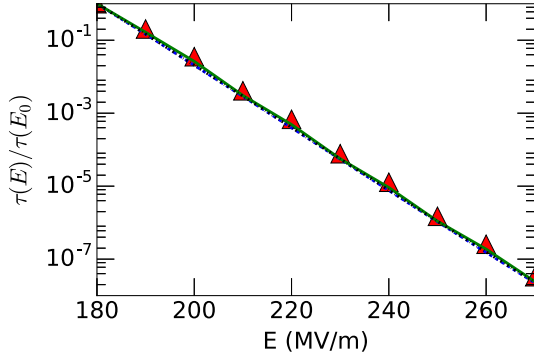


FIG. 5. Mean breakdown time  $\tau$  as a function of the electric field relative to  $\tau(E_0 = 180 \text{ MV/m})$ , calculated using the exact formula [Eq. (9), solid line], the metastable approximation [Eqs. (12) and (14), dashed line], the metastable approximation with an additional Stirling approximation of  $\pi_n$  [Eqs. (14) and (18), dash-dotted line], and the simulation (triangles). The size of the symbols here and in all figures accounts for simulation errors, see Appendix A.

in a metastable state centered about  $n_*$ . Assuming  $t_r \ll \tau$ , we can employ the metastable assumption, where the probability of being absorbed into  $n = n_c$  is given as  $P_{n=n_c}(t) = 1 - e^{-t/\tau}$ , while  $P_{n < n_c}(t) = \pi_n e^{-t/\tau}$ , where  $\pi_n$  is a normalized time-independent *quasistationary* probability distribution (QSD) [46–51].

Substituting the metastable ansatz into Eq. (7) and assuming that  $\tau$  is exponentially large, to be verified *a posteriori*, yields the *quasistationary* master equation

$$\lambda_{n-1}\pi_{n-1} + \mu_{n+1}\pi_{n+1} - (\lambda_n + \mu_n)\pi_n = 0. \quad (10)$$

Together with the fact that  $\mu_0 = 0$  and  $\pi_{n<0} = 0$ , the solution for  $\pi_n$  is

$$\pi_n = \pi_0 \prod_{m=1}^n \frac{\lambda_{m-1}}{\mu_m}, \quad (11)$$

where  $\pi_0$  is found via the normalization condition  $\sum_{n=0}^{n_c-1} \pi_n = 1$  [32]. Substituting the values of  $\lambda_n$  and  $\mu_n$  from Eq. (5) into Eq. (11) yields

$$\begin{aligned} \pi_n &= \pi_0 \frac{n_c \eta}{n + n_c \eta} \left( \frac{A_1 B_1}{B_2 \eta} \right)^n \\ &\times \exp \left[ n \alpha A_1 \left( 1 + \frac{n-1}{2n_c \eta} \right) \right] \frac{\Gamma(n + n_c \eta)}{n! \Gamma(n_c \eta)}, \end{aligned} \quad (12)$$

where  $\eta = A_1/A_2$ , and  $\Gamma(x)$  is the Gamma function.

For the nominal set of parameters, up to the close vicinity of  $E = E_b$ ,  $\pi_0 \gg \pi_{n>0}$ , and therefore  $\pi_0 \approx 1$ . Alternatively, to achieve a more accurate normalization of the distribution, we notice that the maximum of the distribution is obtained at  $n = 0$ , and the width of the distribution is  $O(1)$ .

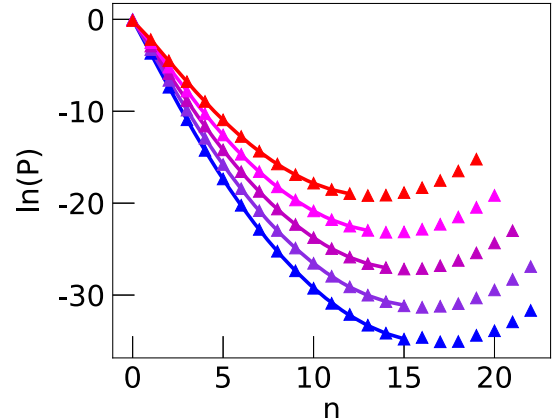


FIG. 6. The probability of being at state  $n$ , calculated from the metastable approximation [Eq. (12), line] and the simulation (triangles) for the nominal parameter set and electric fields of 180, 200, 220, 240, and 260 MV/m (from bottom to top). Here we chose  $n_c + 7$  as an absorbing state, to clearly demonstrate the minimum at  $n = n_c$ , see Appendix A.

As a result, the bulk of the QSD can be found by linearizing the reaction rates close to the maximum, and obtaining  $\lambda_n \approx A_1^2 B_1 e^{\alpha A_1}$  and  $\mu_n \approx A_1 B_2 n / n_c$ . Using Eq. (11), the approximate QSD resulting from these linear rates is a Poisson distribution with a mean (and variance) of

$$\mathcal{R} = \frac{A_1 B_1}{B_2} n_c e^{\alpha A_1}. \quad (13)$$

Therefore, the normalization factor for the QSD is  $\pi_0 = e^{-\mathcal{R}}$ . Figure 6 shows excellent agreement between the theoretical and simulation results for  $\pi_n$ , for the nominal parameters and five different electric fields.

Since the flux through  $n_c$  determines the escape rate, the mean breakdown time is given by

$$\tau \simeq (\lambda_{n_c} \pi_{n_c})^{-1}, \quad (14)$$

which is found from Eq. (7) for  $n = n_c$ .

Using the Stirling approximation  $\Gamma(z) = (2\pi/z)^{1/2} (z/e)^z$ , the rightmost factor in Eq. (12), containing the Gamma functions, becomes, for  $n = n_c$ ,

$$\frac{\Gamma(n_c + n_c \eta)}{n_c! \Gamma(n_c \eta)} = \frac{1}{\sqrt{2\pi n_c}} (1 + \eta)^{n_c} \left( 1 + \frac{1}{\eta} \right)^{n_c \eta - 1/2}. \quad (15)$$

Therefore,

$$\pi_{n_c} = \frac{e^{-\mathcal{R}}}{\sqrt{2\pi n_c}} \left( 1 + \frac{1}{\eta} \right)^{-3/2} \exp \left( -\frac{\alpha A_1}{2\eta} \right) e^{-n_c \Delta S}, \quad (16)$$

where

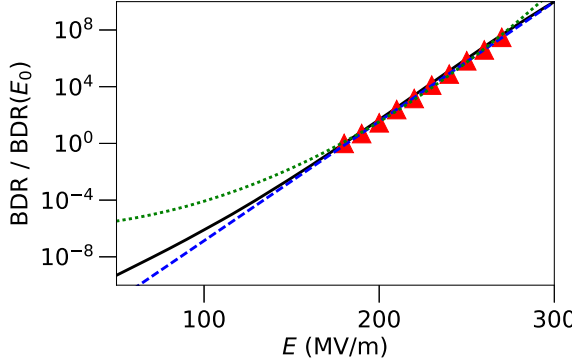


FIG. 7. BDR as a function of the electric field. The solid line is the metastable approximation [Eq. (9) in the main text], the triangles are the simulation results, and the dashed and dotted lines are linear and quadratic fits, respectively, see text.

$$\Delta S = \ln \frac{B_2}{A_1 B_1} - \alpha A_1 \left( 1 + \frac{1}{2\eta} \right) - (\eta + 1) \ln \left( 1 + \frac{1}{\eta} \right). \quad (17)$$

Plugging this result, together with  $\lambda_{n_c}$ , into Eq. (14), yields

$$\tau = \mathcal{A} e^{n_c \Delta S}, \quad (18)$$

with

$$\mathcal{A} = \sqrt{2\pi n_c} \frac{\exp [\mathcal{R} - \alpha A_1 (1 + \frac{1}{2\eta})]}{A_1^2 B_1} \left( 1 + \frac{1}{\eta} \right)^{-1/2}. \quad (19)$$

Here,  $n_c \Delta S$  serves as a barrier that the system needs to overcome in order to enter the breakdown state.

As an alternative to the discrete calculation in Eq. (11), it is possible to employ the WKB ansatz, and express  $\pi_n$  as an exponential function [46,49–51]

$$\pi(q) \sim \exp \{n_c [S(q_*) - S(q)] + S_1(q_*) - S_1(q)\}, \quad (20)$$

where  $q = n/n_c$ ,  $q_* = n_*/n_c$ , and

$$S(q) = - \int^q \ln \frac{w_+(\xi)}{w_-(\xi)} d\xi, \quad S_1(q) = \frac{1}{2} \ln [w_+(q) w_-(q)]. \quad (21)$$

Here  $w_+(q) = \lambda(n_c q)/n_c$  and  $w_-(q) = \mu(n_c q)/n_c$ . Although the WKB approximation is not formally valid when  $n_* = O(1)$  as in our case [49–51], since the barrier for breakdown is large, using Eq. (20) to calculate the QSD and  $\tau$ , for various electric fields, yields results which coincide in the leading order with those of the above method [52].

Our analytical results, given by Eqs. (17)–(19), contain a nontrivial dependence of  $\tau$  on  $E$ . Indeed, while it can be shown that for  $E \simeq E_c$  the term  $A_1 \sim E^2$  dominates the exponent in Eq. (18), for  $E < E_c$ , where breakdown is

fluctuation-driven, our results can be approximated by a linear dependence of  $\ln \tau$  on  $E$ ,

$$\tau \simeq \mathcal{C} \exp[\gamma(1 - E/E_0)]. \quad (22)$$

Here  $E_0$  is a reference field, and  $\gamma$  and  $\mathcal{C}$  are constants independent of  $E$ . This is demonstrated in Figs. 5 and 7 (for fields between 50 and 300 MV/m). Note that, while within the range of currently available data, this behavior is similar to that derived in Ref. [53],  $\tau \sim \exp(\alpha E^2)$ , the models diverge outside that range, see Fig. 7.

#### IV. MODEL FITTING AND VALIDATION

As described in Sec. II, there are four parameters in the MDDF model whose values are not taken from standard properties of the cathode material or estimated from direct observations. The first two of these are the free energy of activation  $E_a$  and the activation volume  $\Omega$  of mobile dislocation nucleation in Eq. (1). The third parameter is  $\kappa$ , see Eq. (1), which is a temperature-independent kinetic prefactor of the rate constant of dislocation nucleation. Finally, the fourth parameter  $\beta$ , in Eq. (3), represents the in-plane effective attenuation or enhancement of the electromagnetic field.

The purpose of this section is to describe the calibration of these four parameters by fitting the results of the model to experimental data of BDRs as a function of the electric field and the temperature. The quality of the fit can serve as a validation of the model, and the resulting values will be compared to previous estimates, and used to predict the results of future experiments.

Most of the available experimental data was acquired from the CLIC prospect study, in which the BDRs are measured in breakdowns per pulse per meter of accelerator (bpp/m). Thus, to translate bpp/m units to the natural characteristic time of the MDDF model, the mean breakdown time per slip plane  $\tau$ , the CLIC accelerator geometry must be taken into consideration. Every meter of the CERN CLIC accelerator is planned to contain 100 cathode irises, in each of which a ring of 2.35 mm diameter and 1 mm width is subjected to the electric field pulse [21]. The surface area of one dislocation cell is approximately  $\Delta\rho^{-2} = 10^{-4}$  mm. Assuming an active slip plane can develop independently in each dislocation cell, the number of active slip planes in one meter of accelerator length is then  $N \approx 1.5 \times 10^7$ . The BDR, in bpp/m, is  $tN/\tau$ , where  $t$  is the time duration of one pulse. With  $t = 230$  ns in the experimental data [22], the resulting conversion of units between the BDR and  $\tau$  is

$$R = 3.45 \frac{\text{bpp s}}{\text{m}} \tau^{-1}. \quad (23)$$

The numerical results of the MDDF model can be compared to experimental data, which consists of sets

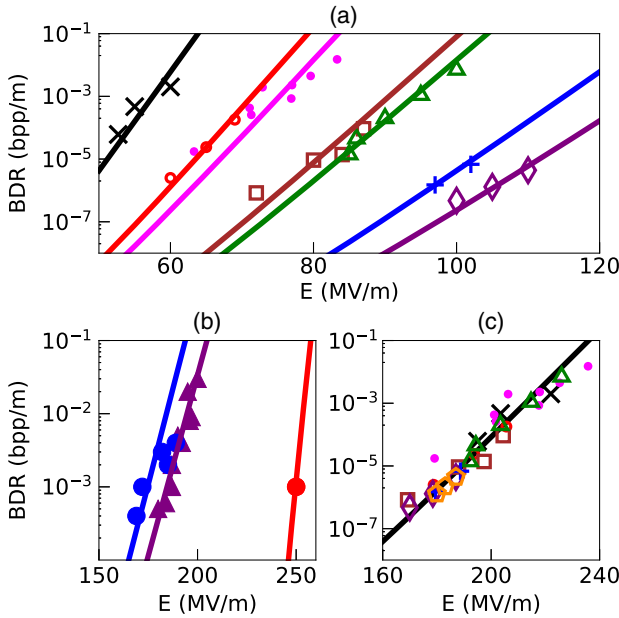


FIG. 8. BDR as a function of the electric field: (a) Group (1) in the text, measured at 300 K in various structures [22]. (b) Group (2) in the text. The two data sets on the left were measured at 300 K, and the set on the right was measured at 45 K [54]. In (a) and (b), the lines represent a fit to the MDDF model with the nominal set of parameters, except for  $\beta$ , which varies among the data sets. (c) Group (3) in the text represented by the yellow pentagons [55], and group (1), with the electric fields scaled, represented by all other symbols. The line in (c) represents a fit to the MDDF model with the nominal set of parameters (including  $\beta$ ).

of measurements of the BDR as a function of the electric field, where each set of measurements was taken in a different physical structure. The sets are divided into three groups: (1) Seven sets measured in different structures in the CERN CLIC project at room temperature [Fig. 8(a)] [22]. (2) Three sets measured at SLAC [Fig. 8(b)]. The two sets on the left of the figure were measured at room temperature (300 K), and the set on the right was measured at 45 K. The leftmost set and the set on the right were measured in the same structure [54]. Although the data set at 45 K consists of a number of measurements, the field varies over a small range. Thus, we consider this data as a single average value. (3) A set measured in the CERN CLIC project [the pentagons in Fig. 8(c)]. This set of data is considered by CLIC to be the most accurate to date [55], and will therefore be used here as a reference set.

Since the parameters  $E_a$ ,  $\Omega$ , and  $\kappa$  should depend on the properties of the material itself, which is identical for all structures, we expect the value of  $\beta$  alone to vary among the structures. Despite the fact that  $\beta$  is not known *a priori* for any structure, it is clear from Eq. (3) that the MDDF model is invariant for a constant  $\beta E$ . Therefore, rescaling the electric field should yield a fit, for all the data sets, with the

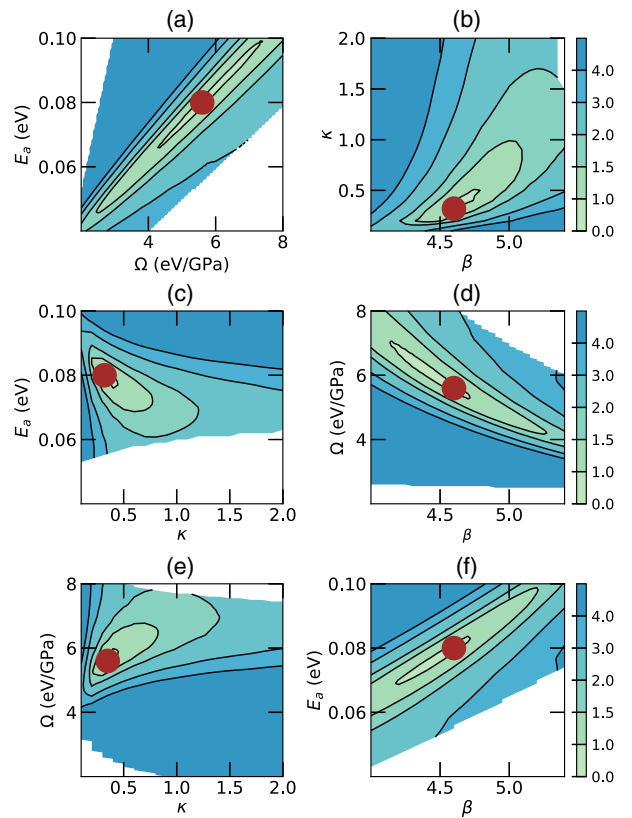


FIG. 9. The LSQ fit measure  $Q$  [see Eq. (B1)] as a function of (a)  $\Omega$  and  $E_a$ , (b)  $\beta$  and  $\kappa$ , (c)  $\kappa$  and  $E_a$ , (d)  $\beta$  and  $\Omega$ , (e)  $\kappa$  and  $\Omega$ , and (f)  $\beta$  and  $E_a$ . In each graph, the two remaining parameters of the set ( $E_a$ ,  $\Omega$ ,  $\kappa$ ,  $\beta$ ) are held at their nominal values. The circle shows the location of the nominal parameter set in the phase space.

same values for all four parameters. Figure 8(c) shows the data sets from group (1) rescaled so that their measured BDRs as a function of the field are all fitted by the same exponential relation as that of the reference set. A LSQ fit to the rescaled data was performed (see Appendix B for details), yielding an optimal fit for the nominal set described in Sec. II, namely  $E_a = 0.08 \pm 0.01$  eV,  $\Omega = 5.6 \pm 0.1$  eV/GPa,  $\kappa = 0.32 \pm 0.01$ , and  $\beta = 4.6 \pm 0.1$ . Figure 9 shows the value of the quality measure of the fit,  $Q$ , for the six two-dimensional cross sections of the four-dimensional phase space ( $E_a, \Omega, \kappa, \beta$ ). The circle shows the location of the nominal parameter set in each cross section.

The activation energy  $E_a = 0.08$  eV is consistent with that previously found for dislocation nucleation from existing sources [56], and considerably lower than the activation energy for dislocation nucleation in configurations with no preexisting sources [40,57,58]. The activation volume is  $\Omega = 5.6$  eV/GPa =  $57b^3$ , with  $b$  the Burgers vector. This result is consistent with experimental results, in which the activation volume was found to be within the range  $10b^3 < \Omega < 124b^3$  [56,58].

## V. SENSITIVITY OF THE MODEL TO PHYSICAL ASSUMPTIONS

In this section we consider possible variations of the physical model, and examine the effect they would have on the predictions of the MDDF model.

### A. Dependence of stress on dislocation density

The MDDF model discusses in-plane mobile dislocation density fluctuations, neglecting interactions between slip planes. The mobile dislocation density  $\rho$  is therefore a two-dimensional density, measured in units of length per area,  $\text{nm}^{-2}$ . In the case where  $\rho$  is defined as the volume density of mobile dislocations in units of length per volume,  $\text{nm}^{-3}$ , the average distance between dislocations is proportional to  $\rho^{-1/2}$  [1,44]. The stress in this case is  $\sigma = \epsilon_0(\beta E)^2/2 + ZGb\rho^{1/2}$ , leading to modified creation and depletion rates [Eqs. (1) and (2)] of

$$\dot{\rho}^+ = \frac{25\kappa C_t c}{G^2 b} \sigma^2 \exp\left(-\frac{E_a - \Omega\sigma}{k_B T}\right), \quad \dot{\rho}^- = \frac{50\xi C_t c}{G} \sigma b \rho \quad (24)$$

where  $c = 1 \mu\text{m}^{-2}$  is now the volume density of the barriers, while all other constants retain their original meaning. The factor of  $b$  in the depletion term was added in order to correctly describe the probability of two dislocations interacting, now in a volume instead of a plane, assuming that the width of a dislocation is equal to the Burgers vector  $b$ .

As seen in Fig. 10(a), for adjusted values of the parameter set  $E_a$ ,  $\Omega$ ,  $\kappa$ , and  $\beta$ , the volume density creation and depletion rates,  $\dot{\rho}^+$  and  $\dot{\rho}^-$ , exhibit the same qualitative behavior as in the two-dimensional density model. The same considerations as in the latter model can then be applied, once again yielding the  $\ln \tau \sim E$  dependence described in Sec. III.

In general, the stress can have a power dependence on the mobile dislocation density of the form  $\sigma = \epsilon_0(\beta E)^2/2 + ZG(b\rho)^\nu$  with some value of  $\nu$ . When considering a volume dislocation density we took  $\nu = 1/2$ , with an additional correction to Eq. (2) due to dimensional considerations. As another example, we examine the case in which  $\nu = 2$ , i.e., the stress is proportional to the two-dimensional dislocation density squared. Here, the value of  $Z$ , the proportionality constant linking the stress to the mobile dislocation density, is expected to be different. Indeed, choosing  $Z = 5 \times 10^4$ , the same qualitative behavior of  $\dot{\rho}^+$  and  $\dot{\rho}^-$  can be produced for the nominal parameters found in Sec. IV, as can be seen in Fig. 10(b).

### B. Effect of sessile and mobile dislocations

Another assumption in the model, justified in Sec. II, is that the stress is affected by the mobile dislocations only. If the stress caused by sessile dislocations contributes

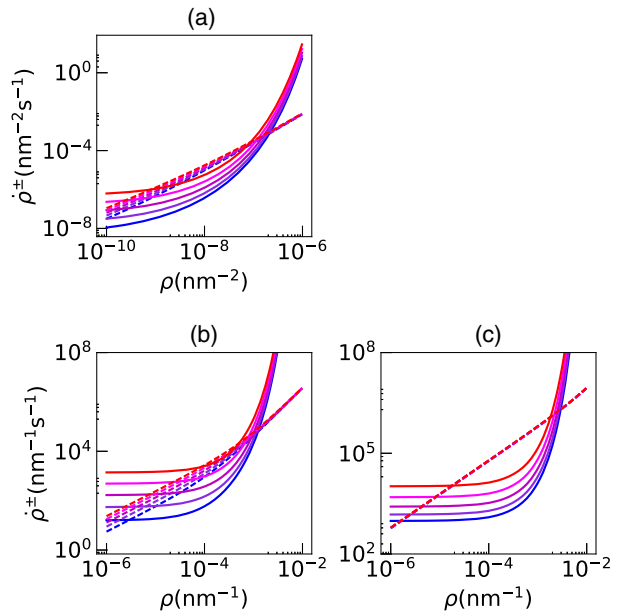


FIG. 10.  $\dot{\rho}^+$  (solid lines) and  $\dot{\rho}^-$  (dashed lines) for the nominal set of parameters and an electric field of (from bottom to top) 150, 190, 230, 270, and 310 MV/m, in (a) a model describing mobile dislocation volume density fluctuations, (b) a model with  $\sigma \sim \rho^2$  (here  $Z = 5 \times 10^4$ ), and (c) a model in which both sessile and mobile dislocations contribute to the average stress.

significantly to the overall stress, Eq. (3) becomes  $\sigma = \epsilon_0(\beta E)^2/2 + Z_m Gb\rho + Z_s Gbs$ , with  $Z_m$  and  $Z_s$  being proportional factors defining the relative contributions of the mobile and sessile dislocations to the stress, respectively, and  $s \approx 20 \mu\text{m}^{-1}$  the density of sessile dislocations (see Sec. II and Fig. 2). Examining the extreme case in which  $Z_m = Z_s = 1$ , a parameter set can be found for which  $\dot{\rho}^+$  and  $\dot{\rho}^-$  exhibit the same qualitative behavior as in the original model, where  $Z_s = 0$ , as seen in Fig. 10(c). Here, too, the calculation yields a  $\ln \tau \sim E$  dependence as in Sec. III.

## VI. PROPOSED EXPERIMENTS

### A. Temperature dependence

As discussed in Sec. IV, experiments to date were carried out primarily at a temperature of 300 K. In calibrating the model to find the unknown parameters, only one measurement point at a different temperature of 45 K was available [54]. However, the model predicts a strong dependence of the BDR on temperature, due to the explicit dependence of  $\alpha$  in Eq. (18) on the temperature, and the fact that  $n_c$  decreases for increasing temperature. Figure 11 shows the dependence of the BDR on the temperature for three electric fields, and Fig. 12 shows the BDR as a function of the electric field for four different temperatures. The effect of the temperature is the most pronounced for weaker electric fields, because the stronger the electric

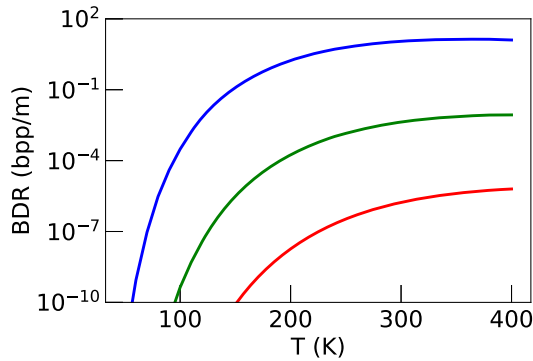


FIG. 11. BDR as a function of the temperature for the nominal parameter set, calculated using the metastable approximation [Eq. (18)]. The lines, from bottom to top, are for fields of 180, 220, and 260 MV/m.

field is, the greater the stress and therefore the lower the activation enthalpy is, thus making the temperature less significant in Eq. (1).

Experiments, supplying data of BDRs at different temperatures and fields, would be instrumental for determining the nature of the temperature dependence of the BDR. This dependence can then be compared to the predictions of the model, and can be used, in addition, to produce more accurate estimates of the activation energy and volume of dislocation nucleation.

### B. Pulse length dependence

As mentioned in Sec. I, the electromagnetic field driving the breakdown, in some applications, is a pulsed rf signal. In the context of the CLIC project, for example, pulse lengths  $t_{\text{pulse}}$  between 50 and 400 ns were examined, with a duty cycle of 50 Hz [59].

Figure 13 shows the cumulative probability distribution function (CDF) of  $t_{\text{tr}}$  in a simulation, with the nominal set of parameters and  $E = 250$  MV/m. Here  $t_{\text{tr}}$  is defined as

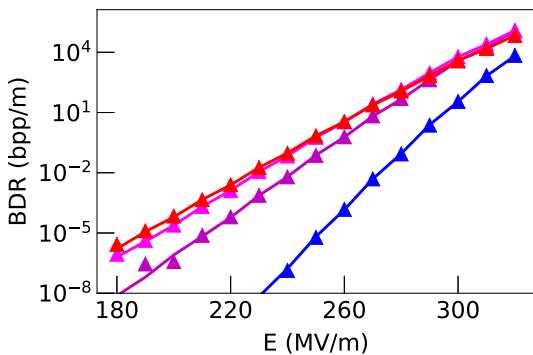


FIG. 12. BDR as a function of the electric field calculated using the exact formula [Eq. (9), lines] and the simulation (triangles). The results are plotted, from bottom to top, for temperatures of 100, 200, 300, and 400 K.

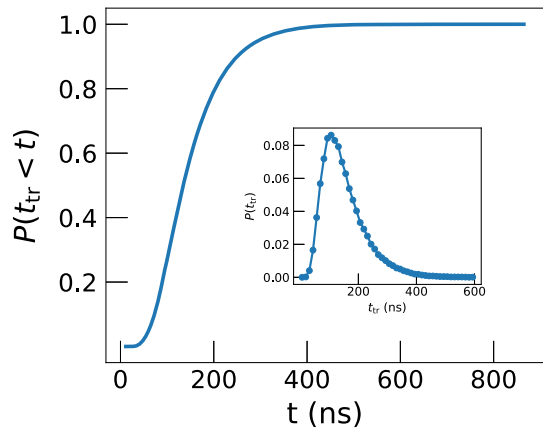


FIG. 13. Cumulative distribution function of the time duration of the trajectory to the critical point  $t_{\text{tr}}$  (see text), for the nominal set of parameters and an electric field of 250 MV/m. The inset shows the probability distribution function, drawn as a histogram of forty-eight bins, each bin 12.5 ns wide. Both curves were found by simulating  $10^5$  breakdown events.

the time it takes to reach the critical point  $n = n_c(E)$ , starting from  $n = n_*(E)$ . For  $t_{\text{pulse}}$  on the order of  $t_{\text{tr}}$  (or shorter), a significant number of trajectories, which would have reached the critical point, will rapidly go to  $n = 0$  once the field is switched off. Therefore, in this regime, we expect a strong dependence of the BDR on  $t_{\text{pulse}}$ , which can be empirically shown to satisfy

$$R = R_0 + m(t_{\text{pulse}} - t_0)e^{-\delta/t}, \quad (25)$$

see Fig. 14. Here,  $R$  is the BDR, and  $R_0$ ,  $t_0$ ,  $m$ , and  $\delta$  are constants depending on the field.

The BDR was shown, experimentally, to have an exponential or power-law dependence on  $t_{\text{pulse}}$  [22,60,61].

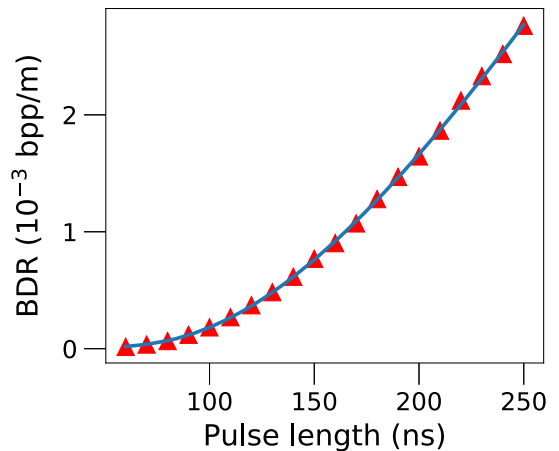


FIG. 14. BDR as a function of the pulse length,  $t_{\text{pulse}}$ , for the nominal set of parameters and an electric field of 250 MV/m, found from the numerical simulations (triangles). The line is a fit to Eq. (25).

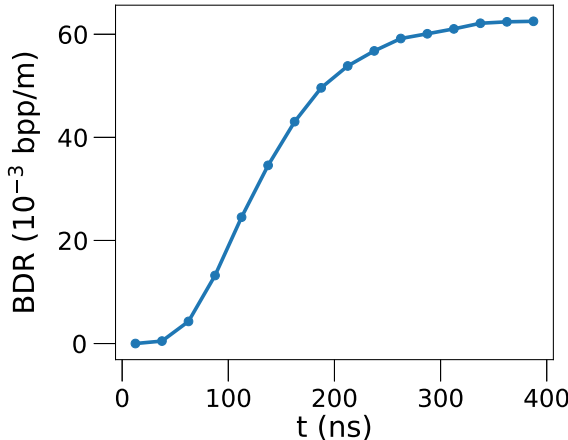


FIG. 15. Probability of a breakdown occurring as a function of the time within the pulse, found by simulation, for the nominal set of parameters, an electric field of 250 MV/m, and a total pulse duration of 400 ns. The probability distribution is presented as a histogram of sixteen bins, each bin 25 ns wide, and normalized by the total BDR at 250 MV/m and a pulse length of 400 ns. The total number of breakdowns is  $10^6$ .

However, the validity of using the existing data to determine the dependence is limited, as it consists of either a small sample [60], or of measurements taken during the conditioning process, when the BDR is still dominated by extrinsic processes [61]. At the very least, the BDR is expected to saturate for a continuous-wave rf signal, and therefore the exponential or power-law dependence holds only for a limited range of pulse lengths.

Under the assumption of pulse independence, the distribution of breakdowns in time within each pulse should be an increasing function, due to the finite evolution time  $t_{tr}$ . Figure 15 shows this distribution for  $E = 250$  MV/m and a pulse duration of 400 ns. For a given time interval  $(t, t + dt)$  within a pulse, an event will mature if it began within the time interval  $(t - t_{tr}, t + dt - t_{tr})$ . Given that a breakdown occurred, the probability that it occurred within an interval  $dt$  is, therefore,  $(dt/t_{pulse}) \int_0^t P(t_{tr}) dt_{tr}$ , where  $P(t_{tr})$  is linearly proportional to the probability distribution function shown in the inset of Fig. 13. This integral, however, is simply the CDF of  $t_{tr}$ , and therefore the probability distribution in Fig. 15 is linearly proportional to the CDF in Fig. 13. This non-Poissonian distribution becomes predominantly Poissonian for times that are significantly greater than  $t_{tr}$ .

If, however, the interval between pulses is smaller than the typical relaxation time, then the breakdown probability should not depend on the pulse duration alone, but rather on the combined effect of exposure to the field and the relaxation achieved between pulses. In this case, the variation in the BDR within the pulse can be small, and characterized by a constant probability, similarly to the slow variation observed for  $t > 500$  ns in Fig. 13. Indeed, in Ref. [62] it was shown that the breakdown distribution does not vary

significantly within the pulse. However, an increase in the breakdown probability was observed for one of the structures studied in Ref. [62]. Due to this fact, together with the need to correct for conditioning effects, we chose not to include this data as a constraint on the MDDF model. As explained, if the system does not reach full relaxation between pulses, we expect the BDR to depend on the duty cycle of the pulses, rather than solely on the pulse length. Therefore, experiments involving variation of the duty cycle, as well as further data regarding the pulse-length dependence during and after conditioning, can help determine the exact nature of the pulse-length dependence of the BDR. This may serve to quantify the memory effect between and within pulses.

### C. Field ramping

Traditionally, kinetic processes leading to transitions have been studied by varying the driving force at a constant rate, measuring changes in the observed transition rate [63]. In general, increasing the electric field at a constant rate  $\chi$  leads to a corresponding mean breakdown field  $E_{BD}(\chi)$ . Using the  $\tau(E)$  dependence from Eq. (22) for constant fields, we find that, if the field at time  $t$  is  $E$ , the upper limit of the mean breakdown time is  $t + \tau[E(t)]$ . Then, from Eq. (22) and the relation  $t = E/\chi$ , the upper limit of the mean field at which breakdown occurs is  $E + \chi C \exp[\gamma(1 - E/E_0)]$ . Assuming an adiabatic increase of  $E$ , i.e.,  $\chi\tau \ll E$ , we can use this upper limit as an estimate of the mean breakdown field. The lowest upper limit fulfilling this condition for any  $E$  is

$$E_{BD} = \frac{E_0}{\gamma} \left( \gamma - \ln \frac{E_0}{\gamma \chi C} + 1 \right). \quad (26)$$

Figure 16 shows  $E_{BD}$  as a function of the field increase rate  $\chi$  for four temperatures. For each temperature,  $C$  and  $\gamma$  were found from a linear fit to the results of the model for a constant field, and were then used in Eq. (26). Simulated breakdown fields are consistent with (and, as expected, slightly lower than) the results of Eq. (26). All the mean breakdown times corresponding to data points in Fig. 16 are greater than  $2 \times 10^5$  seconds of total field exposure time, equivalent to  $10^{12}$  typical 200 ns pulses.

It can be shown from Eq. (26) that  $\ln \chi$  is a linear function of  $E_{BD}/E_0 - 1$ , and that the slope of this function is  $\gamma$ , as shown in Fig. 17. Hence, the value of  $\gamma$ , for a given structure at a given temperature, can be found experimentally by measuring  $E_{BD}$ . BDRs in the MDDF model are analogous to chemical reaction rates in singly-activated kinetic scenarios. The driving force for the transition is provided in the MDDF model by  $E$ , instead of the temperature  $T$  in the chemical reactions, with  $\gamma$  defining the sensitivity of the BDR to the electric field, in the same way that the activation energy defines the sensitivity of the reaction rate to the temperature. The theoretical results

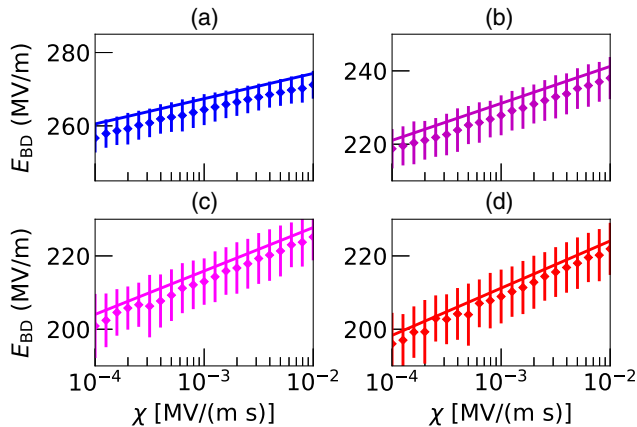


FIG. 16. Mean breakdown field as a function of the field increase rate for a linearly incrementing field, calculated using the metastable approximation [Eqs. (18) and (26), solid line] and the simulation (squares with error bars), for temperatures of (a) 100, (b) 200, (c) 300, and (d) 400 K.

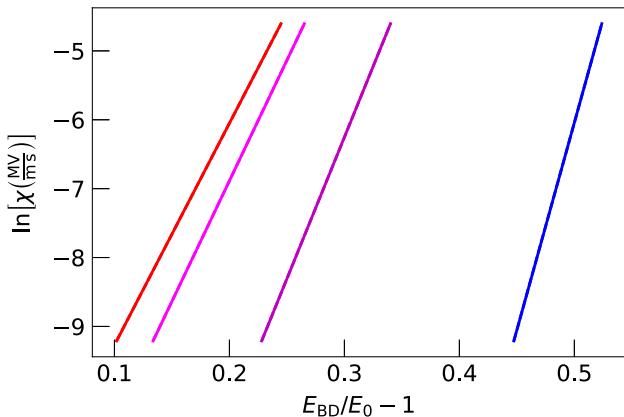


FIG. 17. Logarithm of the field increase rate as a function of  $E_{BD}/E_0 - 1$ , for temperatures of (lines from right to left) 100, 200, 300, and 400 K. Here  $E_{BD}$  is the mean breakdown field, and  $E_0$  is a reference field of 180 MV/m [as in Eq. (22)]. The slopes of the lines, from right to left, are 62.3, 41.7, 35.4, and 32.6, which are the values of  $\gamma$  in Eq. (22) for each of the corresponding temperatures.

described in Fig. 17 can serve as a basis for a future experiment, which will assist in identifying the controlling kinetics. The proposed experiment is analogous to the Kissinger method [63], where the activation energy of a chemical reaction is found by increasing the temperature of a specimen at several constant heating rates, and measuring the exothermic peak temperature  $T_m$  as a function of the heating rate [63].

## VII. DISCUSSION AND CONCLUSIONS

The mobile dislocation density fluctuations (MDDF) model describes the plastic response to an applied field, via

a stochastic process. This early stage evolution can nucleate consequent dynamics, which are described by other models [25–29,53]. In addition, the model defines some unique features of breakdown nucleation, which have not been directly treated by previous models. First, breakdown is a critical process, which develops within several tens of nanoseconds for parameter values around those of the nominal parameters, see Sec. VI. This can explain why prebreakdown surface modifications are not observed in samples, regardless of proximity to the breakdown sites and time of exposure to the field. Second, breakdown occurs deterministically for electric fields greater than  $E_b$ , at which a bifurcation occurs where  $\rho_*$  and  $\rho_c$  merge. Finally, when the time to nucleate breakdown is comparable to the pulse length, the BDR exhibits both a Poissonian and a non-Poissonian regime within each pulse, see Fig. 15. For the nominal parameter set, this time is on the order of several tens of nanoseconds, suggesting BDR reduction for pulse lengths that are shorter than  $O(10)$  ns.

In addition to qualitative observations, the MDDF model yields quantitative estimates, following calibration of the unknown physical parameters, which are in agreement with experimental results. The agreement of the stochastic analysis and simulation results enable the use of the former in cases where running the simulation is prohibitively long. This expands the range of parameters and scenarios in which the predictions of the MDDF model can be applied and put to test. The model was used to predict BDRs outside the currently available experimental data, see Fig. 7 and Sec. VI. Experiments conducted over these ranges, where the predictions of the MDDF model and previous models diverge, can serve to distinguish between models.

Apart from predicting BDRs, the MDDF model can be used to characterize aspects of a system prior to breakdown. Specifically, the QSD of the mobile dislocation density (see Sec. III) can be calculated with the metastable approximation, or from numerical simulations. The standard deviation of the QSD is found to be an increasing function of the electric field, and can be calculated directly from the QSD for each field, see Fig. 18. In addition, a simpler expression of the standard deviation is derived by assuming that the QSD can be approximated as a Poisson distribution in the vicinity of  $n_*$  (see Sec. III), and therefore it can be estimated as the square root of  $\mathcal{R}$  in Eq. (13). This increase with field may be observed experimentally, by measuring acoustic emission signals, or by measuring the dark current between the cathode and anode as a function of the applied electric field [64]. This would allow the development of methods to detect early warning signals of imminent breakdowns [65].

Such methods can be useful as part of the conditioning or other operational schemes. At present, conditioning involves both extrinsic processes in which contaminants are removed from the surface, and intrinsic processes in which the surface structure of the cathode metal is modified [59]. For example,

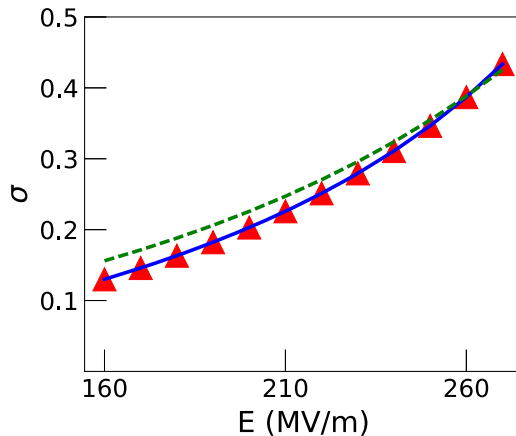


FIG. 18. Standard deviation of the QSD as a function of the electric field, calculated numerically from the QSD of the metastable approximation [Eq. (11), solid line], calculated by treating the QSD approximately as a Poisson distribution [Eq. (13), dashed line], and found from the simulation (triangles).

in the CLIC project, conditioning is done in a test stand reproducing the characteristics of the application setup, and typically takes six months to complete [61]. Combining the ability to monitor early warning signals, together with an understanding of the physical mechanism underlying conditioning, may allow the design of an improved conditioning procedure.

To conclude, a theoretical link between fluctuations in the mobile dislocation density, and its stochastic response to an external field, is offered as a source for the critical process of breakdown under extreme electric fields. The MDDF model developed from this theory is analyzed and shown to provide a good fit to a wide set of experimental data, most of which was made available through the CLIC collaboration, and to direct microscopic observations characterizing the dislocation structure in electrodes. Using the model, expected responses in performed and planned experimental scenarios are presented. We suggest that experiments, utilizing temperature and drive rate variations, can lead to significant improvement in the ability to identify specific mechanisms controlling the critical transition which leads to eventual breakdown. In addition, estimates are made of prebreakdown changes in the evolution of dislocations. Such changes may lead to an observable prebreakdown signal, which is currently under investigation.

## ACKNOWLEDGMENTS

We acknowledge K. Nordlund, F. Djurabekova, W. Wuensch, S. Calatroni, and J. Paszkiewicz for helpful discussions and providing data for Fig. 8. Samples for Figs. 2 and 4 were provided through the CLIC collaboration, with assistance from W. Wuensch, E. Rodriguez Castro, and I. Profatilova. We acknowledge funding from the PAZY Foundation.

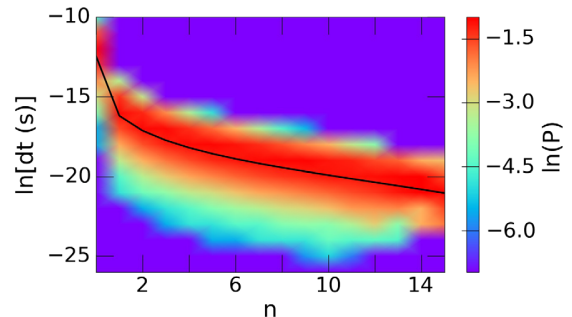


FIG. 19. Probability distribution of the amount of time spent every step, for every  $n$ .

## APPENDIX A: KINETIC MONTE-CARLO SIMULATION

In this Appendix we describe the kinetic Monte-Carlo simulations used to describe the time evolution of the system and to compute the QSD and  $\tau$ . The simulations implement a Gillespie algorithm, tracking a single-step biased random walker along the  $n$  axis. The time spent between adjacent steps is randomly selected from the exponential distribution,  $P = e^{-t/T}/T$ , with  $T = (\lambda_n + \mu_n)^{-1}$  the average time spent between steps in the state  $n$ .

To verify the time calculations in the simulations, a histogram was created detailing, for every value of  $n$ , the distribution of the amount of time spent in every step in which the system was in state  $n$ . This is shown in Fig. 19. The line in the figure represents the theoretical mean time spent at every step. We find that the time distribution is as expected.

To find  $\tau$  as a function of the electric field, the simulations were run at least  $10^2$  times for a number of electric fields, with a reflecting state at  $n = 0$  (i.e.,  $\mu_0 = 0$ ) and an absorbing state at  $n_c$ , as was assumed in the exact and metastable analyses. The time spent at each step, from the beginning of the run until reaching  $n = n_c$ , was summed in order to find the breakdown time of each run. The mean breakdown time  $\tau$  was then calculated by averaging the results of all the runs for that electric field, and the error in  $\tau$  was calculated as the standard deviation of the results. In order to find the QSD, the simulations were run, beginning at  $n = 0$ , for at least  $10^{11}$  steps every time, for a number of electric fields.

## APPENDIX B: LSQ FIT

The logarithm of the BDR in the reference data set depends linearly on the magnitude of the electric field [see Fig. 8(c)]. Comparing this relation to Eq. (22) yields  $\gamma = 31.4$  (at  $T = 300$  K). Using the conversion ratio given by Eq. (23), we also find that  $\log_{10}[R_{\text{hot}}(\text{bpp/m})] = -5.89$ , where  $R_{\text{hot}}$  is the BDR at  $E = 180$  MV/m and  $T = 300$  K.

To incorporate the temperature dependence of the BDR into the parameter fit, we note that the leftmost data set in

TABLE I. Measures and target values for the LSQ fit of the physical parameters [Eq. (B1)].

Measure	Description	Target value	Weight
$\gamma$	Fit to Eq. (22)	31.4	4
$Q_1$	$\log_{10}[R_{\text{hot}}(\text{bpp}/\text{m})]$	-5.89	1
$Q_2$	$\log_{10}(R_{\text{hot}}/R_{\text{cold}})$	1.8	1
$n_{c,\text{hot}}$	$n_c(180 \text{ MV/m}, 300 \text{ K})$	30	1
$n_{c,\text{cold}}$	$n_c(300 \text{ MV/m}, 45 \text{ K})$	15	1
$E_a$	Activation energy	0.1 eV	1

Fig. 8(b) and the single measurement at 45 K must be fitted with the same  $\beta$  since they were both measured in the same structure, or, equivalently, the electric field must be scaled identically in both sets. Scaling the fields, so that the data of the leftmost set matches the fit of the reference set, yields a scaled field of 300 MV/m for the measurement at 45 K. Comparing the BDRs of this measurement and the reference set, we have  $\log_{10}(R_{\text{hot}}/R_{\text{cold}}) \approx 1.8$ , where  $R_{\text{cold}}$  is the BDR at  $E = 300 \text{ MV/m}$  and  $T = 45 \text{ K}$ .

Defining  $Q_1 = \log_{10}[R_{\text{hot}}(\text{bpp}/\text{m})]$  and  $Q_2 = \log_{10}(R_{\text{hot}}/R_{\text{cold}})$ , the LSQ fit was carried out by finding the lowest value of the total quality measure  $Q$  in the four-parameter phase space ( $E_a, \Omega, \kappa, \beta$ ), where

$$Q = 4 \left( \frac{\gamma}{31.4} - 1 \right)^2 + \left( \frac{Q_1}{-5.89} - 1 \right)^2 + \left( \frac{Q_2}{1.8} - 1 \right)^2 + \left( \frac{n_{c,\text{hot}}}{30} - 1 \right)^2 + \left( \frac{n_{c,\text{cold}}}{30} - 1 \right)^2 + \left( \frac{E_a}{0.1 \text{ eV}} - 1 \right)^2. \quad (\text{B1})$$

Here,  $n_{c,\text{hot}}$  is  $n_c$  at  $E = 180 \text{ MV/m}$  and  $T = 300 \text{ K}$ , and  $n_{c,\text{cold}}$  is  $n_c$  at  $E = 300 \text{ MV/m}$  and  $T = 45 \text{ K}$ . These were included in the quality measure because the statistical mean-field analysis and the metastable approximation are valid only when  $n_c \gg 1$ . The target values for these measures were chosen because they are larger than the calculated values in the whole region of the phase space where the parameters have plausible values, so that the larger  $n_{c,\text{hot}}$  and  $n_{c,\text{cold}}$  are, the smaller  $Q$  is. Similarly, the lowest theoretical estimate of  $E_a$  to date is  $\sim 0.1 \text{ eV}$  [56], while within the phase space where the other parameters have plausible values it is found that  $E_a < 0.1$ . Therefore,  $E_a$  was added as a quality measure with a target value of 0.1 eV, so that the greater  $E_a$  is, the smaller  $Q$  is. The value of  $\gamma$  was given greater weight than the other measures as its relative error is smaller by  $\sim 4$  than that of the other measures.

Table I summarizes the measures of the LSQ fit, their target value, and the relative weight of each measure. The optimal set of parameters found from the fit is the nominal set described in Sec. II.

- [1] G. I. Taylor, The mechanism of plastic deformation of crystals. Part I.—Theoretical, *Proc. R. Soc. A* **145**, 362 (1934).
- [2] J. Hirth, A brief history of dislocation theory, *Metall. Trans. A* **16**, 2085 (1985).
- [3] W. Blum and P. Eisenlohr, Dislocation mechanics of creep, *Mater. Sci. Eng. A* **510–511**, 7 (2009).
- [4] J. Man, K. Obrtlik, and J. Polák, Extrusions and intrusions in fatigued metals. Part 1. State of the art and history, *Philos. Mag.* **89**, 1295 (2009).
- [5] V. Levitin and S. Loskutov, *Strained Metallic Surfaces* (Wiley-VCH, Weinheim, 2009).
- [6] M. Goto, S. Han, T. Yakushiji, S. Kim, and C. Lim, Fatigue strength and formation behavior of surface damage in ultrafine grained copper with different non-equilibrium microstructures, *International Journal of Fatigue* **30**, 1333 (2008).
- [7] L. Laurent, S. Tantawi, V. Dolgashev, C. Nantista, Y. Higashi, M. Aicheler, S. Heikkinen, and W. Wuensch, Experimental study of rf pulsed heating, *Phys. Rev. ST Accel. Beams* **14**, 041001 (2011).
- [8] M. A. Meyers, D. J. Benson, O. Vöhringer, B. K. Kad, Q. Xue, and H.-H. Fu, Constitutive description of dynamic deformation: Physically-based mechanisms, *Mater. Sci. Eng. A* **322**, 194 (2002).
- [9] M. D. Uchic, P. A. Shade, and D. M. Dimiduk, Plasticity of micrometer-scale single crystals in compression, *Annu. Rev. Mater. Res.* **39**, 361 (2009).
- [10] D. M. Dimiduk, C. Woodward, R. LeSar, and M. D. Uchic, Scale-free intermittent flow in crystal plasticity, *Science* **312**, 1188 (2006).
- [11] F. F. Csikor, C. Motz, D. Weygand, M. Zaiser, and S. Zapperi, Dislocation avalanches, strain bursts, and the problem of plastic forming at the micrometer scale, *Science* **318**, 251 (2007).
- [12] N. Friedman, A. T. Jennings, G. Tsekenis, J. Y. Kim, M. Tao, J. T. Uhl, J. R. Greer, and K. A. Dahmen, Statistics of Dislocation Slip Avalanches in Nanosized Single Crystals Show Tuned Critical Behavior Predicted by a Simple Mean Field Model, *Phys. Rev. Lett.* **109**, 095507 (2012).
- [13] W. D. Nix and S.-W. Lee, Micro-pillar plasticity controlled by dislocation nucleation at surfaces, *Philos. Mag.* **91**, 1084 (2011).
- [14] I. Ryu, W. D. Nix, and W. Cai, Plasticity of bcc micro-pillars controlled by competition between dislocation multiplication and depletion, *Acta Mater.* **61**, 3233 (2013).
- [15] I. Ryu, W. Cai, W. D. Nix, and H. Gao, Stochastic behaviors in plastic deformation of face-centered cubic micropillars governed by surface nucleation and truncated source operation, *Acta Mater.* **95**, 176 (2015).
- [16] E. Z. Engelberg, Y. Ashkenazy, and M. Assaf, Stochastic Model of Breakdown Nucleation under Intense Electric Fields, *Phys. Rev. Lett.* **120**, 124801 (2018).
- [17] *Handbook of Vacuum Arc Science and Technology: Fundamentals and Applications*, edited by R. L. Boxman, D. M. Sanders, and P. J. Martin (Noyes, Park Ridge, NJ, 1996).
- [18] P. G. Slade, *The Vacuum Interrupter: Theory, Design, and Application* (CRC Press, Boca Raton, FL, 2008).

- [19] W. Gai, *High Gradient Accelerating Structure* (World Scientific, Singapore, 2014).
- [20] G. Teel, A. Shashurin, X. Fang, and M. Keidar, Discharge ignition in the micro-cathode arc thruster, *J. Appl. Phys.* **121**, 023303 (2017).
- [21] P. Burrows, P. Lebrun, L. Linssen, D. Schulte, E. Sicking, S. Stapnes, and M. Thomson, CERN Technical Report No. CERN-2016-004, 2016.
- [22] A. Grudiev, S. Calatroni, and W. Wuensch, New local field quantity describing the high gradient limit of accelerating structures, *Phys. Rev. ST Accel. Beams* **12**, 102001 (2009).
- [23] A. Descoedres, Y. Levinson, S. Calatroni, M. Taborelli, and W. Wuensch, Investigation of the dc vacuum breakdown mechanism, *Phys. Rev. ST Accel. Beams* **12**, 092001 (2009).
- [24] S. Calatroni, A. Descoedres, J. W. Kovermann, M. Taborelli, H. Timko, W. Wuensch, F. Djurabekova, K. Nordlund, A. Pohjonen, and A. Kuronen, in *Proceedings of Linear Accelerator Conference (LINAC'10), Tsukube, Japan* (JACoW, Geneva, 2010), pp. 217–219.
- [25] A. Pohjonen, F. Djurabekova, K. Nordlund, A. Kuronen, and S. Fitzgerald, Dislocation nucleation from near surface void under static tensile stress in Cu, *J. Appl. Phys.* **110**, 023509 (2011).
- [26] A. Anders, *Cathodic Arcs: From Fractal Spots to Energetic Condensation*, Springer Series on Atomic, Optical, and Plasma Physics, Vol. 50 (Springer, New York, 2008).
- [27] A. Anders, A review comparing cathodic arcs and high power impulse magnetron sputtering (HiPIMS), *Surf. Coat. Technol.* **257**, 308 (2014).
- [28] V. Zadin, A. Pohjonen, A. Aabloo, K. Nordlund, and F. Djurabekova, Electrostatic-elastoplastic simulations of copper surface under high electric fields, *Phys. Rev. ST Accel. Beams* **17**, 103501 (2014).
- [29] S. Vigonski, M. Veske, A. Aabloo, F. Djurabekova, and V. Zadin, Verification of a multiscale surface stress model near voids in copper under the load induced by external high electric field, *Appl. Math. Comput.* **267**, 476 (2015).
- [30] A. Kyritsakis, M. Veske, K. Eimre, V. Zadin, and F. Djurabekova, Thermal runaway of metal nano-tips during intense electron emission, *J. Phys. D* **51**, 225203 (2018).
- [31] G. R. Werner, Probing and modeling voltage breakdown in vacuum, Ph.D. thesis, Cornell University, Ithaca, NY (2004), see, e.g., Fig. 7.6.
- [32] C. W. Gardiner, *Handbook of Stochastic Methods* (Springer, Berlin, 2004).
- [33] J. P. Hirth and J. Lothe, *Theory of Dislocations* (Krieger, Malabar, FL, 1982).
- [34] *Plastic Deformation and Fracture of Materials*, edited by H. Mughrabi, Materials Science and Technology: A Comprehensive Treatment (Wiley-VCH, Weinheim, 1992), Vol. 6.
- [35] F. C. Frank and W. T. Read, Multiplication processes for slow moving dislocations, *Phys. Rev.* **79**, 722 (1950).
- [36] J. Weertman and J. R. Weertman, *Elementary Dislocation Theory* (Macmillan, New York, 1964).
- [37] W. F. Greenman, T. V. Jr., and D. S. Wood, Dislocation mobility in copper, *J. Appl. Phys.* **38**, 3595 (1967).
- [38] E. Nadgornyi, Dislocation dynamics and mechanical properties of crystals, *Prog. Mater. Sci.* **31**, 1 (1988).
- [39] D. Mordehai, Y. Ashkenazy, I. Kelson, and G. Makov, Dynamic properties of screw dislocations in Cu: A molecular dynamics study, *Phys. Rev. B* **67**, 024112 (2003).
- [40] S. Ryu, K. Kang, and W. Cai, Entropic effect on the rate of dislocation nucleation, *Proc. Natl. Acad. Sci. U.S.A.* **108**, 5174 (2011).
- [41] J. D. Jackson, *Classical Electrodynamics*, 3rd ed. (Wiley, Hoboken, NJ, 1999).
- [42] P. Chatterton, A theoretical study of field emission initiated vacuum breakdown, *Proc. Phys. Soc.* **88**, 231 (1966).
- [43] X. Wang, M. Wang, P. He, Y. Xu, and Z. Li, Model calculation for the field enhancement factor of carbon nanotube, *J. Appl. Phys.* **96**, 6752 (2004).
- [44] J. Sevillano, P. van Houtte, and E. Aernoudt, 3. The deformed state of metals (II). Structure, *Prog. Mater. Sci.* **25**, 135 (1980).
- [45] R. J. Amodeo and N. M. Ghoneim, A review of experimental observations and theoretical models of dislocation cells and subgrains, *Res mechanica* **23**, 137 (1988).
- [46] M. Dykman, E. Mori, J. Ross, and P. Hunt, Large fluctuations and optimal paths in chemical kinetics, *J. Chem. Phys.* **100**, 5735 (1994).
- [47] V. Elgart and A. Kamenev, Rare event statistics in reaction-diffusion systems, *Phys. Rev. E* **70**, 041106 (2004).
- [48] M. Assaf and B. Meerson, Spectral Theory of Metastability and Extinction in Birth-Death Systems, *Phys. Rev. Lett.* **97**, 200602 (2006).
- [49] C. Escudero and A. Kamenev, Switching rates of multistep reactions, *Phys. Rev. E* **79**, 041149 (2009).
- [50] M. Assaf and B. Meerson, Extinction of metastable stochastic populations, *Phys. Rev. E* **81**, 021116 (2010).
- [51] M. Assaf and B. Meerson, WKB theory of large deviations in stochastic populations, *J. Phys. A* **50**, 263001 (2017).
- [52] S. Be'er, M. Assaf, and B. Meerson, Colonization of a territory by a stochastic population under a strong Allee effect and a low immigration pressure, *Phys. Rev. E* **91**, 062126 (2015).
- [53] K. Nordlund and F. Djurabekova, Defect model for the dependence of breakdown rate on external electric fields, *Phys. Rev. ST Accel. Beams* **15**, 071002 (2012).
- [54] A. Cahill, J. Rosenzweig, V. Dolgashev, S. Tantawi, and S. Weathersby, in *Proceedings of the Eighth International Particle Accelerator Conference (IPAC'17)* (JACoW, Geneva, 2017).
- [55] W. Wuensch (private communication).
- [56] T. Zhu, J. Li, A. Samanta, A. Leach, and K. Gall, Temperature and Strain-Rate Dependence of Surface Dislocation Nucleation, *Phys. Rev. Lett.* **100**, 025502 (2008).
- [57] J. Bonneville, B. Escaig, and J. Martin, A study of cross-slip activation parameters in pure copper, *Acta Metall.* **36**, 1989 (1988).
- [58] O. Couteau, T. Kruml, and J. L. Martin, About the activation volume for cross-slip in Cu at high stresses, *Acta Mater.* **59**, 4207 (2011).
- [59] W. Wuensch, CERN Technical Report No. CERN-OPEN-2014-028, 2013.
- [60] S. Döbert *et al.*, in *Proceedings of 2005 Particle Accelerator Conference (PAC'05), Knoxville, Tennessee* (IEEE, New York, 2005), pp. 372–374.

- [61] A. Degiovanni, W. Wuensch, and J. Giner Navarro, Comparison of the conditioning of high gradient accelerating structures, *Phys. Rev. Accel. Beams* **19**, 032001 (2016).
- [62] X. Wu, J. Shi, H. Chen, J. Shao, T. Abe, T. Higo, S. Matsumoto, and W. Wuensch, High-gradient breakdown studies of an X-band Compact Linear Collider prototype structure, *Phys. Rev. Accel. Beams* **20**, 052001 (2017).
- [63] R. L. Blaine and H. E. Kissinger, Homer Kissinger and the Kissinger equation, *Thermochim. Acta* **540**, 1 (2012).
- [64] J. Weiss, T. Richeton, F. Louchet, F. Chmelik, P. Dobron, D. Entemeyer, M. Lebyodkin, T. Lebedkina, C. Fressengeas, and R. J. McDonald, Evidence for universal intermittent crystal plasticity from acoustic emission and high-resolution extensometry experiments, *Phys. Rev. B* **76**, 224110 (2007).
- [65] M. Scheffer, J. Bascompte, W. Brock, V. Brovkin, S. Carpenter, V. Dakos, H. Held, E. van Nes, M. Rietkerk, and G. Sugihara, Early-warning signals for critical transitions, *Nature (London)* **461**, 53 (2009).



## CHAPTER 4

# Dark Current Spikes as an Indicator of Mobile Dislocation Dynamics Under Intense DC Electric Fields

---

E.Z.Engelberg, J. Paszkiewicz, R. Peacock, S. Lachman, Y. Ashkenazy, and  
W. Wuensch

Published: Physical Review Accelerators and Beams **23** (2020), 123501

# Dark current spikes as an indicator of mobile dislocation dynamics under intense dc electric fields

Eliyahu Zvi Engelberg<sup>1</sup>, Jan Paszkiewicz<sup>2</sup>, Ruth Peacock,<sup>2</sup> Sagy Lachmann,<sup>1</sup>  
Yinon Ashkenazy,<sup>1,\*</sup> and Walter Wuensch<sup>2</sup>

<sup>1</sup>Racah Institute of Physics and the Center of Nanoscience and Nanotechnology,  
The Hebrew University of Jerusalem, Jerusalem 9190401, Israel

<sup>2</sup>CERN, CH-1211 Geneva-23, Switzerland



(Received 28 June 2020; accepted 2 December 2020; published 17 December 2020)

Breakdown of metals subject to intense electric fields is a long-standing limiting factor in high-voltage applications. The mechanism leading to breakdown nucleation is not completely understood. Previously, it was suggested that breakdown can be nucleated by a critical transition in the population of mobile dislocations near the surface of electrodes. This was formulated in terms of a mean-field mobile dislocation density fluctuation (MDDF) model. Based on this model, it was proposed that prebreakdown fluctuations of the mobile dislocation density might be observed as spikes in the dark current between the electrodes. We constructed a setup in which these fluctuations were measured. The rate of fluctuations, as a function of the electric field between the electrodes, agrees with the predictions of the MDDF model, both in functional form and in absolute numerical rates. This numerical agreement was obtained using previously derived numerical parameters of the model. In addition, for each electric field, the distribution of times between current fluctuations was examined. The results indicate that each such prebreakdown fluctuation is the result of a two-step process. This characteristic, too, is in line with the MDDF model, which predicts that a characteristic prebreakdown current event is described as two separate steps in a Markov process, occurring in quick succession.

DOI: 10.1103/PhysRevAccelBeams.23.123501

## I. INTRODUCTION

### A. Vacuum breakdown

High-gradient technologies rely on the maintenance of high voltages between metallic electrodes. In systems sustaining such high voltages, plasma originating from the electrodes can effect an electrical discharge between them. This is called *vacuum arcing*, or *vacuum breakdown*, and is a long-standing problem in high-voltage applications, limiting the obtainable amplitudes of electric and electromagnetic fields [1–4].

The development of quantum mechanics led to the recognition that field emission, in which electrons are released from the electrodes due to the electric field, is a necessary step in the nucleation of vacuum breakdown [5]. However, the precise mechanism leading to breakdown nucleation is not yet understood. This problem has assumed

importance due to the initiation of next-generation linear collider projects, which employ strong radio frequency (rf) electromagnetic fields. In each of these, breakdown has become a limiting factor [6]. An improved understanding of breakdown would be valuable for other fields in which breakdown is relevant, too, as either a desired effect or one to be prevented.

One linear collider project, in which understanding and controlling breakdown are pivotal topics, is the prospect study for the compact linear collider (CLIC) in CERN. CLIC aims to produce rf accelerating gradients of up to 100 MV/m, which will be used to collide a beam of electrons with a beam of positrons. These rf fields are to be produced in pulses of about 200 ns each at a repetition rate of 50 Hz. At the initial stage, in which the length of the linac will be 11.4 km, the collision energy will reach 380 GeV. The present goal at CLIC is to reduce the breakdown rates to  $3 \times 10^{-7}$  breakdowns per pulse per meter (bpp/m) of accelerator length [7].

To investigate breakdowns in an environment which is simpler, and more specifically targeted to their study, direct current (dc) setups were constructed in CERN and elsewhere. One of these is the large electrodes system (LES) in CERN, in which the experiment to be described in this manuscript was conducted. While some characteristics of

\*yinon.ash@mail.huji.ac.il

Published by the American Physical Society under the terms of the Creative Commons Attribution 4.0 International license. Further distribution of this work must maintain attribution to the author(s) and the published article's title, journal citation, and DOI.

the rf and dc setups obviously differ, many insights gained from dc measurements were shown to be valid in rf systems, too [8–10].

### B. The MDDF model

Surface features have been postulated to be essential in the development of breakdown [11–13]. However, after an initial state of conditioning, breakdown rates normally saturate at an approximately constant level [14,15]. This suggests that breakdown sites are intrinsic and formed during operation, since preexisting surface formations or extrinsic sources would be depleted over time. In addition, prebreakdown surface features have not been observed experimentally [3,11,12,16].

We previously proposed [17,18] that a critical transition in the density of the mobile dislocations within a metal can lead to a rapid increase in local current. This mobile dislocation density fluctuation (MDDF) model provides a description of the initial stage of breakdown nucleation, showing that intense electric fields can cause surface response, thus nucleating breakdown [17,18]. This description is in line with previous suggestions that the electric field and current are enhanced due to the formation of a protrusion, leading to localized heating and plasma formation through evaporation [16,19], and thus to breakdown [1,20,21]. However, in the MDDF model, the localized plastic activity leading to this enhancement is the result of a rapid transition in the mobile dislocation population, which does not produce observable features prior to breakdown. In addition to providing a qualitative explanation of the characteristics of breakdown nucleation, the MDDF model also provides statistical tools to calculate breakdown rates, which are in agreement with experimental observations [17,18,22,23].

### C. Dark current fluctuations

The surface of a metal serves as a potential barrier for its conduction electrons. These electrons can be released by tunneling through the barrier. When a strong electric field is applied to the surface of the metal, *field emission* occurs, in which the amount of electrons released increases rapidly as a function of the field. This creates a *dark current* between electrodes in high-gradient setups, which was recognized as a probable precursor of breakdown. It was further recognized that the electric field might be enhanced at certain locations on electrode surfaces, due to their deformation [24].

In order to investigate this field enhancement, experiments were conducted in which the average dark current was measured in high-gradient setups. The results were then compared to theoretical predictions of the tunneling rate, which took into account possible deformations of the electrode surfaces. This allowed the estimation of the field enhancement factor, which is the amount by which an applied field is increased to a local microscopic value.

Typically, the field enhancement factor was found to have values ranging between 40 and 100 [8,24–26].

As described above, the prebreakdown surface features which would lead to the existence of such field enhancement factors have not been observed, and, in the MDDF model, are not predicted to exist prior to breakdown. However, according to the model, subcritical fluctuations of the mobile dislocation density might be observed as *fluctuations* of the dark current during routine operation [17,18]. For a study of these fluctuations, a measurement of the changes in the dark current, rather than its average value, are necessary. Such measurements have now been carried out at CERN in a dedicated system, and the purpose of this manuscript is to compare their results to the time distribution of fluctuations derived from the MDDF model.

In a previous study, four physical parameters, which were not determined *a priori*, were estimated by carrying out a least squares fit to various measurement sets of breakdown rates as a function of the electric field and temperature [17,18]. Here we demonstrate that the MDDF model, with the same values of parameters obtained from that fit, reproduces the observed dark current fluctuation rates.

The rest of this manuscript is organized as follows: The experimental setup is described in Sec. II, and the resulting measurements are presented in Sec. III. In Sec. IV, the MDDF model is applied to calculate the dark current fluctuation rates, and the resulting predictions are shown to agree with the measurements. Finally, in Sec. V we suggest that this apparent link between dark current fluctuations and breakdown rates can be utilized to improve operational procedures in high voltage setups. We also propose additional experiments, which can further validate the MDDF model and its link to dark current fluctuations.

## II. EXPERIMENTAL SETUP

Measurements of prebreakdown dark currents were performed in the large electrode system (LES) at CERN. The LES is designed to test various electrodes under high-gradient conditions, enabling application of electric fields up to  $\sim 100$  MV/m, in vacuum levels in the range of 1 pbar (see [9,10] for a detailed description). Here we used oxygen-free high conductivity (OFHC) Cu electrodes (grain diameter  $\sim 1$  mm, Ra0.025). Each such electrode was shaped as a cylinder with a diameter of 80 mm, with a circular protrusion of 60 mm diameter from the shoulder. The center of each such protrusion, facing the opposite electrode, featured a machined  $10\text{ mm} \times 1\text{ mm}$  rectangular ridge. A ceramic was placed between the shoulders of the electrodes to maintain a gap of  $60\text{ }\mu\text{m}$  between the ridges. These ridges were initially arranged crosswise, giving about  $1\text{ mm}^2$  area exposed to the high field, and then rotated to be parallel, increasing the area to  $10\text{ mm}^2$  (see Fig. 1). The conditioning process allowed these ridged electrodes to sustain fields of up to 60 MV/m. (This is lower than the typically achieved level in the LES [10],

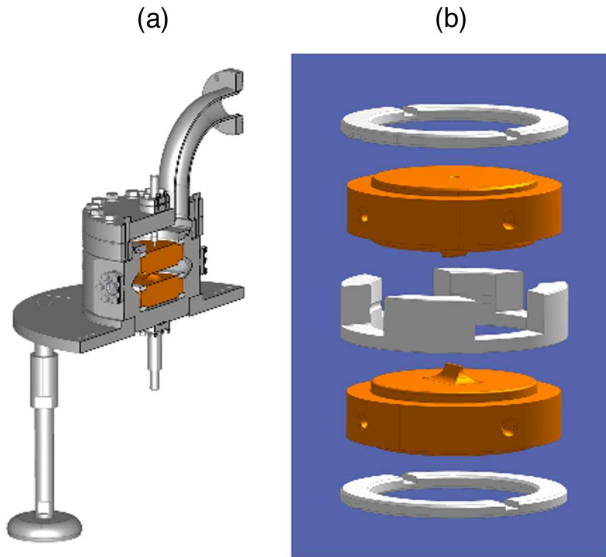


FIG. 1. (a) Sketch of the LES vacuum chamber and (b) detail of the mechanical assembly, holding crossed ridged electrodes.

possibly due to the altered shape of the electrodes.) Applied voltages were limited by this maximum sustainable field, as well as the maximum 1 mA obtainable current.

The electric field between the electrodes can be estimated as  $E = V/d$ , where  $V$  is the applied voltage, and  $d$  is the distance between their ridges [9]. A more detailed estimate can be achieved by simulation. Figure 2 shows the electric field on a plane adjacent to the surface of one of the electrodes, in the vicinity of the area between the ridges, for crossed and parallel ridges. The results in the figure were obtained using CST STUDIO SUITE. The total measured capacitance of the system, when the ridges were parallel, was 87 pF, so the energy stored in the system for, e.g., a voltage of 3 kV, can be estimated as 392  $\mu$ J.

A specialized electric setup, shown in Fig. 3, was used to search for the subcritical fluctuations predicted by the MDDF model. The signal output is capacitively coupled to

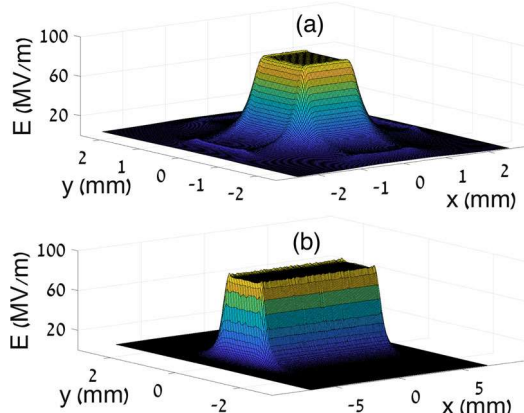


FIG. 2. Electric field adjacent to an electrode surface, in the vicinity of its ridge, for (a) crossed and (b) parallel electrodes. The applied voltage is 5 kV.

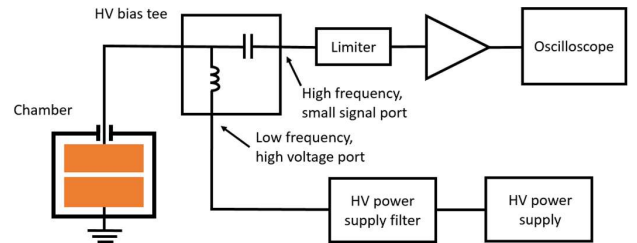


FIG. 3. Block diagram of the setup used to measure dark current fluctuations.

the high-voltage line, followed by input protection and low-noise amplifiers, before being sampled by an oscilloscope, with 1  $\mu$ A of dark current corresponding to approximately 1.75 mV measured by the oscilloscope. The system was designed for a broad bandwidth ( $>1.5$  GHz) and low noise, to account for as large a range of signals as possible, since the characteristics of the signal were not known *a priori*. A power supply filter was added to attenuate any residual electrical noise from the switching behavior of the high-voltage power supply.

In both configurations, measurements of the dark current as a function of time showed pronounced brief current spikes occurring at varying intervals. These unique subcritical prebreakdown events, see, e.g., Fig. 4, consist of a fast transient of  $\sim 50$  ns followed by a decaying sinusoid at  $\sim 2.5$  MHz. The latter is thought to be the resonant response of the setup to the initial current spike. Measurements are performed via capacitive coupling, resulting in a high-pass response which removes the dc component of the dark current. This precludes the differentiation among transient spikes and step changes in the dark current. For obtaining a statistically significant amount of events, a low sampling rate of 5 MHz was used, thus optimizing oscilloscope memory usage (and avoiding the need to process prohibitively large amounts of data). Although this rendered the initial spike too fast to resolve, the 2.5 MHz ringing remained visible, thus allowing to determine the time of occurrence per spike and their ensuing time distribution, which is the focus of this study.

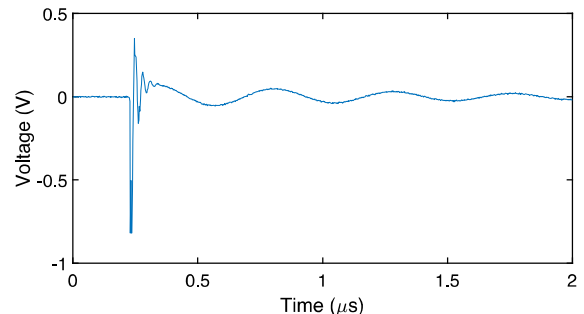


FIG. 4. Example oscilloscope trace of a subcritical (i.e., prebreakdown) current spike, recorded at a high sample rate of 500 MHz.

TABLE I. List of measurement series.

Series	Electrode configuration	Symbol in Fig. 7	$\beta$
A	Crossed	Circles	3.2
B	Crossed	Diamonds	1.8
C	Parallel	Triangles	1.7
D	Parallel	Squares	0.5
E	Parallel	x	0.6

### III. RESULTS

Five series of measurements, as listed in Table I, were performed. Over the course of each series, the applied voltage was varied in steps. An algorithm was applied to assign a time of occurrence to each current spike, avoiding double counting due to the ringing. Using this algorithm the distribution of time intervals between the spikes, for each voltage in each measurement series, was calculated. The cumulative distribution function (CDF) and frequency histogram of these distributions, for a few example voltages in one series, are shown in Figs. 5 and 6, respectively.

For further details of the course of each measurement series and the algorithm used to identify the spikes, see the Appendixes A and B.

Each measured distribution was characterized by an average rate of occurrence of spikes  $r_s$ . This rate as a function of the electric field  $E$ , for every measurement series, is shown in Fig. 7. (Here  $E = V/d$ , as described in Sec. II. The field at the surface of the electrodes can have a different value, due to their shape and surface deformation. This difference is incorporated in the parameter  $\beta$ , see Sec. IV and Refs. [17,18]). The rates in Fig. 7 are given in units of spikes per second per slip plane, under the assumption that an active slip plane can develop in an area of approximately  $\Delta\rho^{-2} = 10^{-4} \text{ mm}^2$  [18].

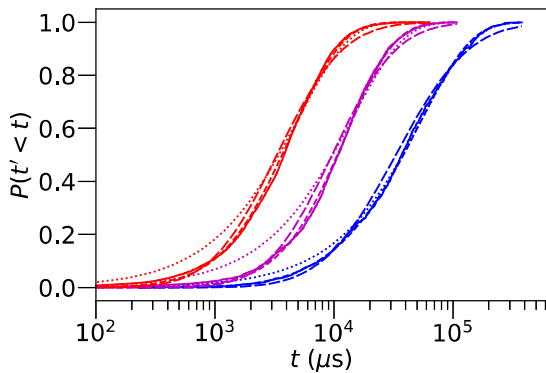


FIG. 5. CDF of the time interval between current spikes for electric fields of 31.3, 35.4, and 39.6 MV/m (from right to left), from series D. For each field, the CDF calculated from experiment is drawn as a solid line. The other lines represent best fits to hypoexponential (dashed), exponential (dotted), and log-normal (dash-dotted) distributions.

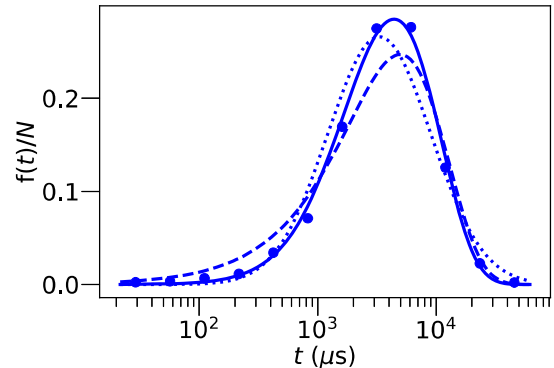


FIG. 6. Histogram of the time interval between current spikes for an electric field of 39.6 MV/m, from series D. The time intervals are divided logarithmically into thirteen bins, and the frequency axis is normalized by the total number of samples. The circles represent the experimental results (with error bars that are smaller than the size of the symbols), and the lines represent best fits to hypoexponential (solid), exponential (dashed), and log-normal (dotted) distributions. The logarithms of the likelihood ratios are  $\ln(L_h/L_e) = 227$  for the hypoexponential and exponential fits, and  $\ln(L_h/L_l) = 466$  for the hypoexponential and log-normal fits.

As seen in Fig. 7, spikes were observed at fields starting from a threshold field  $E_{\text{th}}$ , varying between 21 and 29 MV/m among series, and  $r_s$  was found to be an increasing function of  $E - E_{\text{th}}$ . However, as progressing series of measurements were made, this dependence became milder, and the overall values of  $r_s$  decreased. This decrease over time is in line with the proposal that the current spikes are connected to the breakdown rate, since high-voltage electrodes are known to undergo a conditioning process, in which exposure to strong electromagnetic fields over time makes them less susceptible to subsequent breakdown [9,10,22]. The electric field and vacuum were retained between series, so that the electrodes were

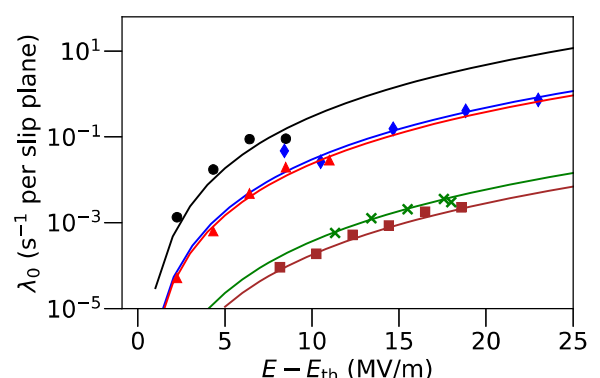


FIG. 7. Rate of current spikes as a function of the electric field, experimental (markers, whose size also accounts for experimental error) and theoretical (lines), for the measurement series listed in Table I. The theoretical lines differ only in the parameter  $\beta$ , as detailed in the table.

continuously being conditioned between them. This long-term conditioning mechanism does not preclude short-term deviations, as observed between series D and E. Indeed, short-term increases of the breakdown rate as a function of the electric field are regularly observed in the conditioning process.

#### IV. COMPARISON TO THEORY

##### A. Theoretical interpretation of current spikes

It was proposed in [18] that fluctuations of the mobile dislocation density within slip planes of a metal, subjected to a strong electric field, can be described as a birth-death Markov process. In this process the density  $n$ , representing the number of mobile dislocations in one slip plane, can change by  $\pm 1$ , normally fluctuating around  $n_* = 0$ , and ranging from 0 to a critical density  $n_c$ . When  $n$  reaches  $n_c$  a critical transition occurs, leading to a runaway increase in  $n$  and, subsequently, to possible breakdown nucleation [17,18].

The corresponding birth and death rates of the Markov process are

$$\lambda_n = \frac{25\kappa C_t c}{G^2 b \Delta\rho} \sigma^2 e^{-\frac{E_a - \Omega\sigma}{k_B T}}; \quad \mu_n = \frac{50\xi C_t c}{G} \sigma n. \quad (1)$$

Here  $\sigma$  is the stress in the slip plane, given by  $\sigma = \epsilon_0(\beta E)^2/2 + ZGb\Delta\rho n$ ,  $T$  is the temperature, and  $E$  is the electric field. The rest of the constants, listed in Table II, are physical values obtained by microscopy, *a priori* physical considerations, and fitting the MDDF theory to measured breakdown rates. It was shown that the variation among experimental structures of the breakdown rates, as a function of the electric field, can be explained as a difference in only one parameter,  $\beta$  [18].

The breakdown rate is clearly not equal to  $r_s$ , since the latter is the rate of a prebreakdown phenomenon. To estimate  $r_s$  we consider that, prior to breakdown, each active slip-plane system is in a metastable state, in which the creation and arrest of mobile dislocations occur regularly. An increase in the density of mobile dislocations, in cells on the surface of the cathode, can be expected to modify the surface structure. This, in turn, may affect the dark current between the electrodes. We therefore consider the possibility that the spikes of dark current can be described in terms of the same kinetic model as that of the breakdown rate.

To analyze this hypothesis quantitatively, we consider an increase in mobile dislocations, i.e., a transition from any state  $n$  to the state  $n + 1$ . The rate of such a transition is given by  $\pi_n \lambda_n$ , where  $\pi_n$  is the value of the quasistatic distribution function (see [17,18]) at  $n$ . In the range of interest for experimental setups,  $\lambda_0 \gg \lambda_{n>0}$ , and also  $\pi_0 \approx 1 \gg \pi_{n>0}$ . The rate at which birth events occur is, therefore, approximately equal to  $\lambda_0$ . In addition, since in the experimental range of interest we have  $\mu_{n+1} \gg \lambda_n$  for

TABLE II. Constants and fitted parameters of the MDDF model [18].

Symbol	Value	Meaning
$\kappa$	0.32	Kinetic factor of dislocation creation <sup>a,b</sup>
$C_t$	2.31 km/s	Velocity of sound in Cu
$c$	1 $\mu\text{m}^{-1}$	Density of barriers in slip plane <sup>c</sup>
$G$	48 GPa	Shear modulus in Cu
$b$	0.25 nm	Burgers vector in Cu
$\Delta\rho$	0.1 $\mu\text{m}^{-1}$	Discrete change in mobile dislocation density <sup>c,d</sup>
$E_a$	0.8 eV	Activation energy of dislocation creation <sup>b</sup>
$\Omega$	5.6 eV/GPa	Activation volume of dislocation creation <sup>b</sup>
$k_B$	86.2 $\mu\text{eV/K}$	Boltzmann constant
$\xi$	1	Mobile dislocation trap efficiency
$\epsilon_0$	8.85 pF/m	Permittivity of vacuum
$\beta$	4.6	Stress/field enhancement factor <sup>e</sup>
$Z$	1	Structural parameter <sup>f</sup>

<sup>a</sup>Dependent on the activation entropy of the dislocation sources.

<sup>b</sup>Fitted to observed breakdown rates.

<sup>c</sup>Observed by microscopy.

<sup>d</sup>Inverse of dislocation cell size.

<sup>e</sup>Fitted value for the reference data set of breakdown rate measurements. This value is varied to account for the diversity of results among measurements in different structures.

<sup>f</sup>Linking stress to mobile dislocation density.

every  $n$  (and in particular  $\mu_1 \gg \lambda_0$ ), practically every birth event will be closely followed by a death event.  $\lambda_0$  can be thought of, then, as the rate at which dark current spikes, each representing a birth-and-death pair of events, will occur. Therefore,  $\lambda_0$  can be used to approximate  $r_s$ .

#### B. Dependence on the electric field

From Eq. (1), we find that

$$\lambda_0 = \frac{25\kappa C_t c}{G^2 b \Delta\rho} \sigma_0^2 \exp\left(-\frac{E_a - \Omega\sigma_0}{k_B T}\right). \quad (2)$$

Here, we might expect  $\sigma_0 = \sigma(n=0) = \epsilon_0(\beta E)^2/2$ . However, we saw in the experiment that current fluctuations occur only above  $E_{\text{th}}$ . This observation leads us to redefine the effective stress for mobile dislocation nucleation as

$$\sigma_0 = \frac{1}{2} \epsilon_0 [\beta(E - E_{\text{th}})]^2. \quad (3)$$

Such a threshold field might be due to preexisting stresses within the sample.

With this modified  $\sigma_0$ , the values of  $\lambda_0$  predicted by Eq. (2) can be directly compared to the measured dark current spike rates  $r_s$ . Since the dependencies of the spike rates on the electric field vary among measurement series, the parameter  $\beta$  is fitted individually for each series, while

the values of all other constants remain as in [18]. This is in line with the fitting procedure used previously to compare  $r_c$  to measured breakdown rates, where different values of  $\beta$  (and no other parameter) differentiate among experimental structures, thus accounting for both geometrical differences and different levels of conditioning of the electrodes [17,18]. It is also in line with the fact that  $\beta$  decreases over time, due to conditioning. As seen in Fig. 7, the theoretical values of  $\lambda_0$  as a function of  $E$  provide a good fit to the experimental results, with no need to further adjust the MDDF theory or any numerical values. This supports the hypothesis that the dark current spikes are, indeed, a manifestation of the fluctuations in the mobile dislocation density population as described in the MDDF model.

We note that the fit in [18] was done with  $E_{\text{th}} = 0$ . The process of breakdown explored in [18] is controlled by the probability of exceeding the critical mobile dislocation density, which is not strongly affected by  $E_{\text{th}}$ . This is due to the different functional form of the dependence of the breakdown rate on the field [18] vs Eq. (2), and also to the fact that breakdown occurs at significantly higher fields than prebreakdown fluctuations of the dark current. In addition, it is common to include an extensive annealing stage in the manufacturing of full-scale rf accelerating structures. This leads to the reduction of internal stresses, which, in turn, are expected to result in lower  $E_{\text{th}}$ . Still, taking the threshold field into account when calculating both the current spike and breakdown rates would necessitate minor changes in the values of the fitted parameters of the MDDF model. Further investigation could determine whether a threshold field exists and affects breakdown rates in high-field pulsed rf setups such as those analyzed in [18].

### C. Distribution in time

Having established that  $\lambda_0$  gives a good approximation of  $r_s$ , we further assume that each observable variation of the dark current is directly related to a mobile dislocation reaching the surface of the sample. Under this assumption, the full distribution of times between current spikes can be evaluated using the MDDF model. We recall that in the MDDF model, mobile dislocations are free to move within subgrain dislocation cells [18]. Here, we need to consider the kinetics of mobile dislocations in cells adjacent to the surface, and the probability of their ejection to the surface. In general, mobile dislocations can become sessile due to either reaching the surface or collision with barriers [17,18]. However, we expect cells adjacent to the surface to be relatively denuded of the sessile dislocations which serve as barriers, due to their strong elastic interaction with the surface [27].

The process of a mobile dislocation reaching the surface involves, therefore, two steps: (i) The creation of a mobile dislocation, and (ii) the ejection of the dislocation to the surface. These are represented in the MDDF model as transitions from state  $n$  to  $n + 1$ , followed by a transition

from state  $n + 1$  to  $n$ . Assuming that  $\mu_1 \gg \lambda_1$ , as is the case in the experimental range of interest, the time between spikes can be approximated by considering the random variable  $T = T_{0 \rightarrow 1} + T_{1 \rightarrow 0}$ . Here,  $T_{0 \rightarrow 1}$  and  $T_{1 \rightarrow 0}$  are random variables describing the transition time from state  $n = 0$  to  $n = 1$  and back, respectively. Assuming, for simplicity, that each transition individually is a Poissonian process, we find that  $T$  is a two-parameter hypoexponentially distributed variable, with the rate parameters  $\lambda_0$  and  $\mu_1$  [28].

We note that even though a dark current spike occurs when a mobile dislocation reaches the surface of the sample, i.e., at the transition from state  $n = 1$  to state  $n = 0$ , the mobile dislocation needs to be created in order to be depleted. Since  $\mu_1 \gg \lambda_0$ , the average value of  $T_{0 \rightarrow 1}$  is much greater than the average value of  $T_{1 \rightarrow 0}$ , so  $E(T) \approx E(T_{0 \rightarrow 1})$ . This is why, even though the spike of dark current corresponds to the transition  $n = 1 \rightarrow n = 0$ , the *mean* time interval between spikes (used to approximate  $r_s$ ) is  $E(T_{0 \rightarrow 1}) = \lambda_0^{-1}$ , as stated above.

For each voltage in each measurement series, the observed distribution of the time intervals between fluctuations was fitted to an exponential, two-parameter hypoexponential, and log-normal distribution (using MATLAB's mle function). The two-parameter hypoexponential fits yielded better results in the majority of the cases, and particularly for the higher voltages, in which there were more samples per voltage. The sum of the logarithms of the likelihood ratios [29] of all the fits was  $\sum \ln(L_h/L_e) = 5.16 \times 10^5$  for the hypoexponential and exponential fits, and  $\sum \ln(L_h/L_l) = 5.73 \times 10^3$  for the hypoexponential and log-normal fits. (For this calculation, the data measured at 2125 V in series B was excluded, as fitting it to any of the three distributions yielded poor results.) The quality of fit is demonstrated in Figs. 5 and 6 for three out of the 25 voltage steps in the measurement series.

## V. DISCUSSION AND CONCLUSIONS

The MDDF model provides a qualitative and quantitative explanation of observed breakdown rates in high-voltage applications. The purpose of the experiment described in this manuscript was to investigate the suggestion that the fluctuations of the mobile dislocation density, which are an underlying feature of the model, can be observed before breakdown itself occurs [17,18]. Indeed, dark current spikes were discovered, and their rates match the theoretical state transition rate  $\lambda_0(E)$  remarkably well, with no need to adjust the previously derived numerical parameters of the model.

The fit of the time interval distribution to a hypoexponential distribution further supports the proposal that the current spikes are an inherent feature of the dynamics described by the MDDF model. The fitted value of  $\lambda_0$  can be compared to  $r_s$ . However, since  $\mu_1 \gg \lambda_0$ , the confidence interval for the fit of  $\mu_1$  is large, making it impractical to derive values of  $\mu_1$  as a function of the electric field.

The experiment described here was performed on ridged OFHC copper electrodes. By modifying the electrode material production process and geometry, it might be possible to vary the amount of spikes prior to breakdown. This would enable us to study the dependence of prebreakdown fluctuations on the electrode structure. A configuration in which the spike rate increases significantly would allow more data samples to be collected per measurement, allowing the estimation of  $\mu_1$ , and maybe even the exploration of  $\lambda_n$  for  $n > 0$ . In addition, the current experimental setup allows the identification of strong temporal variation in the current, but not its specific shape. Thus, the current work concentrated on reproducing the distribution of times between current spikes. Future experiments can investigate the form of the emitted current within spikes, possibly providing constraints on the specific current emission mechanism.

Another subject for investigation is the value of  $\beta$ , in a given setup, as a function of the exposure time to electric fields. As explained in Sec. III, electrodes subject to electric fields undergo a continuous process of conditioning. As a result, while the functional form of the spike rate as a function of the electric field is consistent, the value of  $\beta$  [and therefore  $\lambda_0(E)$ ] in a given setup varies over time. Until now, this variation was followed via breakdown rate measurements. The discovery of dark current spikes allows us to examine the development of  $\beta$  via the spike rate, without having to bring the system to breakdown. Alternatively, it might be possible to measure current spike rates and breakdown rates in the same setup, so that the values of  $\beta$  derived from each of them can be compared.

The observed correlation between current spikes and breakdown can be utilized to reduce the breakdown rate in high voltage setups, and improve operational procedures in such systems, by using rates of observed dark current spikes to determine the level of conditioning of electrodes, or by monitoring spikes as observed *in situ* prior to breakdown.

## ACKNOWLEDGMENTS

E. Z. E., S. L., and Y. A. acknowledge funding from CERN and the PAZY foundation.

## APPENDIX A: DETAILS OF THE MEASUREMENT SERIES

As stated in Sec. III, the experiment was repeated in five measurement series. Over the course of each such measurement series, the applied voltage was varied in steps over two or three cycles, so that each voltage was revisited 2 or 3 times. Each voltage step in each of the cycles consisted of eight windows, 2 s long each, between which there were intervals on the order of one minute, in which the data collected was saved to disk. An example of the voltage over the course of one measurement series is shown in Fig. 8.

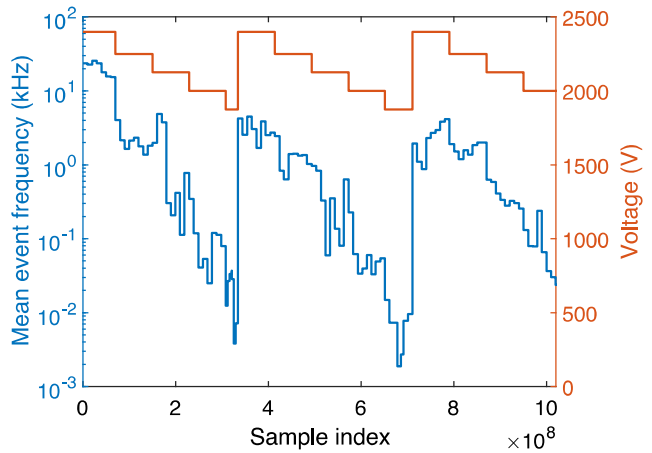


FIG. 8. Applied voltage and spike frequency over the course of measurement series C. The time in the horizontal axis is shown in units of oscilloscope samples, with the time intervals between the windows emitted.

The windows between voltage steps are omitted in the figure.

The voltages in each measurement series were chosen so as to allow the observation of as many current fluctuations

TABLE III. Details of the measurement series.

Series	Date	Voltage (V)	Electric field (MV/m)	$\lambda_0$ ( $10^4 \text{ s}^{-1} \text{ mm}^{-2}$ )
A	10/15/2019	1875	31.3	$1.34 \times 10^{-3}$
		2000	33.3	$1.74 \times 10^{-2}$
		2125	35.4	$8.85 \times 10^{-2}$
		2250	37.5	$9.05 \times 10^{-2}$
B	10/15/2019	2125	35.4	$4.69 \times 10^{-2}$
		2250	37.5	$2.27 \times 10^{-2}$
		2500	41.7	$1.11 \times 10^{-1}$
		2750	45.8	$2.67 \times 10^{-1}$
		3000	50.0	$3.64 \times 10^{-1}$
C	10/29/2019	1875	31.3	$5.20 \times 10^{-5}$
		2000	33.3	$6.34 \times 10^{-4}$
		2125	35.4	$4.79 \times 10^{-3}$
		2250	37.5	$1.97 \times 10^{-2}$
		2400	40.0	$2.85 \times 10^{-2}$
		1750	29.2	$9.14 \times 10^{-5}$
D	10/31/2019	1875	31.3	$1.90 \times 10^{-4}$
		2000	33.3	$5.24 \times 10^{-4}$
		2125	35.4	$8.55 \times 10^{-4}$
		2250	37.5	$1.79 \times 10^{-3}$
		2375	39.6	$2.30 \times 10^{-3}$
		2000	33.3	$5.78 \times 10^{-4}$
E	11/01/2019	2125	35.4	$1.28 \times 10^{-3}$
		2250	37.5	$2.05 \times 10^{-3}$
		2375	39.6	$3.59 \times 10^{-3}$
		2400	40.0	$3.01 \times 10^{-3}$

possible, while making sure that there were no breakdowns within a window. Due to these considerations, and to the effects of conditioning, the voltage steps in the different series were not identical. Table III lists the measurement series, the date at which each was carried out, the voltages in each of the series, and the applied electric field. In addition, the value of  $\lambda_0$ , yielding the best fit to a two-parameter hypoexponential distribution, is listed. As explained in Sec. IV, this value is also approximately equal to the rate of current spikes  $r_s$ .

## APPENDIX B: SPIKE IDENTIFICATION ALGORITHM

The purpose of the spike identification algorithm was to identify the onset time of the unique current spike events. The algorithm had to distinguish the events from noise, and avoid double counting by determining whether temporally consecutive peaks of current represented separate spikes, or were caused by ringing, see Fig. 4.

Concerning the first issue, the noise in the current was assumed to be normally distributed. For a normal distribution of  $N$  samples with standard deviation  $\sigma$ , the expected number of samples deviating by  $n\sigma$  from the mean is  $F = [1 - \text{erf}(n/\sqrt{2})]N$ . At a sampling rate of 5 MHz and window length of 2 s, each window contains  $N = 10^7$  samples. The lowest integer value of  $n$  yielding  $F < 1$ , i.e., less than one false positive per window on average, is, then,  $n = 6$ . Figure 9 shows a histogram of the absolute values of the current measured in a typical window. It is seen that the shape of the histogram diverges from a half-Gaussian beginning from a deviation between  $5\sigma$  and  $6\sigma$ . Therefore, at the first stage of the algorithm, the mean and standard deviation of the measured current were

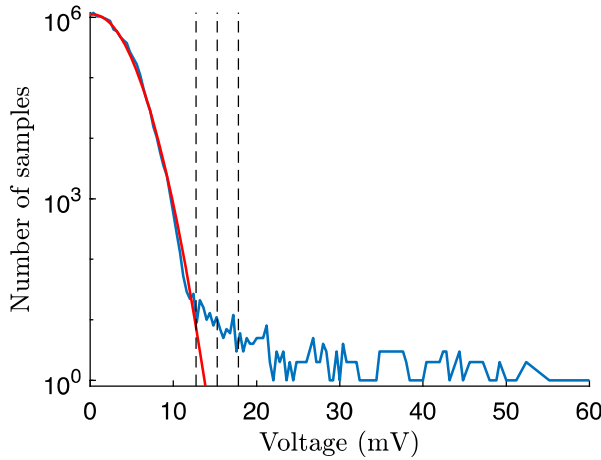


FIG. 9. Frequency histogram of the measured dark current signal values in one window, measured at an electric field of 29.2 MV/m, in measurement series D. The histogram contains 150 evenly spaced bins, each 0.4 mV (corresponding to a current of  $2.3 \times 10^7 \mu\text{A}$ ) wide. The vertical dashed lines represent deviations from the mean of  $5\sigma$ ,  $6\sigma$ , and  $7\sigma$ .

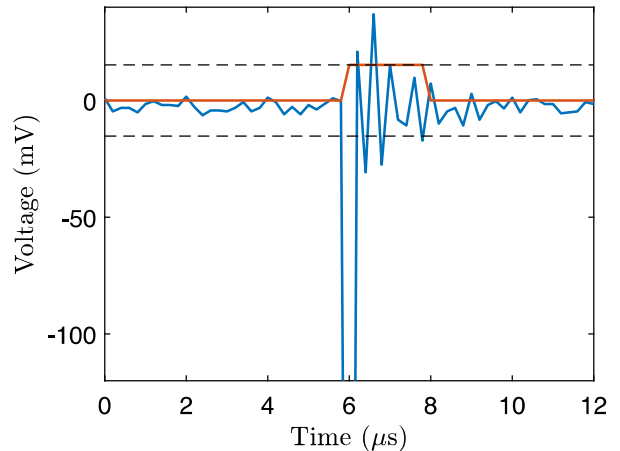


FIG. 10. Dark current signal as a function of time, shown over a period of 12  $\mu\text{s}$  measured at an electric field of 29.2 MV/m in measurement series D. The first peak of the current reaches a value of approximately  $-800$  mV. The dashed lines represent the event thresholds of  $6\sigma$ , and the solid straight line shows how a number of current peaks, caused by ringing, were counted as one spike.

calculated for each window individually. Samples deviating from the mean by  $6\sigma$  or more were considered as potential spike locations.

At the second stage, to avoid double counting due to ringing, the algorithm examined the measured current of the samples which were not discarded at the first stage. If the absolute value of the current was a maximum within a time range of  $\pm 20 \mu\text{s}$  from the sample, it was determined to be the location of a spike. This time constant was considerably greater than the observed duration of ringing, and considerably smaller than typically observed times between spikes at all electric fields. Figure 10 shows a typical spike made up of a few peaks, each consisting of samples above the threshold of  $6\sigma$ . The spike is detected by the first stage of the algorithm, and counted as exactly one spike by the second stage.

- [1] *Handbook of Vacuum Arc Science and Technology: Fundamentals and Applications*, edited by R. L. Boxman, D. M. Sanders, and P. J. Martin (Noyes, Park Ridge, NJ, 1996).
- [2] P. G. Slade, *The Vacuum Interrupter: Theory, Design, and Application* (CRC Press, Boca Raton, FL, 2008).
- [3] *High Gradient Accelerating Structure*, edited by W. Gai (World Scientific, Singapore, 2014).
- [4] G. Teel, A. Shashurin, X. Fang, and M. Keidar, Discharge ignition in the micro-cathode arc thruster, *J. Appl. Phys.* **121**, 023303 (2017).
- [5] W. P. Dyke, J. K. Trolan, E. E. Martin, and J. P. Barbour, The field emission initiated vacuum Arc. I. Experiments on Arc initiation, *Phys. Rev.* **91**, 1043 (1953).

- [6] S. Döbert, RF-breakdown in high-frequency accelerators, SLAC Technical Report No. SLAC-PUB-10463, 2004.
- [7] P. Burrows, N. C. Lasheras, L. Linssen, M. Petrič, A. Robson, D. Schulte, E. Sicking, and S. Stapse, The Compact Linear Collider (CLIC) 2018 summary report, CERN Technical Report No. CERN-2018-005-M, 2018.
- [8] A. Descoeuilles, Y. Levinsen, S. Calatroni, M. Taborelli, and W. Wuensch, Investigation of the dc vacuum breakdown mechanism, *Phys. Rev. ST Accel. Beams* **12**, 092001 (2009).
- [9] I. Profatilova, X. Stragier, S. Calatroni, A. Kandratsyeu, E. R. Castro, and W. Wuensch, Breakdown localisation in a pulsed DC electrode system, *Nucl. Instrum. Methods Phys. Res., Sect. A* **953**, 163079 (2020).
- [10] A. Saressalo, A. Kyritsakis, F. Djurabekova, I. Profatilova, J. Paszkiewicz, S. Calatroni, and W. Wuensch, Classification of vacuum arc breakdowns in a pulsed dc system, *Phys. Rev. Accel. Beams* **23**, 023101 (2020).
- [11] V. Zadin, A. Pohjonen, A. Aabloo, K. Nordlund, and F. Djurabekova, Electrostatic-elastoplastic simulations of copper surface under high electric fields, *Phys. Rev. ST Accel. Beams* **17**, 103501 (2014).
- [12] S. Vigonski, M. Veske, A. Aabloo, F. Djurabekova, and V. Zadin, Verification of a multiscale surface stress model near voids in copper under the load induced by external high electric field, *Appl. Math. Comput.* **267**, 476 (2015).
- [13] A. Kyritsakis, M. Veske, K. Eimre, V. Zadin, and F. Djurabekova, Thermal runaway of metal nano-tips during intense electron emission, *J. Phys. D* **51**, 225203 (2018).
- [14] W. Wuensch, Advances in the understanding of the physical processes of vacuum breakdown, CERN Technical Report No. CERN-OPEN-2014-028, 2013.
- [15] A. Degiovanni, W. Wuensch, and J. G. Navarro, Comparison of the conditioning of high gradient accelerating structures, *Phys. Rev. Accel. Beams* **19**, 032001 (2016).
- [16] A. Pohjonen, F. Djurabekova, K. Nordlund, A. Kuronen, and S. Fitzgerald, Dislocation nucleation from near surface void under static tensile stress in Cu, *J. Appl. Phys.* **110**, 023509 (2011).
- [17] E.Z. Engelberg, Y. Ashkenazy, and M. Assaf, Stochastic Model of Breakdown Nucleation under Intense Electric Fields, *Phys. Rev. Lett.* **120**, 124801 (2018).
- [18] E. Z. Engelberg, A. B. Yashar, Y. Ashkenazy, M. Assaf, and I. Popov, Theory of electric field breakdown nucleation due to mobile dislocations, *Phys. Rev. Accel. Beams* **22**, 083501 (2019).
- [19] S. Calatroni, A. Descoeuilles, J. W. Kovermann, M. Taborelli, H. Timko, W. Wuensch, F. Djurabekova, K. Nordlund, A. Pohjonen, and A. Kuronen, Breakdown studies for the CLIC accelerating structures, in *Proceedings of Linear Accelerator Conference (LINAC'10)*, Tsukuba, Japan (JACoW, Geneva, 2010), pp. 217–219.
- [20] A. Anders, *Cathodic Arcs: From Fractal Spots to Energetic Condensation*, Springer Series on Atomic, Optical, and Plasma Physics (Springer, New York, 2008), Vol. 50.
- [21] A. Anders, A review comparing cathodic arcs and high power impulse magnetron sputtering (HiPIMS), *Surf. Coat. Technol.* **257**, 308 (2014).
- [22] A. Grudiev, S. Calatroni, and W. Wuensch, New local field quantity describing the high gradient limit of accelerating structures, *Phys. Rev. ST Accel. Beams* **12**, 102001 (2009).
- [23] A. Cahill, J. Rosenzweig, V. Dolgashev, S. Tantawi, and S. Weathersby, Ultra high gradient breakdown rates in x-band cryogenic normal conducting rf accelerating cavities, in *Proceedings of the Eighth International Particle Accelerator Conference (IPAC'17)* (JACoW, Geneva, 2017).
- [24] J. Wang and G. Loew, Field emission and RF breakdown in high-gradient room-temperature linac structures, SLAC Technical Report No. SLAC-PUB-7684, 1997.
- [25] P. Kranjec and L. Ruby, Test of the critical theory of electrical breakdown in vacuum, *J. Vac. Sci. Technol.* **4**, 94 (1967).
- [26] S. V. Baryshev, S. Antipov, J. Shao, C. Jing, K. J. P. Quintero, J. Qiu, W. Liu, W. Gai, A. D. Kanareykin, and A. V. Sumant, Planar ultrananocrystalline diamond field emitter in accelerator radio frequency electron injector: Performance metrics, *Appl. Phys. Lett.* **105**, 203505 (2014).
- [27] J. P. Hirth and J. Lothe, *Theory of Dislocations* (Krieger, Malabar, FL, 1982).
- [28] D. R. Cox, *Renewal Theory* (Methuen, London, 2008).
- [29] G. Bohm and G. Zech, *Introduction to Statistics and Data Analysis* (DESY, Hamburg, 2010).

## CHAPTER 5

# Discussion

---

### 5.1 Comparison to Goals in the Research Proposal

The main goal of this research was to construct and validate a model describing the formation of surface features on electrodes subject to strong electromagnetic fields. Such a model would, as described throughout this thesis, provide the missing description of the initial step of breakdown nucleation. This core goal was achieved in Chapter 2, where such a model was constructed, and shown to produce results which agree well with experimentally measured breakdown rates. The model was further validated by comparing its postulates to microscopic observations in Chapter 3.

Another original goal was to identify prebreakdown fluctuations of the field emission currents, and of acousto-electric signals, corresponding to subcritical processes of the model. This was done successfully for the field emission currents in Chapter 4, in which spikes in the dark current were found to behave as predicted by the model. The evolution of the current spike rates over time, which was shown to correspond to expected breakdown rates, also allows for the estimation of the effect of *conditioning* (see Chapter 4), which was another goal of the research. In addition, the dark current spikes can serve as prebreakdown signals, thus fulfilling one more research goal.

An additional goal was to propose a mechanism controlling pulse-length dependency. This was achieved in Chapter 3.

The original research plan included further development of the model with atomistic simulations. Due to the fact that a dedicated setup was built in CERN to test our model, focus was shifted to the successful analysis of the field emission currents mentioned above, so that not enough time was left to conduct the atomistic simulations. Such simulations can enhance the MDDF model in the future, aside from the possibilities of future research mentioned in Chapters 2-4.

## 5.2 Applicability and Future Research

The MDDF model was developed in cooperation with the CLIC study in CERN, where breakdown is the main limiting factor of further development. The model provides opportunities to reduce breakdown rates by designing future electrodes so that the mobility of dislocations is limited, thereby avoiding the critical transition which leads to breakdown nucleation. This can be done either by working the metals used in CLIC, or by modifying the process of conditioning (see Chapter 3) so that it leads to a reduced mobility of dislocations in the electrodes. The observed correlation between dark current spikes and breakdown, described in Chapter 4, can be utilized to monitor the efficacy of these processes, by using rates of observed dark current spikes to determine the mobility of dislocations in processed electrodes, or by monitoring spikes as observed *in situ* prior to breakdown.

Although most of the experimental data used to develop the model came from CLIC, the model aims to describe breakdown nucleation in general. Experiments involving breakdown rates and dark current spikes can be con-

ducted in other applications and settings, and their results compared to the predictions of the model.

Additional future research will most likely involve atomic simulations, which will provide a better understanding of the fundamental processes which lead to the nucleation of mobile dislocations within metals subjected to strong electric fields. This can affect the forms of the equations of multiplication and depletion of mobile dislocations in the model, and provide a method of determining, *a priori*, those values of the physical parameters of the model which are currently inferred from fits to the experimental data.

As stated in Chapters 3 and 4, additional phenomenological experiments, too, can serve to further the development and validation of the model. Such experiments include, among other options, measuring breakdown rates as a function of the pulse length of the electromagnetic fields, or measuring dark current spikes and breakdown rates at the same time in the same setup.



# Bibliography

- [1] R. L. Boxman, D. M. Sanders, and P. J. Martin, eds., *Handbook of Vacuum Arc Science and Technology: Fundamentals and Applications*. Park Ridge, NJ: Noyes, 1995.
- [2] A. Anders, *Cathodic Arcs: From Fractal Spots to Energetic Condensation*, vol. 50 of *Springer Series on Atomic, Optical, and Plasma Physics*. New York: Springer, 2008.
- [3] S. Döbert, “Rf-breakdown in high-frequency accelerators,” *SLAC Technical Report No. SLAC-PUB-10463*, May 2004.
- [4] CERN, *Compact Linear Collider Study list of members*, 2020. Available at <http://clic-study.web.cern.ch/content/list-members>, as of March 5, 2020.
- [5] A. Saressalo, A. Kyritsakis, F. Djurabekova, I. Profatilova, J. Paszkiewicz, S. Calatroni, and W. Wuensch, “Classification of vacuum arc breakdowns in a pulsed dc system,” *Phys. Rev. Accel. Beams*, vol. 23, p. 023101, Feb 2020.
- [6] P. Burrows, N. Catalan Lasheras, L. Linssen, M. Petrič, A. Robson, D. Schulte, E. Sicking, and S. Stapnes, “The compact linear collider (clic) 2018 summary report,” *CERN Technical Report No. CERN-2016-004*, Aug 2016.
- [7] A. Descoeuilles, Y. Levinsen, S. Calatroni, M. Taborelli, and W. Wuensch, “Investigation of the dc vacuum breakdown mechanism,” *Phys. Rev. Spec. Top. Accel. Beams*, vol. 12, p. 092001, 2009.

- [8] I. Profatilova, X. Stragier, S. Calatroni, A. Kandratsyeu, E. R. Castro, and W. Wuensch, “Breakdown localisation in a pulsed dc electrode system,” *Nucl. Instrum. Methods A*, vol. 953, p. 163079, 2020.
- [9] S. Calatroni, A. Descoeudres, J. W. Kovermann, M. Taborelli, H. Timko, W. Wuensch, F. Djurabekova, K. Nordlund, A. Pohjonen, and A. Kuronen, “Breakdown studies for the clic accelerating structures,” in *Proceedings of Linear Accelerator Conference (LINAC’10), Tsukube, Japan*, (Geneva), pp. 217–219, JACoW, 2010.
- [10] C. Kittel, *Introduction to Solid State Physics*. New York: Wiley, 1996.
- [11] J. P. Hirth and J. Lothe, *Theory of Dislocations*. Malabar, FL: Krieger, 1982.
- [12] C. W. Gardiner, *Handbook of Stochastic Methods*. Berlin: Springer, 2004.
- [13] P. Collet, S. Martínez, and J. San Martín, *Quasi-Stationary Distributions*. Springer Series on Probability and its Applications, Berlin: Springer-Verlag, 2013.
- [14] G. Bohm and G. Zech, *Introduction to Statistics and Data Analysis*. Hamburg: DESY, 2010.
- [15] J. Weertman and J. R. Weertman, *Elementary Dislocation Theory*. New York: Macmillan, 1964.
- [16] J. Wang and G. Loew, “Field emission and rf breakdown in high-gradient room-temperature linac structures,” *SLAC Technical Report No. SLAC-PUB-7684*, October 1997.

## תקציר

התפרקותן של מתקכות בשדות חשמליים חזקים הינה בעיה ארוכת ימים ביישומי מתח גובה, המגבילה את האמפליטודות אליהן ניתן להגיע בשדות חשמליים ואלקטרומגנטיים. "שימוש ספציפי שכזה הוא במחקר ההיתכנות של מאייז החלקיקים הלינארי הקומפקטי (compact linear collider, CLIC) ב-CERN, ובעוד מאייזים בגרדינט גובה, בהם הבנה ושליטה בהתפרקויות הן מהוות ציר פיתוח קרייטי. בעבר הוצע שתוצאות על פני השטח הן חיוניות להתפתחותן של התפרקויות. ברם, המנגנון שבאמצעותו תוצאות כאלה נוצרות אינו מובן היטב.

בזאת זאת, אנחנו בונים מודל של אדוות בצפיפות הדיסלוקציות הנידיות (mobile dislocation density), שבו התפרקות של מתקכת בשדה חשמלי חזק מונעת על ידי דיסלוקציות במבנה הגביש. במודל זה, צפיפות הדיסלוקציות הנידיות נעה בדרך כלל סביב נקודה יציבה, כאשר יש הסתברות סופית שהיא תבצע מעבר קרייטי בהשפעת השדה החשמלי. ברגע שמתרכש מעבר זה, צפיפות הדיסלוקציות הנידיות תגדל באופן דטרמיניסטי, אשר יוביל להתהווותן של תוצאות על פני השטח, ובהמשך להתפרקות. הסתברות מעבר זה צפופה לאגדול ככל שגדל השדה החשמלי החיצוני, עד לשדה קרייטי שבו ההתפרקות היא מיידית. על ידי תיאורו של מנגנון שבאמצעותו תוצאות על פני השטח, באופן שהוא קונסיסטנטי עם תוצאות ניסיוניות, מודל ה-MDDF משלים את התיאור הפיזיקלי של התפתחותן של התפרקויות.

פרמטריזציה של המודל מתבצעת באמצעות ניתוח מיקרוסקופי של דוגמאות של קוודות מנוחשת נתולות חמצן, בעלת מוליכות תרמית גבוהה (oxygen-free high thermal conductivity, OFHC), שמקורו בפרויקט CLIC של CERN, המאפשרת הערכה של קבוע הייצור והחיסול של דיסלוקציות נידיות, כתלות במצב הפיזי ההתחלתי של החומר ובשדה החשמלי החיצוני. אנו מוצאים ביטויים אנליטיים עבור זמן ההתפרקות הממוצע, והتلגוגות ההסתברות הייצה-למחצה של צפיפות הדיסלוקציות הנידיות, וכן מאמטים תוצאות אלה באמצעות אלגוריתם Gillespie. אנו מפעילים אלגוריתם של ריבועים מינימלים (least-squares) על מנת להתאים את התוצאות לתוצאות ניסיוניות של תלות קצב ההתפרקויות בעוצמת השדה החיצוני ובטמפרטורה. התוצאות המותאמות של המודל מתאימות היטב לתוצאות הניסיוניות.

השפעתה של וריאציה בכמה מן ההנחהות של המודל הפיזיקלי נשקלות, ומוצעים מספר ניסויים נוספים לאימות המודל, הכוללים בחינה של השפעת הטמפרטורה ואורך הפולס, כמו כן השפעת שדה חשמלי תלוי בזמן, על קצב ההתפרקויות. בנוסף, בהתבסס על מודל ה-MDDF, חדינו את קיומן של פלקטואציות בצפיפות הדיסלוקציות הנידיות לפני ההתפרקות, אשר באים לידי ביטוי כקפיצות בזרם

החוור הנמדד ביןALKTR0D0T. נבנה ב CERN התקן לבחינת תחזית זו, שבו אכן התגלו ואופיינו קפיצות אלה. קיבל התרחשותם והתפלגותם בזמן מתאימים לתחזיות של מודל ה MDDF, הן בצורת הפון-קצינלית והן בערכים מסוימים מוחלטים. התחזית והתייאור של תופעה זאת מהווים אימות נוספת של המודל, ומספקים אפשרות לגילוי במודדם של התפרקות מתקרבת.

עבודה זו נעשתה בהדריכתו של

פרופ' ינון אשכנזי



# מודל סטטיסטי של התפרקות מתכוות בשדות חמליים חזקים

חיבור לשם קבלת תואר

"דוקטור לפילוסופיה"

מאט

אלן אנגלברג

הוגש לסנט האוניברסיטה העברית בירושלים

ספטמבר 2020